UNIVERSITY OF CALIFORNIA
RIVERSIDE

A Study of Transition Metal Dichalcogenides: Synthesis, Catalysis, and Mechanically Induced, Elastic Tuning of their Optical Properties

A Dissertation submitted in partial satisfaction
of the requirements for the degree of

Doctor of Philosophy

in

Materials Science and Engineering

by

Sarah Michelle Bobek

August 2016

Dissertation Committee:
Dr. Ludwig Bartels, Chairperson
Dr. Joshua C. H. Lui
Dr. De-en Jiang

The Dissertation of Sarah Michelle Bobek is approved:

_____

_____

_____

Committee Chairperson

University of California, Riverside

Acknowledgements

First and foremost, I would like to express my gratitude and respect for my research and academic advisor, Dr. Ludwig Bartels. I am grateful for his intellectual insight in our discussions of research, creative ideas and consistent support. Facilitating growth of students in the laboratory, and the classroom is the crux of the research advisors challenge, to produce a self-motivated, self-sufficient thinker. I have seen the lab more than double in the number of graduate students. Dr. Bartels has maintained the same fastidious level of mentorship over these years. And, owing to his diligence, he has time and time again relentlessly forged a path where there was none, for the gain of his lab and myself. Whether it be securing a laboratory space to carry out research by moving three summers in a row, or advocating to renew my Dean's Distinguished fellowship for funding in 2011, his persistence has given me many opportunities to succeed.

I would like to express appreciation to my defense committee members, Dr. De-en Jiang and Dr. Joshua C. H. Lui for accommodating my defense date and for taking time to consider this work. Dr. Lui brings expertise from his study of strained two dimensional materials. Dr. Jiang has particular insight into catalysis from the perspective of a theorist. I look forward to your thoughts.

Although my focus shifted from the study of coordination chemistry, my first mentors in the laboratory helped me immensely. From them, I learned good scientific practices in the field, and more importantly, the necessary work ethic to

succeed. Thank you for investing time teaching me; Dr. Miaomiao Liu, Dr. Dezheng Sun, Dr. Yeming Zhu, Dr. Jon Wyrick and Dr. Wenhao Luo.

I am grateful for my oral defense committee members, Dr. Phillip Christopher, Dr. Jack Eichler, Dr. Pingyun Feng, and Dr. Cengiz Ozkan for their time and questions. Through that process, my method and the presentation of my work was raised to a higher standard.

I would like to thank Dr. Alec Talin and Dr. François Leonard, at Sandia National Laboratory (SNL) in Livermore, CA, for training and challenging me beyond the front of photoelectrochemistry and photocurrent spectroscopy. We engaged in critical discussions of scientific phenomena driving our results and discussed how to think strategically about high-level directions for research. Thank you to Marie-Josee and Dr. François Leonard for so graciously welcoming my lab mate and I into their home for six months. Their hospitality allowed me to carry out the photoelectrochemistry work in Chapter 4. I would like to thank Dr. Raymond Friddle for training on and use of the Kelvin Probe instrument at SNL, Livermore.

A special thanks goes to the lab members who have helped, by providing opportunities to practice in preparation for my final defense. For reading the proof-reading the document in-full, I owe many thanks to Lauren Bobek, J.D.

Experimentally, I would like to acknowledge contributions made by my colleagues. The x-ray photoelectron spectroscopy work, done in the growth section of this dissertation, was carried out with great expertise by my former lab mate Dr. Quan Ma. Mark Micklich was able to provide insight, and the much needed density

functional theory calculations for the work which looks at strain on the two dimensional materials. Chun-Yu Huang has become adept at transfer of two dimensional materials, and will continue to further the transfer methods discussed here, accompanied by Michelle Wurch and Michael Valentin. I would like to express my appreciation for the work done on novel material compositions, carried out by David Barroso, who provided many molybdenum and tungsten selenide materials for use in the strain measurements. Ariana Nguyen was extremely helpful in coordination of sulfide samples grown by Aimee Martinez, William Coley and Sahar Naghibi Alvillar used in Chapter 6. Machining components that were instrumental in the execution of experiments central to this work was done by Miguel Isarraraz and Katie Marie Magnone.

I have had the opportunity to work with many undergraduate students in the lab during my time at UC Riverside. They have given me the opportunity to learn and lead. Their involvement in this work has been extremely helpful. Most relevant to Chapter 5 are the contributions of Edward Benavidez and Hannah Oteng-Quarshie, who were funded interns through summer programs at UC Riverside thanks to funding contributions from the Semiconductor Research Corporation and the National Science Foundation- REU program. For the execution of growth techniques developed in Chapter 3, supporting the work I was doing while in Livermore, I thank Kelly Brown, Justin Chung, Christopher Lee and Dongkun Lee.

My parents, Barry and Sheila Bobek, deserve more thanks than can be given for their hard work to provide for my sisters and I economically, and for the

great care and time they invested in our personal growth. Additionally, the diligence of my father, mother and a young, talented pediatric optometrist, Dr. Robert Hered at Nemours Children's Hospital in Jacksonville, gave me the invaluable gift of my eye sight which has allowed me to observe many wonders, learn and think through spatial visualization, and practically, it helped greatly in carrying out these experiments.

The love and friendship of my sisters, Lauren and Katelyn, is a gift that I am grateful for each day and has supported me immensely in the completion of this work.

ABSTRACT OF THE DISSERTATION

A Study of Transition Metal Dichalcogenides: Synthesis, Catalysis, and Mechanically Induced, Elastic Tuning of Their Optical Properties

by

Sarah Michelle Bobek

Doctor of Philosophy, Graduate Program in Materials Science and Engineering
University of California, Riverside, August 2016
Dr. Ludwig Bartels, Chairperson

Highly photosensitive, tunable direct band gap materials of subnanometer thickness represent an important path forward in minimization of opto-electronic devices. It is inevitable that the scale of devices will soon move beyond the 2 nm node. With the ever decreasing scale of devices, two dimensional transition metal dichalcogenides (TMDs) offer a promising avenue towards reduced dimensionality and unveil novel direct-indirect band gap shift tuning capabilities by means of thickness, and composition. The first goal of this work is to investigate bottom-up approaches to fabrication of integrated materials systems using chemical vapor deposition (CVD) grown TMDs. In that vein, this thesis examines the methods for growth of the transition metal dichalcogenide materials on a variety of metal oxide terminated substrates, graphene and directly onto an economical photocathode for the hydrogen evolution reaction in water splitting. Where the limits of CVD

processing preclude bottom-up fabrication, the research presents methods to vertically stack CVD-grown two dimensional materials and deposit them on arbitrary substrates via physical transfer techniques, allowing for a single step process to obtain CVD grown TMDs on flexible substrates. Executing physical transfer allows us to reach the final goal of this work, to investigate a third type of optical tuning, that of uniaxial mechanical strain. The thesis probes reversible mechanical strain-induced shifting in the optical behavior of the chemical vapor deposition grown materials shown here in tension and compression.

TABLE OF CONTENTS

LIST OF FIGURES

Chapter 1. Introduction

1.1 Structure of the Thesis

This dissertation presents a group of cohesive projects carried out in the lab of Dr. Ludwig Bartels in the field of opto-electronics of two dimensional materials. Because the work which is carried out is experimental, I first discuss the spectroscopic techniques and instrumentation to give depth to the research results which follow. Each of the research themes encompassed is discussed by chapter chronologically, in the order each was motivated.

The research themes can be broken into four sections: 1.) synthesis of TMD materials, 2.) photoelectrochemistry, 3.) transfer and 4.) strain-probing of the optical band gap. The first focus of research is chemical vapor deposition (CVD) growth of monolayer TMDs. In order to establish a bottom-up synthesis route for direct use of as grown samples, we show fabrication of the materials on a variety of substrates including an electrode for water splitting. Eliminating post-growth fabrication steps represents an efficient and clean route to scalability. Furthermore, the growth of catalytically active MoS_2 directly on a photocathode allowed us to look at the photoelectrochemical performance of chemical vapor deposition grown molybdenum disulfide for water reduction. Upon closer examination of the system, using kelvin probe force microscopy (KPFM), we showed that metal patterning a catalytically inactive metal would improve the performance of our materials system by decreasing the amount of potential necessary to drive the hydrogen evolution reaction. However, the synthesis process degrades thin layers of evaporated

metal. The high process temperatures and precursors employed in the growth process limited the library of substrate materials amenable to TMD deposition as well as the patterning of substrates with thin film metals. The impetus to deposit the two dimensional materials onto substrates, not able to withstand growth conditions, gave way to development and optimization of a physical, dry transfer techniques more attractive than the typical aqueous etching of silicon dioxide with a harsh solvent.

With the TMD materials transferred, optical properties intact, onto a flexible substrate, it was possible to probe the effect of mechanical strain on the materials. In the final chapter of this work, we examine a reversible shifting in the optical properties of the material with application of uniaxial mechanical strain.

1.2 Introduction to Transition Metal Dichalcogenides (TMDs)

Transition metal dichalcogenides are two-dimensional, layered materials characterized by a hexagonal lattice structure with trigonal prismatic coordination.[1] In the 2-H phase, prepared as described in the following text, two planes of chalcogenide atoms (X) lie in alignment above and below the equatorial transition metal plane (M) forming a sandwich with stoichiometry MX_2.[2] Transition metal dichalcogenides such as molybdenum disulfide occur naturally in the bulk form, and have been widely used tribologically as lubricants and as a precursor to graphite in pencil cores. Synthesis and subsequent characterizations are simplified by the stability evidenced in the presence of molybdenite (MoS_2) in the earth's

crust at 1 ppm.[3] The position of chalcogenide atoms relative to the transition metal atoms, and the distance of molecular layers from one another is a determining factor in the optical and electronic properties of the layered materials. Orbital interactions dominate the physics responsible for the phenomena described throughout this work.

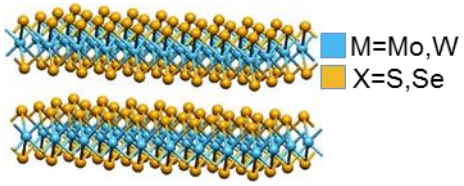

Figure 1.1: Ball-stick model of a transition metal dichalcogenide bilayer material showing trigonal prismatic coordination of the chalcogenide (yellow) and transition metal (blue) species separated by the interlayer van der Waal's gap.

It is within the last six years that this class of two dimensional materials has become a research focus. Molybdenum disulfide was first studied in its' monolayer form, exfoliated using the same process that is used to fabricate exfoliated graphene. The ability to isolate single molecular sheets of the material is possible due to the weak Van der Waals forces between adjacent layers and between the films and their substrate. These first reports uncovered drastically different behavior of the single layer materials compared to their bulk counterparts.[4, 5]

Since that discovery, the class of materials known now as TMDs has expanded to include iterations of the metals; molybdenum and tungsten in combination with chalcogenide species; sulfur, selenium and tellurium. Chemical vapor deposition processes have also advanced the materials beyond the capabilities of exfoliation

by providing a route to customize composition, create material of a single thickness, and scale-up production. But, with novel two dimensional materials being synthesized as an ongoing process, there is much to be learned about their unique properties.

1.3 Emergence as Two Dimensional Materials

Interest in transition metal dichalcogenide materials within the genre of two dimensional materials arises from the band structure transformation, which occurs with decreasing layers, and its lack of inversion symmetry leading to large spin splitting in the valence band. These two attributes contribute to the high photoluminescence seen for monolayer MoS_2. The change in the optical behavior seen in the single layer material, when the direct K point transition becomes more energetically favorable, is due to previously mentioned orbital interactions. The result of the new, direct band gap are materials which are highly photoresponsive in the cases discussed to wavelengths below 635 nm, well within the visible spectrum. Later in this work, we show the characteristic widening of the band gap of transition metal dichalcogenides with decreasing layers is reversed in monolayer material through mechanical strain towards new opto-electronic applications.

1.4 Electronic Properties of Transition Metal Dichalcogenides

Extensive angle resolved photoelectron spectroscopy (ARPES) and inverse angle resolved photoelectron spectroscopy (iARPES) studies have been done to

experimentally map the electron momentum and density of states of various TMD materials.[6-8] The results give clarity to the theory which previously developed.[9] One of the key outcomes of the experimentally produced band structures was the demonstrated splitting of the valence band of TMD materials at the K point in the Brillouin zone. The amount of splitting is directly related to the degree of spin-orbit coupling taking place and the lack of inversion symmetry in the material. The splitting is due to orbital interactions described by crystal field ligand theory. In the theoretical model, for instance, the d orbitals split into different, discrete energy levels according to the trigonal prismatic coordination, the d_{z^2} lowest in energy, then the d_{xy} and $d_{x^2-y^2}$, and finally the highest energy d_{xz} and d_{yz}.[10] Spin splitting in the valence band is observed to be higher in the tungsten disulfide case, which due to the mass of the tungsten atom possesses a higher degree of spin-orbit coupling.

1.5 Vibrational Properties of Transition Metal Dichalcogenides

Raman spectroscopy is a powerful nondestructive characterization tool in the study of transition metal dichalcogenides. Because, similar to graphene, thickness dependent phenomena are observed though investigation of the allowed vibrational modes of the materials. These phonon modes at discreet frequencies arise from motions in the crystal seen in Figure 1.2.

1.5.1 Molybdenum Disulfide

In the case of molybdenum disulfide, the first of the two vibrational motions resolved by our Raman technique is occurring from sulfur atoms being displaced in one direction and molybdenum in the opposite direction in the plane of the layer. The second vibrational motion observed for molybdenum disulfide is with chalcogenide atoms in alignment perpendicular to the plane of the layer moving away outward along the orthogonal plane away from the transition metal in the center of the layer, depicted in Figure 1.2. These phonon modes which are allowed are the in plane and out of plane, are the E^1_{2g} and A_{1g} respectively.

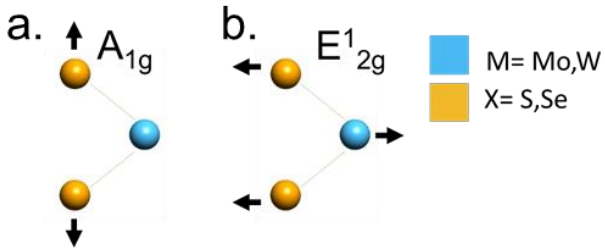

Figure 1.2: a. Side view of a single layer TMD unit. The arrows represent motion of the a. out of plane, A_{1g}, and b. in-plane, E^1_{2g}, vibrational modes of 2-H phase materials with transition metal (blue) between chalcogenide (yellow).

These modes, also common to the other TMDs studied here, respond sensitively to the presence of neighboring layers. For that reason, the in-plane mode is blue-shifted by thinning and the out of plane mode is dampened. The result is that Raman shift separating the two peaks becomes lessened for monolayer material to an established distance of 18-19 cm^{-1}.[4] This is a useful tool in corroborating additional data on material thickness. But, as is later discussed here and established elsewhere, strain shifts the E^1_{2g} mode in MoS_2, so its' use in

observation of thickness is limited by built-in strain on chemical vapor deposition prepared substrates.[11]

Raman studies of MoS_2 shows that thinning from bulk to monolayer causes the in- plane E^1_{2g} mode to increase and the out of plane A_{1g} mode to exhibit decreased frequency. This widely reproduced narrowing is used as an indicator of layer thickness[4]. The phonon modes particular to the in-plane vibrations of the transition metal dichalcogenides are also shifted by application of strain to the monolayer material, a property addressed in Chapter 6.[12]

1.5.2 Molybdenum Diselenide

In molybdenum diselenide materials the vibrational modes, which are allowed in Raman for the monolayer material, are the in-plane E^1_{2g} mode at 287.2 cm^{-1}, the out of plane A_{1g} mode at 243 cm^{-1}. A good indicator of thickness in the Raman measurement of these materials is an additional, B_{2g}, peak at 353 cm^{-1} indicating bilayer material.[13]

1.5.3 Tungsten Disulfide

The Raman active modes for tungsten disulfide are observed at 346, 351 and 418 cm^{-1} for the 2LA(M), E^1_{2g}, and A_{1g} modes.[13] The ratio of the intensity of the E^1_{2g} to A_{1g} peaks was examined alongside atomic force microscopy data of island features. It was determined that, rather than the ratio of intensities of the Raman

modes, photoluminescence intensity, broadness and position were the best optical metrics for predicting material quality and thickness.

1.5.4 Tungsten Diselenide

For the tungsten diselenide species the in plane (E^1_{2g}) and out of plane modes (A_{1g}) are degenerate. Their peaks are not observable distinct from one another. This main peak is centered at 250 cm^{-1}.[13] For the tungsten diselenide, without employing high resolution techniques, we are able to use photoluminescence measurements at the direct gap energy, as well as optical contrast as a guide to identify monolayer domains.

1.6 Optical Properties of Transition Metal Dichalcogenides

The indirect to direct band gap transition, occurring with thinning the material down to a monolayer, has the biggest implications for the optical properties of TMD materials. The transition results in an increase in the quantum efficiency, for the case of MoS_2 reported in literature of 10^4, going from bulk to monolayer.[14]

Transition metal dichalcogenides are transparent at a monolayer. Their ability to transmit light is due to their subnanometer thickness. This transparency makes the TMDs ideal candidates for development of electronic skin applications. Although the TMDs are poor absorbers compared with bulk semiconductors, the applications in light emission are promising especially with plasmonic

enhancement magnifying photoluminescence intensity.[15] Their absorption of wavelengths in the visible regime is promising for photo-conversion applications, such as photovoltaics and solar hydrogen production, discussed in more detail in Chapter 4.

Chapter 2. Spectroscopy Techniques and Instrumentation

2.1 Introduction

The following chapter provides details of the execution of measurements later shown in the work. Spectroscopies discussed follow the order of the research chronologically, and by chapter. The sections are meant to give specific context to set-ups made in our lab for the case of the chemical vapor deposition growth and the uniaxial strain measurements, and set up commercially for the other techniques discussed.

2.2 Tube Furnaces

The chemical vapor deposition included in the growth studied by the author was carried out in resistively heated clamshell style Lindberg furnaces, types 55031-S and 54342. These programmable controllers heat in a single zone, so multiple controllers are used for growths done in the four heat zone furnace. The process tube material was fused quartz, selected for its superior thermal stability and sourced from Technical Glass Products. Tube diameters measured 20 x 25 mm and 46 x 50 for each of the furnace types, respectively.

2.2.1 Gas Flow Regulation

The regulation of carrier gas flow rates was maintained by standard regulators at the cylinder as well as Dwyer flow meters upstream, allowing control of the flow rate. Regulators for low flow processes were tunable in the range of 0.1- 1.0 ft^3/ hr.

For high flow and purging gas control, flowmeters allowing up to 5 ft^3/ hr were used. Swagelok style connections with stainless steel tubing were used for hydrogen gas lines and Teflon tubing for all other process gases.

2.2.2 Temperature Control

The process developed in our laboratory is robust, meaning that with constant process gas flow, reagent weight and position within the furnace zone there can be temperature variations among successful growths of monolayer, highly photoluminescent transition metal dichalcogenides.[2] Although variation in temperature can still result in successful growth, the ability to precisely control temperature is a crucial tool in developing synthesis protocol, especially when implementing precursors in new processes. Thermocouples, whose length was shielded with protective ceramic tubing, contacted the exterior surface of the fused quartz tube in the center of the length of the furnace, at the point of the zone reaching the highest temperature. The thermocouples connected as a process sensor input to Honeywell UDC 3000 Versa Pro controllers powered in series, each controller powering a distinct heating zone, or for the single zone heating case a distinct furnace. The Honeywell controllers operated using proportional with integrated and derivative control (PID) known to be more energy efficient due to duty cycling of the power during the proportional band. Multiple independent PID tuning constants allow for the use of a single program for ramping and then holding temperature constant at a specific set point. Multiphase power cables were built to

custom lengths and phase to accommodate the location and availability power outlets in our laboratory spaces.

2.2.3 Vessels

The reduction of the transition metal species from an oxidation state of M(VI), six, to M(IV), four, is an endothermic, nonspontaneous reaction. All parameters that can facilitate the conversion of the transition metal oxide precursor to a transition metal dichalcogenide must be optimized. For that reason, we experimented with the use of molybdenum metal precursor and substrate holders as well as alumina crucibles. The alumina crucibles were determined to yield a greater reliability due to more uniform heating and cooling.

The placement of the substrate is also critical to the synthesis of monolayer material. In previously established methods, the substrates were placed, SiO_2 side down over the alumina crucible containing the transition metal oxide. In the growth process outlined in this work the inner walls of the tube served to support the substrate downstream from the transition metal oxide boat. The new configuration resulted in less metal oxide precipitating on the substrate.

2.3 Raman Spectroscopy

Nonresonant Raman measurements, taken with a 532 nm laser, are shown throughout this work to demonstrate composition as well as to validate thickness. The spectroscopy technique gives the frequency shift of the vibrational modes of

chemical bonds at values specific to the given material, and in the case of two-dimensional materials, sensitive to thickness. This optical effect takes place when a materials phonon modes are strong enough to scatter incident photons inelastically.[16] More specifically, the vibrational modes of the chemical bonds with a certain “spring constant”, κ, become excited by a monochromatic excitation source (photons) and recombine into a lower energy state emitting a photon with either lower (Stokes) or higher (Anti-Stokes) frequency. That vibration between bonded atoms which is significantly altered by the excitation, is the active mode. Selection rules may also be interpreted as the degree to which the mode is polarized by the excitation, an active mode having a great degree of polarization. Disallowed vibrational modes will be suppressed by selection rules for typical (nonresonant) Raman scattering. Using an excitation source with a frequency which matches that of the electronic band gap, or is resonant with the electronic transition energy in the subject semiconducting material, allows more scattering events to occur enhancing intensity and allowing modes beyond the first order zone-center to be observed.[17]

2.4 Photoluminescence Spectroscopy

Photoluminescence spectroscopy was conducted under ambient conditions to measure the optical band gap of the TMD materials, and thus the intensity and distribution of the radiative recombination events at the direct gap energy allowing determination of material quality and thickness as discussed in Chapter 1. The

excitation wavelength for all spectra reported here is 532 nm, which is sufficient in energy to measure all of the MX_2 (M= Mo, W; X= S, Se) materials. To collect a broader energy range, for optimal peak fitting, the 600 mm^{-1} diffraction grating was selected. Mapping to generate photoluminescence images was executed by scanning the Märzhäuser stage in increments as small as 0.150 µm. Fitting of the data is done to produce intensity (a. u.) and energy (eV) images based on a Gaussian fit of the spectra carried out in Wolfram Mathematica software.

2.5 Atomic Layer Deposition

Atomic layer deposition is a powerful tool in thin film synthesis. The flexibility to deposit highly conformal titanium dioxide films of a particular phase at a growth rate of less than 0.5 Å/ cycle allows a high degree of precision in the bottom-up fabrication model presented. Atomic layer deposition was carried out on a Cambridge Nanotech Savanah 100 instrument in the Center for Nanoscale and Engineering at UC Riverside. The surface passivated process allows deposition of oxide materials in a layer by layer manner. The highly reactive gaseous precursor used for the purposes of titanium dioxide deposition was tetrakis-dimethyl-amido titanium (TDMAT). The specific parameters were deposition at 300 °C with a TDMAT pulse of 0.1 s and O_3 purging for a final thickness of 30 nm.

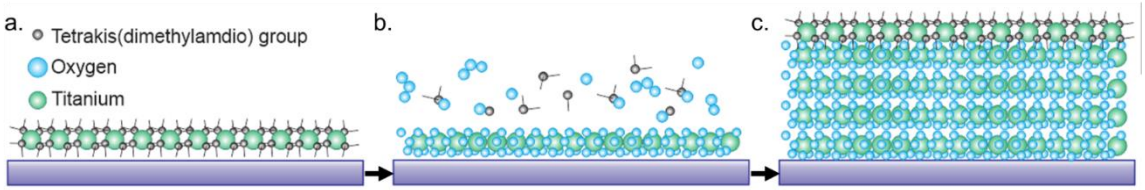

Figure 2.1: a. Shows the TDMAT precursor deposited on the surface of the substrate. b. Ozone gas is used to purge the chamber after the TDMAT pulse cycle has completed and reacts with the organic species on the surface leaving a layer of TiO_2. c. The process of pulsing and purging is repeated such that film of the desired thickness is formed in a layer-by-layer manner

2.6 Photoelectrochemistry

Experiments carried out to analyze the efficacy of the transition metal dichalcogenide based system, designed for hydrogen evolution through the water splitting reaction, are based on the model for heterogeneous semiconductor photocatalysis. The semiconductor electrode of interest is tested using the characterization techniques and reaction mechanisms described here. The results are presented and further discussed in Chapter 4.

2.6.1 Water Splitting Reaction: The Reduction Case

The reduction of water has been investigated as a route to produce hydrogen from water, an abundant source. The ideal energy needed to split water can be derived from the reduction potential given in Equation 2.1 and 2.2.

$$Cathode: 2H^+_{(aq)} + 2\,e^- \rightarrow H_{2(g)} \quad \mathrm{E^o\,red} = 0.00\,\mathrm{V} \tag{2.1}$$

$$Anode: 2H_2O_{(l)} \rightarrow O_{2(g)} + 4H^+_{(aq)} + 4\,e^- \quad \mathrm{E^o\,ox} = -1.23\,\mathrm{V} \tag{2.2}$$

The value, $E°_{cell}$, of -1.23 V is representative of the cell at standard conditions of 25 °C and a pH of 7 derived from the Nernst equation in 2.3.

$$\Delta G° = -nFE° + RTlnk \tag{2.3}$$

In order to closely probe the efficacy of a single electrode in the water splitting cell, it is common practice to use an electrolyte which drives formation of the hydrogen gas according to Le Châtelier's Principle. For the case of water reduction, 0.5 M H_2SO_4 is commonly used. The catalyst material, MoS_2, is impervious to oxidation from the sulfuric acid as is the silicon dioxide terminated silicon surface. Changing the concentration of hydronium in solution and the addition of a reference electrode requires a recalculation of the $E°_{cell}$. For standardization purposes, the values for potential reported in photoelectrochemical experiments are calculated relative to the reversible hydrogen electrode (RHE).

The Nernst equation can be rewritten as:

$$\mathrm{E}_{RHE} = \mathrm{E}_{Ag/AgCl} + 0.059 \times \mathrm{pH} + 0.197 \tag{2.4}$$

$$\Delta \mathrm{G} = \mu \mathrm{H}_{2(g)} + \frac{1}{2}\,\mu \mathrm{O}_{2(g)} - \mu \mathrm{H}_2\mathrm{O}_{(l)} \tag{2.5}$$

$$= \Delta \mathrm{G}° + \mathrm{RTln}\left(\mathrm{p}_{\mathrm{H}_2}\,\mathrm{p}_{\mathrm{O}_2}{}^{\frac{1}{2}}\right) \tag{2.6}$$

Because the system is not lossless, the experimental value for potential necessary to initialize the reaction will differ from the ideal 237 KJ/mol H_2. The system may be described by chemical potential or partial pressure as in Equations 2.5 and 2.6. The difference in voltage is referred to as the overpotential. Photocathodes lower the overpotential necessary for the reaction to take place through photogeneration of reactants, electrons. But, in reality, an overpotential is

often still required. To better understand the effect of applying a bias to the photocathode, consider the surfaces of the following system in the electrolytic solution.

In heterogeneous catalysis with semiconductor photocathodes, the effect of an applied potential is seen in the population of carriers within the space charge region. With the potentials more positive than the flat band potential of our cathode, the band bending at the surface represents accumulation. The depletion case arises when the potential applied is more negative than the flat band potential as shown in Figure 2.2 a., b. At the flat band potential there is no current, dark or irradiated, because there is no electric field to separate the charge carriers.

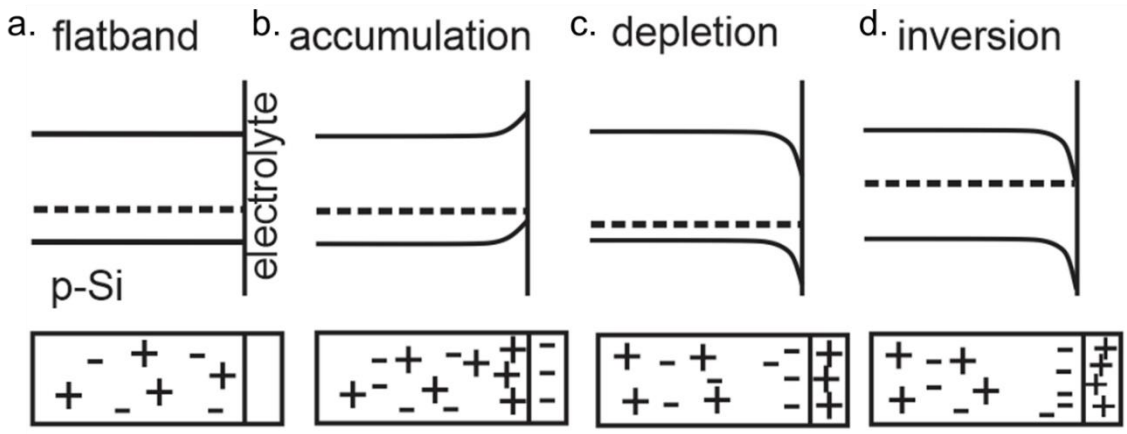

Figure 2.2: Shows the band alignment of a semiconductor in contact with its electrolyte at the cathode in a PEC cell. a. Before a potential is applied, the Fermi level is defined by the intrinsic charge carrier concentration for the p type silicon. b. When a positive potential is applied the bands bend upwards, decreasing the amount of electrons available in the space charge region and increasing the concentration of the majority carrier c. the negative bias case causes band bending in the space charge region which decreases or depletes the hole concentration. d. The concentration may then become inverted, such that there are more electrons present than holes in the space charge region.

2.6.2 Photoelectrochemical Cell

The photoelectrochemical cell was a commercial cell sourced Teflon/ stainless steel cell with sapphire windows from Zahner. The reference electrode, which balances the potential in the solution, was Ag/AgCl. The counter electrode ensures the limiting step for our case is occurring at the working electrode where water reduction occurs. The counter electrode used here was a platinum coil. The light source used was an AM 1.5 lamp, which provides the average spectra of solar radiation filtered by the atmosphere at an intensity for the sun's zenith at 80 degrees. To record the current as a function of potential, we used a Gamry potentiostat.

The samples were electrically connected to the potentiostat by scratching through the native oxide and then using an indium gallium (liquid) eutectic metal back contact sealed and kept in place by Kapton tape as seen in Figure 2.3 and contacted with a copper wire protected from the sulfuric acid electrolyte solution by a Kapton coating.

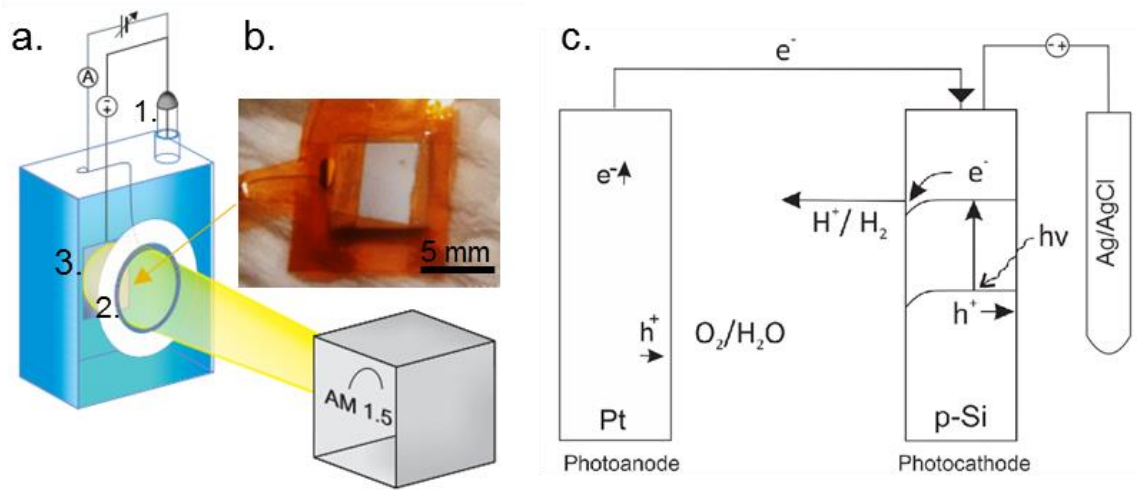

Figure 2.3: a. Above, at left is a photoelectrochemical cell with 1. Ag/AgCl reference electrode, 2. platinum counter electrode and 3. p-silicon based working electrode. b. The photograph shows the working electrode with edges and other non-active surfaces isolated by Kapton tape c. The whole cell with electrodes connected externally, with bias applied to the cathode with respect to the reference electrode, all submerged in the electrolyte solution.

The measurements of photocurrent were done in a three electrode setup with a reference, working and counter electrode. This setup allows for the potential and current to be measured independently from one another, or rather from separate electrodes. In the three electrode setup, current will flow between a working and counter electrode. The counter electrode in the Zahner cell was a platinum coil. The reference electrode in this scenario ensures that the bias applied to the working electrode will not be shifted by the reduction reaction at the working electrode. The bias at the reference electrode remains independent of the catalysis. The bias applied to the working electrode and stabilized by the reference electrode results in a current collected from the counter electrode.

2.6.2.1 Use of Potentiostats for Electrochemistry

The use of a potentiostat in electrochemistry allows the application of a controlled bias between the working electrode and a reference electrode. It allows resolution of currents which are changing rapidly as the reaction begins to occur. In a three electrode setup the role of the potentiostat is to maintain a specific potential between the reference electrode and the working electrode. This bias between the working electrode and reference electrode is compared to the voltage set by the user. If the values do not match, the system is balanced by application of current to the counter electrode. The potentiostat behaves as an operational amplifier.

2.6.3 Current Density and Capacitance Calculations

Linear sweep voltammetry (LSV) allows the potential to be swept linearly with respect to a known value electrode, the reference electrode, using a potentiostat. From this measurement technique, we can ascertain reliable current-voltage curves. Modulating a light source while collecting the current-voltage curve we obtain photocurrent density metrics for our materials.

Chronoamperometry was used to give an endurance metric to the electrode materials being tested. Stability of materials in the electrolyte, under illumination, over an extended period of time is measured with the potential held constant by the potentiostat with respect to the reference electrode.

The Mott-Shottky measurement is also used in the photoelectrochemical work presented. The donor density can be calculated from the slope of the measurement. If one considers the capacitance of the system, then the total capacitance at the electrode arises from the sum of the space charge capacitance and the double layer capacitance in series as seen in Equation 2.7.

$$\frac{1}{C_{Total}} = \frac{1}{C_{SC}} + \frac{1}{C_{DL}} \tag{2.7}$$

The Helmholtz double layer capacitance will be much larger than the space charge capacitance. With space charge capacitance, $C_{SC,}$ going to zero, the capacitance is as seen in Equation 1.7 to be primarily arising from Helmholtz layer, C_{DL}, which can be calculated using Equation 2.8. Values for the inverse capacitance and flat band potential are determined experimentally through analysis of the Mott Shottky plot. This allows the carrier density at the interface to be calculated.

$$\frac{1}{C^2} = \frac{2}{\varepsilon\varepsilon_o e N_A}(-E + E_{FB} - \frac{kT}{e}) \tag{2.8}$$

$$Volmer: H^+ + e^- \rightarrow H_{ads} \tag{2.9}$$

$$Tafel: H_{ads} + H_{ads} \rightarrow H_{2(g)} \tag{2.10}$$

$$Heyrovsky: H^+ + e^- + H_{ads} \rightarrow H_{2(g)} \tag{2.11}$$

More valuable information can be obtained by analyzing the Tafel plot shown in Chapter 4. The exchange current density, or background current, is determined from the value of the log of current density (J) at a potential of zero. The Tafel plot, showing log of J with respect to potential swept linearly, also gives valuable

information about reaction mechanisms taking place. The three reactions specific to the catalysis for the HER are the Volmer (Equation 2.9), Tafel (Equation 2.10) and Heyrovsky (Equation 2.11) mechanisms. The slope of the Tafel plot is indicative of which reaction mechanisms are dominant in the system.

2.7 Scanning Photocurrent Microscopy

Lateral current decay, at a range of biases, on the photocathode of the three electrode system described in Chapter 4, was characterized by scanning photocurrent microscopy (SPCM). The current was measured by the Gamry potentiostat, consistent with measurements done for broad area polarization curves. The Zahner PECC cell could not accommodate the working distance of our objective, so an open petri dish was used with platinum mesh as a counter electrode. The excitation source was a HeNe laser (633 nm) focused through a 50X objective. The sample and stage were rastered with respect to the laser. The laser power used for the measurements shown in Figure 4.7 was measured to be 0.4 µW, with a spot size of 1µm.

2.8 Atomic Force Microscopy

This versatile nondestructive scanning probe microscopy (SPM) technique, first appearing in publication in 1987, can resolve features vertically on the order of 100 Å.[18] Non-contact mode atomic force microscopy (AFM) was used to determine the

height of features on the sample. The AFM uses a Lennard-Jones potential interaction, between two extremely close objects, to resolve the topographical features of a surface. In AFM, piezoactuators oscillate a thin cantilever at its resonant frequency in close proximity to a surface. The amplitude of the resonant oscillation is held constant and changes in the frequency of the oscillation represent a change in topography on the surface of the sample. An intense diode reflects off the center of the cantilever tip onto a photodetector. The changes in the deflection of the tip caused by repulsion, as happens when the cantilever is scanned across a bulky feature, are measured by changes in the reflected angle of the diode onto the four quadrant detector manifested as a voltage increase in a specific quadrant.

With commercial adaptation an AFM was also used in the surface microscopy work discussed in detail in the next section. The AFM work relating to catalysis was done using a Bruker instrument at Sandia National Laboratory while characterization of height and roughness done for all other portions of the work was done using an Asylum MFP-3D at the Winston Chung Hall Global Energy Center at UC Riverside.

2.9 Kelvin Probe Microscopy

Amplitude modulated kelvin probe microscopy (AM-KPFM) commonly referred to as surface potential microscopy measures the differences in contact potential laterally across a substrate. The contact potential difference is proportional to the

work function difference. When two materials are brought into contact, diffusion of electrons will proceed toward the material with the higher work function and this creates the contact potential difference or “built-in potential” referred to in the document.[19] Kelvin probe microscopy can be carried out with minor adaptations to an atomic force microscope (AFM). And, in a fundamental sense, the system can be viewed as a capacitor. The AFM tip and conductive sample comprise the two parallel plates. As the AFM tip oscillates in non-contact mode at its’ resonant frequency the capacitance will change with respect to time, and there will also be charging and discharging oscillations at the resonant frequency, an AC signal. Finally, any noise arising from outside the system is negated by using an externally applied DC voltage and setting it to the V_{CPD}.[20]

$$i(t) = (V - V_{CPD})\frac{dC}{dt} \tag{2.10}$$

So, while the AC voltage is applied to the tip at the resonant frequency of the AFM tip and the DC bias is reduced until the oscillation amplitude is zero or rather the V_{AC} term in Equation 2.11 is brought to zero. Now, scanning the tip across the sample any change in the DC bias represents a change in the contact potential difference.

$$\Delta V = V_{DC} - V_{CPD} + V_{AC}\sin(\omega t) \tag{2.11}$$

When the circuit is connected, an electrical force exists between materials with a V_{CPD}. This force can be calculated using the change in the capacitance between the tip and sample with respect to the tip-sample distance multiplied by the contact potential difference seen in Equation 2.12.

$$\mathrm{F}_{el} = -\frac{1}{2}\frac{\partial C}{\partial z}(\Delta V)^2 \qquad (2.12)$$

With AM-KPFM measurements have a significant tip contribution. However, with the AM-KPFM there is an advantage over higher spatially resolved frequency modulated kelvin probe force microscopy measurements that lower AC voltages can be used to achieve improved resolution of the energy[21]

It is possible from this microscopy to create an image of the surface potential difference of a sample with different surface composition. In the case of these experiments; silicon, molybdenum disulfide, titanium and platinum were evaluated (Chapter 4). A conductive tip was scanned in non-contact mode with the sample grounded via an indium gallium eutectic liquid back contact. The AFM chamber was purged with nitrogen to eliminate the effects of adsorbed water on the surface potential measurements.

2.10 Uniaxial Strain Application

Strain was applied in both tensile and compressive modes by deflecting thin film membranes such that the microstructure of interest is centered at the apex of the bend Figure 2.4. At this apex, the strain of a convexly deflected film is in uniaxial tension on the top surface of the substrate or compression on the bottom surface of the film. Precise control of the deflection was allowed through use of a piezoelectric stage. Radii of curvature were determined by the x-z coordinates of the focal point of the filtered laser on the surface, at each bending iteration, fit to a

quadratic curve. The radius of curvature combined with thickness of the MMA substrate slab, measured by the focal point of the top and bottom of the membrane give the necessary metrics to determine the applied strain, positive for tension, negative for compression using Equation 1.1. [22] Typical thicknesses of the film substrate were 0.2 mm with the encapsulation layer being 200 nm as calculated from an rpm of 4000.

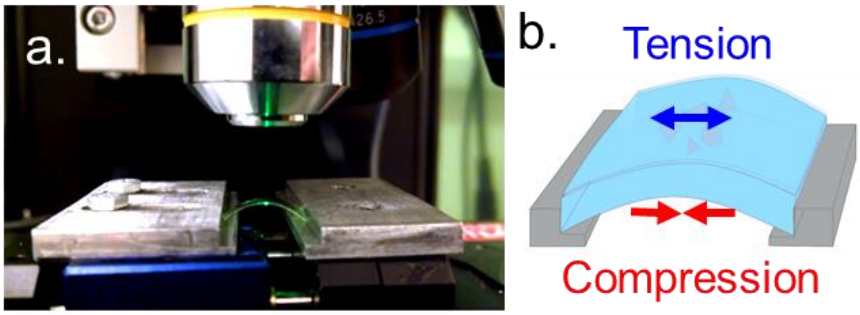

Figure 2.4: a. A photograph of the membrane on a micro positioning stage in the optical setup with a 10x objective in focus on the apex of the sample surface. b. The sample, at the apex of the curve is in complete uniaxial tension (blue) in the top layer, and complete compression (red) in the bottom layer.

The TMD materials were bound to the flexible polymeric substrate by a top encapsulation layer of MMA to ensure conformal bending on the atomically thin microstructures and to prevent lift off. The top layer is of inconsequential thickness relative to the total thickness of the film.

$$R_c = \frac{\left(1 + \left(\frac{\partial y}{\partial x}\right)^2\right)^{\frac{3}{2}}}{\frac{\partial^2 y}{dx^2}} \tag{2.13}$$

$$\varepsilon = \frac{\tau}{R_c} \tag{2.14}$$

Chapter 3. Synthesis of Transition Metal Dichalcogenides

3.1 Introduction to Growth Process: Chemical Vapor Deposition Growth of Monolayer Transition Metal Dichalcogenides

The investigation of photocatalytic and optical properties transition metal dichalcogenides in this thesis is supported by the chemical vapor deposition synthesis done within our lab and as described in this chapter. However, the synthesis also stands on its own as an important study. The ability to fabricate large monolayer crystallites, as well as films of the two dimensional materials, offers a promising route to scale-up for industrial applications. Chemical vapor deposition synthesis also has the key advantage of chemical tuning through alloying with another chalcogenide or transition metal species. And, the ability to study a domain of a material with uniform thickness makes this route highly desirable to study the physics of these thin systems.

The methods for growth presented in this work, and carried out on the substrates outlined in Sections 3.1.1 and 3.1.2 of this chapter, are classified according to the chalcogenide source. First discussed is an all powder based method depicted in the top growth tube in Figure 3.1a. The next method looks at use of liquid precursors in direct proximity to the substrate and transition metal oxide powder, as depicted in Figure 3.1b. And lastly, a method using controlled exposure to chalcogenide vapor is studied show in Figure 3.1c.

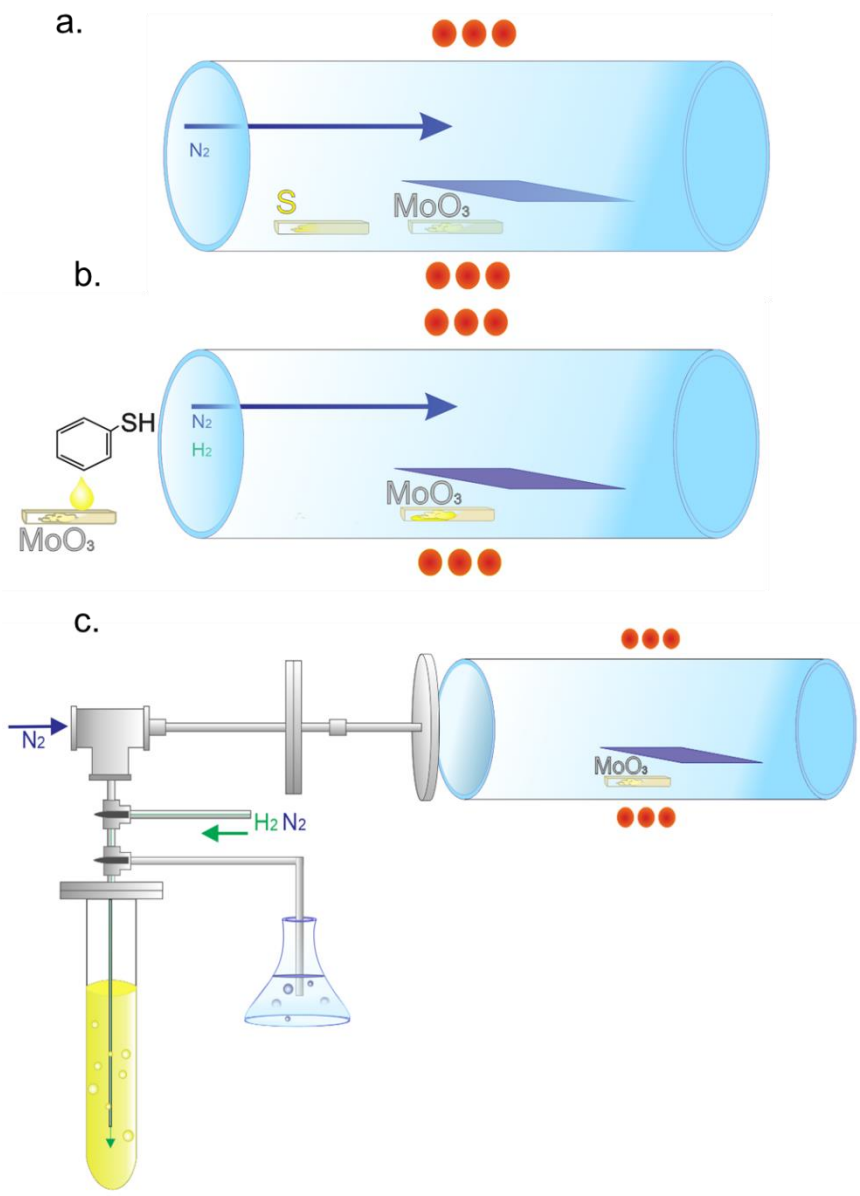

Figure 3.1 A fused quartz tube heated in a single zone depicting three different growth styles used in the CVD synthesis presented. a. Elemental sulfur powder is placed upstream in a cool zone of the furnace with the molybdenum oxide in the center of the heating zone, with the substrate supported by the inner walls of the tube furnace and nitrogen serving as a purge and carrier gas. b. In the droplet method, before growth molybdenum oxide powder precursor is saturated with liquid based chalcogenide reagents (pictured is thiophenol). c. At a specific, peak temperature, the valve to the liquid organic chalcogenide reagent is opened and gases, which bubble through the pre-purged capillary, enter the tube furnace and react with the molybdenum trioxide powder precursor, which is in the same configuration as for previous growths.

3.1.1 Powder Based Growth Techniques

Growth of transition metal dichalcogenide materials were produced using inexpensive powder reagents in a sealed quartz tube with process gases to control oxidation and exposure of the substrate to the reagents present. In the development of TMD materials this was a foundational first step to yielding the monolayer material. A notable characteristic of the growth of these single layer materials is that the processes are robust, allowing for a 50 °C variation in temperature and variations in hold times as well.[2] In this section, we establish the standard method of fabrication used for the sulfide TMDs and discuss how tuning these parameters further, using methods discussed here provides conditions yielding selective growth of either highly crystalline islands or films.

The chemical vapor deposition process occurs in sealed fused quartz tube furnaces depicted in Figure 3.1a. Powder precursors prove to be a reliable, cost effective and low-risk exposure option as reagents for CVD growth of some TMDs, specifically molybdenum and tungsten disulfide. Growth of these materials using powder-based precursors can result in triangular islands on the order of tens of microns, or monolayer films which span hundreds of microns along a single direction shown with processing conditions in Figure 3.3. To achieve these large scale growths, as seen in Figure 3.4 for film, the powders' partial pressure is crucial. The stoichiometric availability of metal and chalcogenide species during growth plays a key role. For this purpose, powder masses and reagent temperatures during growth were tuned. Insufficient chalcogenide pressure during

the growth resulted in incomplete reduction of the MoO_3 reagent to a molybdenum oxisulfide, evidenced by the characteristic rectangular shape seen in Figure 3.2.[23] Control of the chalcogenide pressure in an ambient pressure, single-zone furnace required precise placement of the chalcogenide boat near the onset of the heating elements such that it would only begin to melt and vaporize at its' melting point of 200 °C when the central zone reaches its' peak temperature. Further control over the partial pressures was achieved by standardization of weight of chalcogenide precursors, gas flow and ramp rate. The molybdenum or tungsten oxide is placed in a separate boat in the center of the heating zone, because it requires temperatures above 600° C to become appreciably present in the vapor phase and to be reduced to MoS_2 as it is deposited on the substrate according to Equation 3.1.

$$2\,MoO3 + 7\,S \rightarrow 2\,MoS2 + 3\,SO2 \qquad (3.1)$$

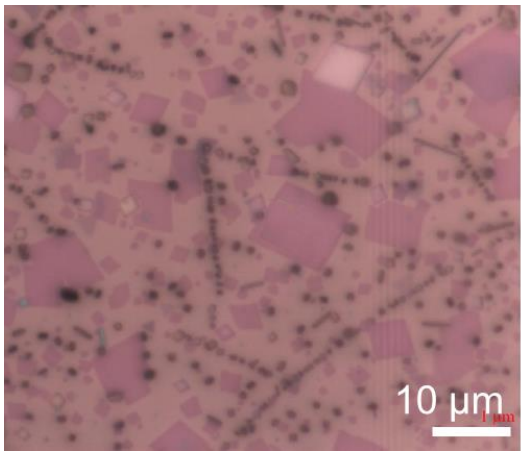

Figure 3.2: Shows molybdenum oxisulfide square-shaped bulk crystallites as well as molybdenum oxide nanorods, an undesirable byproduct of the CVD growth process resulting from incomplete reduction of the transition metal oxide precursor which we minimize through process conditions.

Process gases act as important carriers to populate the transition metal oxide rich areas with vaporized chalcogenide species and can actively suppress oxidation. Their role is also significant in controlling the temperature of the substrate, to assist in halting the growth without over-shooting the desired monolayer thickness. In this powder-based process, an excess of sulfur is used to compensate for the reagent lost during ramping of the temperature due to its low melting point. The excess chalcogenide powder also reduces the formation sulfur vacancies in the materials.

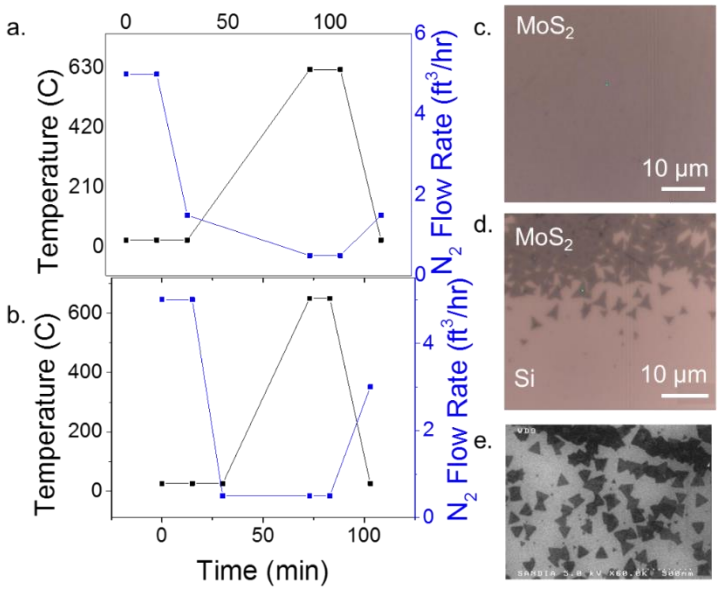

Figure 3.3: Synthesis conditions for film a., c. and island b., d. morphologies using the all powder-based synthesis technique on 100 nm SiO_2/ Si substrate. d. Optical images combined with e. electron microscopy shows the range of island sizes spans from 5 µm to 100 nm.

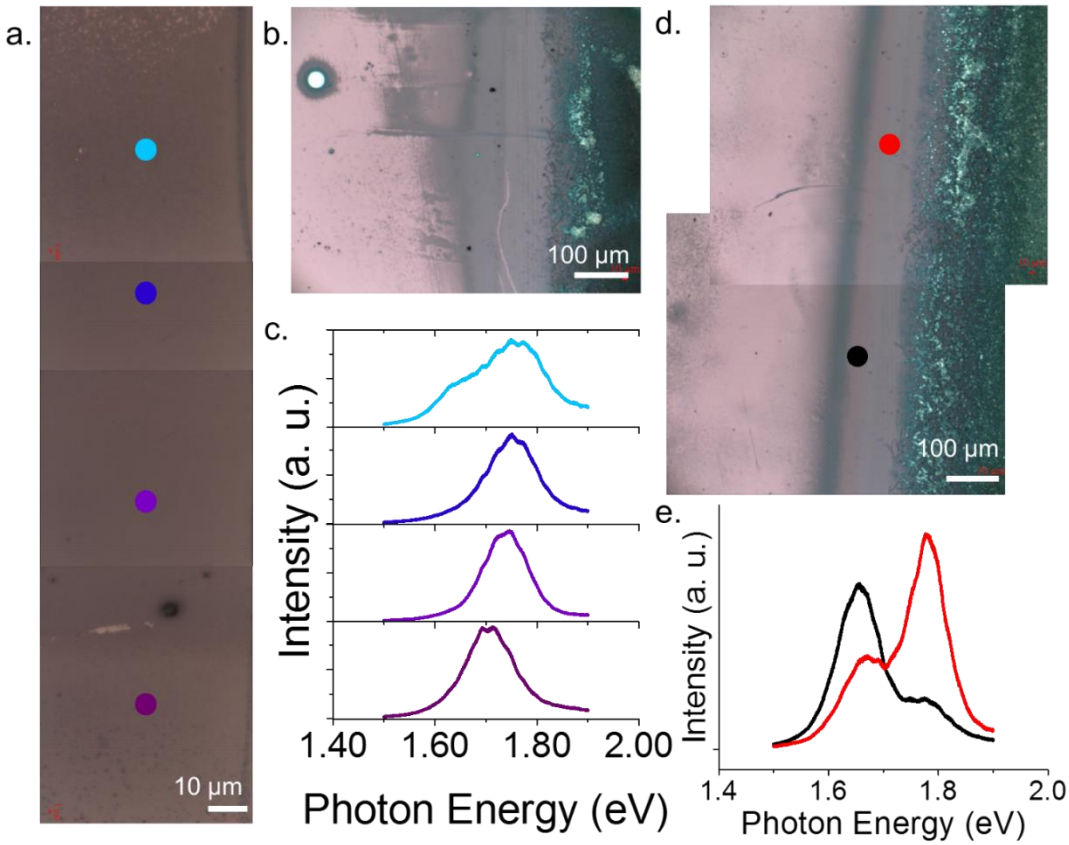

Figure 3.4: CVD MoSSe growth showing a monolayer film spanning over a millimeter with varying sulfur selenium composition as identified by photoluminescence measurements. a. Shows higher resolution optical images stitched of the area of b. the center image. c. The photoluminescence at corresponding point in image a. are shown in the stacked plot d. Film of varying composition spans over one millimeter along the length of the oxide edge, e. with higher selenium (black) or sulfur (red) content shown in PL spectra.

3.1.2 Liquid-Powder Based Growth Techniques

3.1.2.1 Droplet Method

The second technique developed for achieving high quality growth, which we discuss here, incorporates liquid precursors in a droplet style. Liquid-based chalcogenide reagents offer the advantage of a cleaner approach to synthesis. They can reduce the chance of abrasion to the amorphous oxide substrate

surfaces that occur through the use of particle-based methods, and which will lead to shortcuts on fabricated devices. The use of liquid precursors is also a step in the direction of scalable, industry-ready materials. Benzenethiol and carbon disulfide were both studied here in the growth of MoS_2.

Droplet style growth saturates the same metal oxide powders used in the previous method. The transition metal oxide is placed in the ceramic boat. Then, as shown in Figure 3.1b, drops of the organic sulfur precursor are placed directly into the molybdenum oxide powder before the initialization of the process. The tube is purged with nitrogen gas, then ramped to peak synthesis temperatures ranging from 630- 670 °C.

Reactant mass for molybdenum trioxide was optimized at 0.2 g for these growths. Flow rate of the nitrogen gas, after purging the tube at room temperature, was decreased to 0.1 ft^3/ hr. The best growths for both films and islands used 2 droplets of benzene thiol, which is equivalent to 0.10 mL. The remaining variable which was tuned to give different growth outcomes was the peak temperature. Growths over many substrates showed that, for this method with the parameters above, higher process temperature result in more growth. Lower temperature growths at 630 °C yield islands as seen in Figure 3.5 a.-c. More growth at temperatures above 630 °C is seen in the extension of those islands to form a monolayer film at temperatures from 630 to 667 °C as is seen in Figure 3.5 d.-f. For the range from 670- 691 °C thicker films and multi-layer islands are observed.

While molybdenum dioxide is weakly soluble in some alcohols, the molybdenum trioxide used is insoluble in the thiophenol, and it remains liquid until process temperatures are sufficient for vaporization.[24] The substrate and boat placement within the furnace is the same as for the powder based method shown in Figure 3.1a, except the elemental sulfur source is removed.

The boiling point of benzenethiol is only 169 °C, which would suggest that the chalcogenide supply will be exhausted at the temperature that the molybdenum oxide reaches its' peak partial pressure. However, the proximity of the reagents allows the molybdenum trioxide to be partially reduced, slowly, as the temperature is increasing. In order to minimize chalcogenide precursor loss, minimum flow rates are used while ramping-up and holding the temperature at its' peak. Still, some of the chalcogenide will remain in the boat during the peak temperature phase. But, most will have been vaporized and deposited on the substrate 50 mm downstream of the boat.

The availability of the chalcogenide source in direct proximity to the molybdenum oxide and substrate, as the partial pressure of the powders is increasing, aids in reducing the amount of molybdenum oxide (MoO_2), which is formed on the surface of the substrate. Using a nitrogen flow of 0.1ft^3/hr the furnace is heated to 640° C. Compared to the injection method that uses the same liquid organic sulfur precursors, but introduces them into the tube from a syringe needle, at the peak synthesis temperature; the droplet method allows greater control over

the position of the sulfur precursor in the tube. In the droplet style growth, the chalcogenide is in closer proximity to the growth substrate's surface.

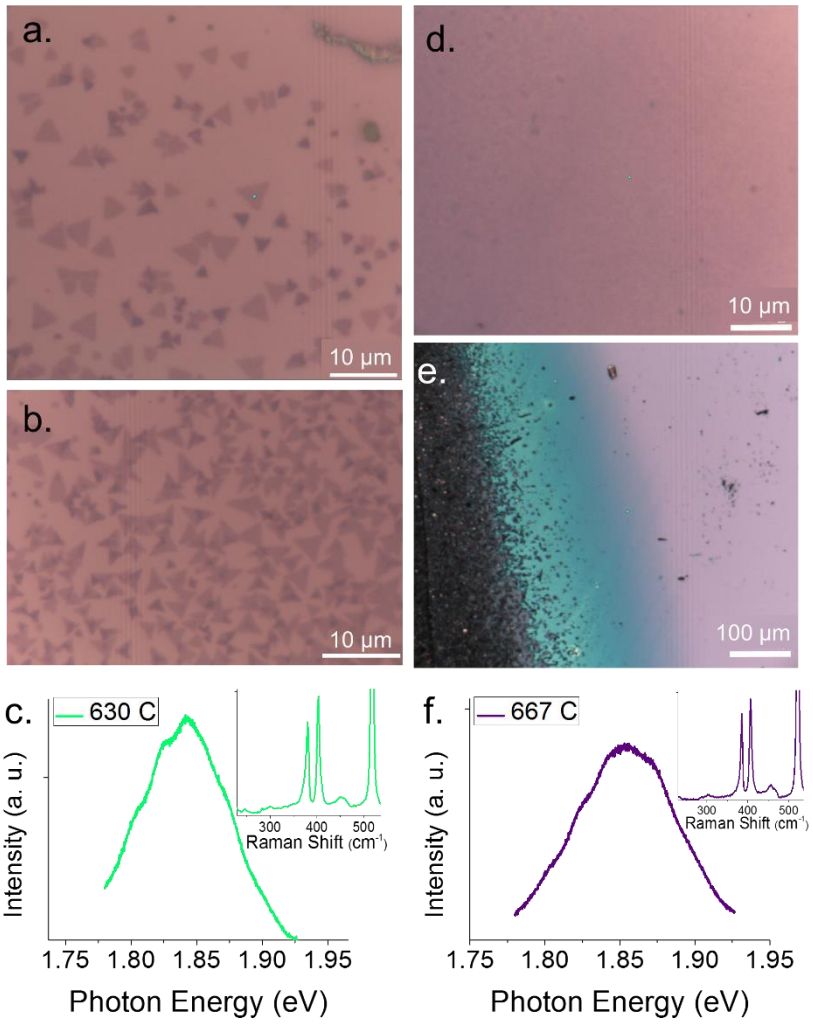

Figure 3.5: a., b. The growth of islands resulting from the droplet methods of chalcogenide incorporation with process temperatures of 630 °C. c. Photoluminescence at the direct band gap energy with complementary Raman data. d.-f. For film grown using the droplet method at 667 °C.

3.1.2.2 Bubbler Style Growth

While the droplet method showed success, the dosing of chalcogenide in that process is limited to what is provided, the liquid which is placed into the

molybdenum oxide boat, at the beginning of the growth. In order to supply a greater quantity of sulfur, which is experimentally shown to increase photoluminescence, we investigated the bubbler style growth. This style of liquid-based synthesis h allowed for greater control of the timing and dosage of chalcogenide species.

Using the setup shown in Figure 3.1c, gases were bubbled through the liquid chalcogenide precursors, carrying the vaporized reagent into the process tube containing the transition metal oxide precursor at peak temperatures. The process for the sample shown, below in Figure 3.6, uses carbon disulfide as the chalcogenide source. Hydrogen gas was bubbled through the carbon disulfide and entered the process tube at a rate of 0.2 ft^3/hr during the temperature range from 600 to 650 °C. Although the process does allow greater control over the time of release, the amount of chalcogenide is limited. This results in sulfur deficient growths, which is seen by the broad and red-shifted photoluminescence in Figure 3.6b on the island indicated by the marker in Figure 3.6a. The Raman peak separation is 18 cm^{-1} (inset of Figure 3.6b), further corroborating sulfur deficiency inherent in the process.

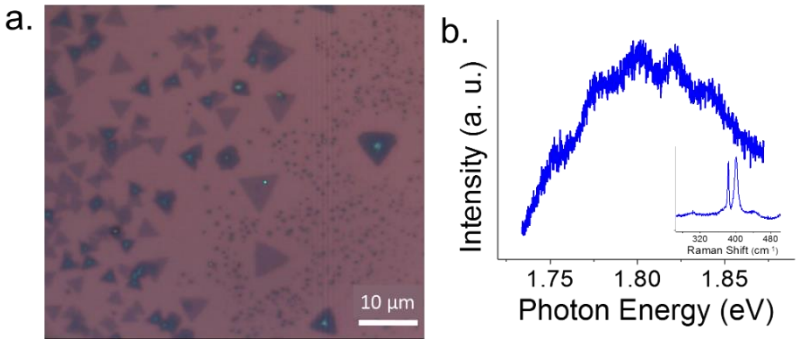

Figure 3.6: a. Optical image of islands grown by the bubbler technique with b. photoluminescence red-shifted and broad, indicating sulfur vacancies.

3.2 Growth on Alternative Surfaces

In order to realize bottom-up fabrication, for application-ready transition metal dichalcogenide systems, investigation of the growth processes must continue on novel surfaces, even after methods which yield monolayer films have already been established. An interesting characteristic of TMDs growth is their ability to form on amorphous surfaces, such as silicon dioxide. Unlike graphene and hexagonal boron nitride, TMDs form single crystalline monolayer material without aligning to a lattice of specific crystallographic direction.[25] By executing growth on functional surfaces, we create added value to the TMD on amorphous oxide model. The following studies operate from this motivation to carry out growth of the 2-d materials on substrates, which can be directly used in applications such as photoelectrodes or which minimize the process steps required to achieve the final application.

3.2.1 Graphene

Growth of molybdenum disulfide directly on graphene is of interest for device applications, where it is advantageous to avoid the Shottky barrier and associated contact resistance that is seen in the conventional metal contacts used in the semiconductor industry. With graphene, it is possible to achieve an ohmic contact to the surface of the MoS_2. This has been accomplished by others through tuning the band gap of the graphene with an applied gate bias as shown in the literature.[26]

The surface is also potentially interesting from the perspective of preparation of an electrode for the hydrogen evolution reaction, as is shown here.[27]

The graphene used in this work was grown by chemical vapor deposition on copper foil, in the lab of Dr. Ya-Hong Xie, where it was also deposited onto 300 nm SiO_2. Raman spectroscopy combined with optical imaging show a film of good continuity having the strong 2D peak, signature of single layer material, seen in Figure 3.7c. The coverage of the graphene is uniform. The coverage area of the transfer is on the scale of the substrate, approximately 800 mm, diced for multiple growths.

The growth of the MoS_2 was carried out via powder based processes in the conventional tube furnace methodology outline in Section 3.1.2. The process conditions for the TMD growth left graphene intact on the substrate. Monolayer Raman and photoluminescence spectra of the MoS_2 on top of the graphene are shown in Figure 3.7b., c.

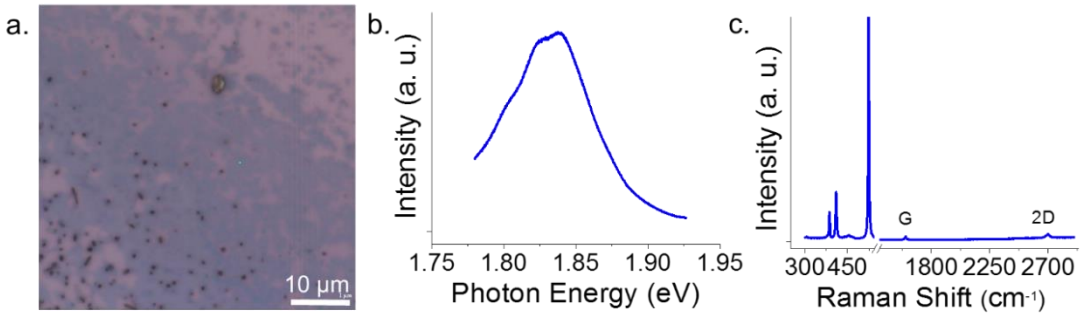

Figure 3.7: a. Monolayer molybdenum disulfide grown on CVD grown- transferred graphene on SiO_2 with b. high direct, K point photoluminescence and c. Raman shift showing weak, but present G and 2D peaks at 1598 and 2701 cm^{-1}.

3.2.2 Aluminum

As a part of the continued work towards bottom-up, device ready growth surfaces, we investigated the use of aluminum metal on our substrates. Growth of monolayer transition metal dichalcogenides on a thin oxide- aluminum surface has the distinct advantage of being readily applicable for photovoltaics (PV). To this end, research has recently shown the performance of such materials to be an interesting avenue towards realizing atomically thin TMDs in PV devices.[28]

The growth procedures for these substrates follows the powder-based model closely, with reagent weights a 1:2 ratio between molybdenum trioxide and elemental sulfur powder respectively. Substrates used here are protected aluminum mirrors sourced from Thorlabs. The substrates used in this process are highly smooth surfaces, as their original application is in optical setups. They have reflectances of 90% as specified by the manufacturer.

However, the CVD growth conditions degrade the material appreciably, resulting in a surface which is rough and nucleates multilayer growth as can be seen in Figure 3.8. The furnace for these growths is heated in four zones. The sample shown in this figure was processed at a peak temperature, in the substrate zone, of 588 °C, below the standard minimum of 600 °C used in CVD synthesis of molybdenum disulfide. This was to mitigate damage to the surface of our substrate. Molybdenum disulfide formed on the surface despite low process temperatures Figure 3.8. However, the surface is still visibly damaged and the roughness of the substrate resulting from growth consistently yields thick film. Raman spectra for

the area identified by the marker in Figure 3.8a exhibited a E^1_{2g}-A^1_g peak difference of 24 cm^{-1}. Photoluminscence spectra are quenched by the substrate.

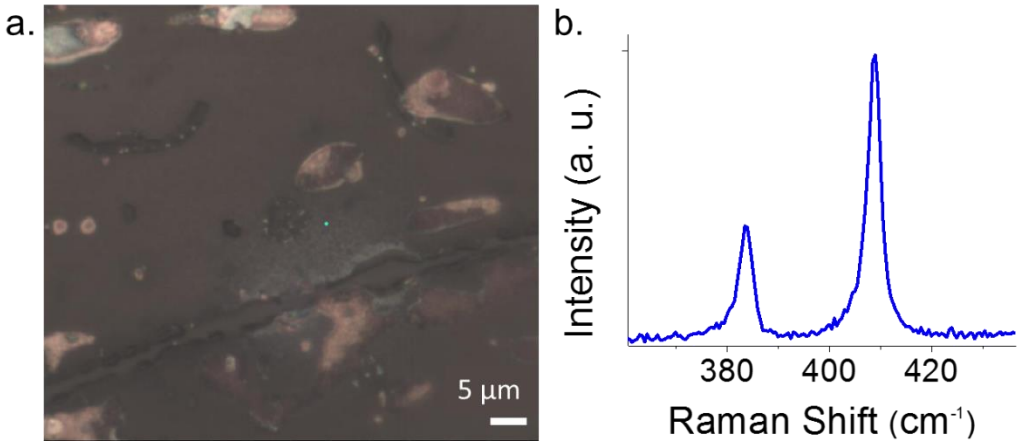

Figure 3.8: a. Optical image of aluminum sample surface with bulk molybdenum film growth (in white, center). b. Raman measurements taken at the marker in the center of image, a., confirm the > 5-layer thickness of the film grown on the roughened metal surface.

3.2.3 Passivated Titanium

In the first phase of experiments to create composite TiO_2/MoS_2 materials, 100 nm of titanium metal was electron beam evaporated onto 300nm and 80nm SiO_2 to serve as the substrate for CVD growth of MoS_2. A thin strip of the silicon substrate was masked during metal evaporation in order to leave an area where the electrode of the PEC cell could make contact. Oxygen plasma treatment was used to terminate the titanium metal surface with a layer of amorphous titania.

Growth on the titania terminated substrate uses powder based reagents for sulfur and molybdenum trioxide, with the sulfur boat upstream from the central hot zone containing molybdenum trioxide powder and the substrate. Oxidation states of titanium (IV) were characterized by x-ray photoelectron spectroscopy after

growth. The XPS data was crucial in determining the oxidation state of the titania, as Raman signal from the TiO_2 was not resolvable. It should be noted that the area scanned by XPS is several millimeters, and that the spot size of the Raman laser is 1 micron. This allows an area averaged measurement of the surface. The 2p $\frac{3}{2}$ and 2p $\frac{1}{2}$ peaks appeared at binding energies indicative of the titanium (IV) oxidation state, 458.5 and 464.5 eV, respectively. There was no oxidation state for titanium metal observed on the surface of this sample in post growth XPS measurements, signifying the thickness of the oxide is greater than the depth of the characterization technique, ranging from 3- 10 nm. For reduced TiO_2, we expect to see the reported shoulder near 258 meV, which is red-shifted from the titanium 2p $\frac{3}{2}$ peak, signature of the core binding energy of titanium (III).[29] It could be expected that the resulting material was reduced TiO_2, oxygen deficient due to the surface limited oxidation and the subsequent CVD growth. However, the XPS data in Figure 3.9 f. does not exhibit strong evidence of peak splitting.

The e-beam evaporation of titanium metal treated with oxygen plasma resulted in a conformal coating of the surface which withstood the conditions of chemical vapor deposition processing, seen in Figure 3.9 d. Thus, monolayer growth on these substrates was achieved. However, the single layer TMDs will exhibit low photoluminescence due to substrate quenching from the thin, pin-hole ridden, surface-passivated oxide. To that point, a portion of the sample was masked during the metal deposition using Kapton tape. Removal of the tape

allowed the subsequent CVD growth to occur on either the SiO_2 or anodized titanium surface. We were able to observe large islands on the SiO_2 terminated surface demonstrating process conditions were ideal for the formation of islands, however the TiO_2 terminated surface was still coated with MoS_2 film seen in Figure 3.9. The single-crystalline islands highly desired in catalysis and the study of single domains were not observed.

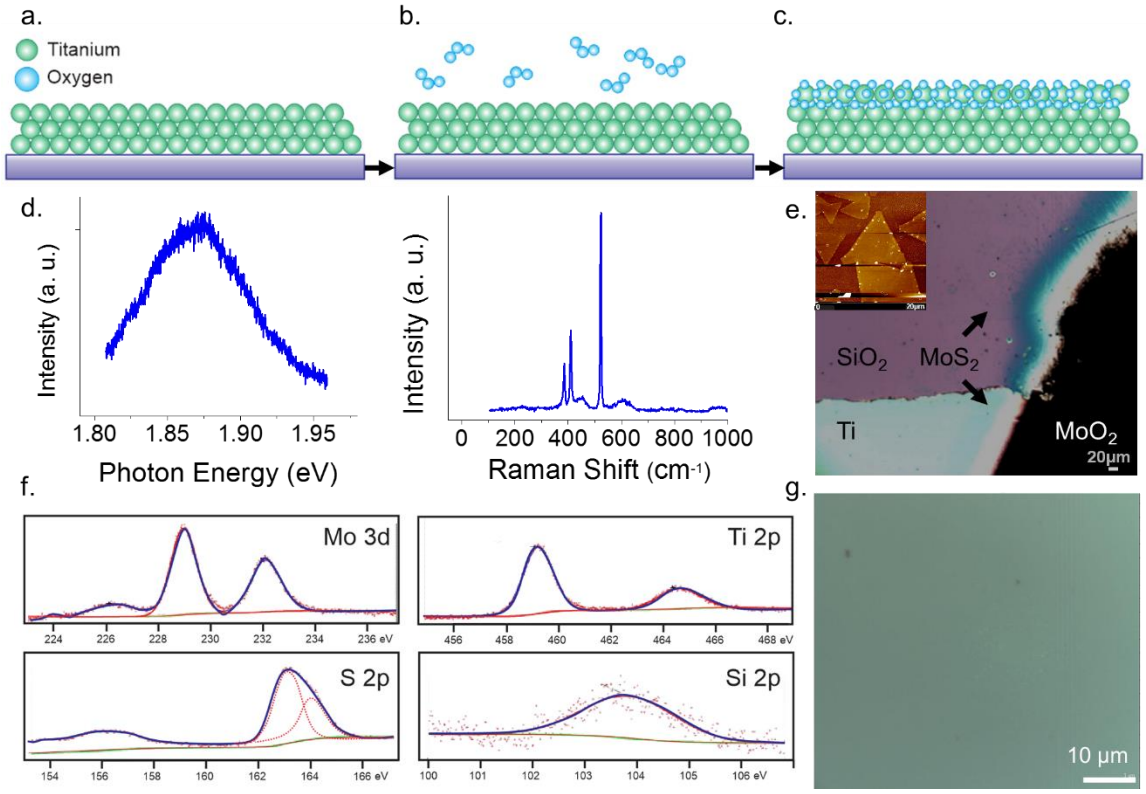

Figure 3.9: a. Schematic of titanium metal electron beam evaporated onto the substrate, b. then plasma oxidized for a c. titania terminated surface. d. Photoluminescence and Raman modes of the e. Right is an optical image of the anodized titanium substrate with an exposed area of SiO_2 found to have triangular islands depicted in the AFM image f. XPS data showing the core binding energies for Mo(IV) and Ti(IV) (top), the two 2p components of sulfur in MoS_2 bottom left and silicon 2p binding energy as it appears in SiO_2.

3.2.4 Titania

Towards the overall goal of the application-ready substrate, titanium dioxide was synthesized in a highly conformal process, which yielded a uniform surface with many monolayer molybdenum disulfide islands. Atomic layer deposition of 30 nm of TiO_2 was carried out according to the methods presented in Chapter 2. The oxidation state of the resulting film was corroborated to have core binding energies commensurate with that of titanium (IV)l by XPS measurement at an energy of 458.5 and 464.5 meV, signature of the 2p $\frac{3}{2}$ and 2p $\frac{1}{2}$ contributions, respectively (Figure 3.10).

The titania samples were grown using molybdenum trioxide powder precursor with liquid droplet of the chalcogenide source, benzenethiol, as described earlier in this chapter. The result of the growth on the ALD substrate using the droplet method was a dense array of monolayer triangles up to 4μm in size coalescing into a film with monolayer photoluminescence as seen in Figure 3.10. In many applications for these CVD grown materials, such as in field effect transistors, large, single-domains are preferred. So, while the film and small islands depicted in Figure 3.10 a., c. are too small for FET devices, their application in catalysis is ideal considering the activity of the sulfur edge sites.[30] The film formed from the coalescing islands which shows high PL allows us to probe the core binding energies of our system in limited resolution XPS measurements.

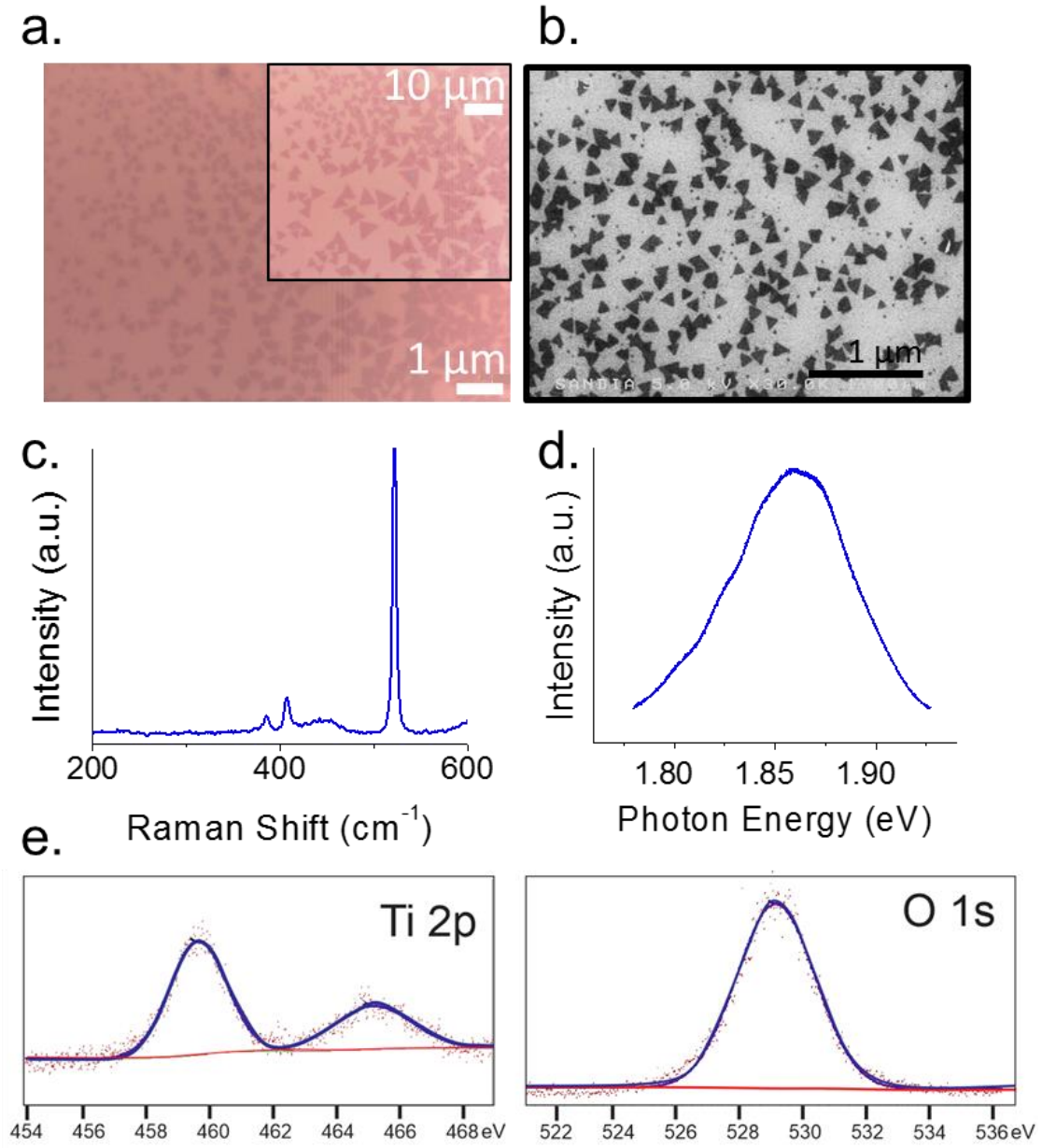

Figure 3.10: a. Islands with ranging from 10 microns to submicron edge length are shown in the optical image. b. Scanning electron microscopy allows resolution of islands with 10 nm in edge length c., d. Raman and photoluminescence of the island pictured in a. respectively. e. XPS spectra of the surface show in the left panel, the titanium (IV) core binding energies of the Ti $2p^{3/2}$ and $2p^{1/2}$ components from left to right. In the panel at right is the oxygen 1s peak, the symmetry of the peak showing the lack of vacancies which are evident in reduced TiO_2.

3.2.5 Bare Silicon on the Tunneling Oxide

The realized bottom-up fabrication of a water-splitting electrode was achieved by the growth of molybdenum disulfide, on both bare silicon and silicon having a 1.82 nm layer of rapid thermal silicon oxide, shown previously to allow tunneling of electrons through its' surface, which was prepared by NIST and supplied by Alec Talin at Sandia National Laboratory in Livermore.[31]

Growth of the samples proceeded using elemental sulfur and transition metal oxide powder. Process temperature for the molybdenum disulfide formation phase of growth was 675 °C. Forming gas (H_2/ N_2) was used to assist formation of MoS_2, inhibit MoO_2 growth and act as a carrier gas, during the ramp from 550 °C through the holding period.

The optical interference of bare silicon with a monolayer of molybdenum disulfide precludes the identification of flakes by optical contrast, as is commonly done with growth on dielectric substrates. Microstructures were located using Raman, photoluminescence spectroscopy. The morphology of the microstructures was resolved through atomic force microscopy and scanning electron microscopy seen in Figure 3.11. Photoluminescence on these samples is low in intensity for areas identified to be monolayer. For the application of photocatalysis, this is a great boon, as it signifies the excited carriers are transferred efficiently between the catalyst and the substrate. With the dim photoluminescence we can predict that our system will show lower rates of carrier recombination.

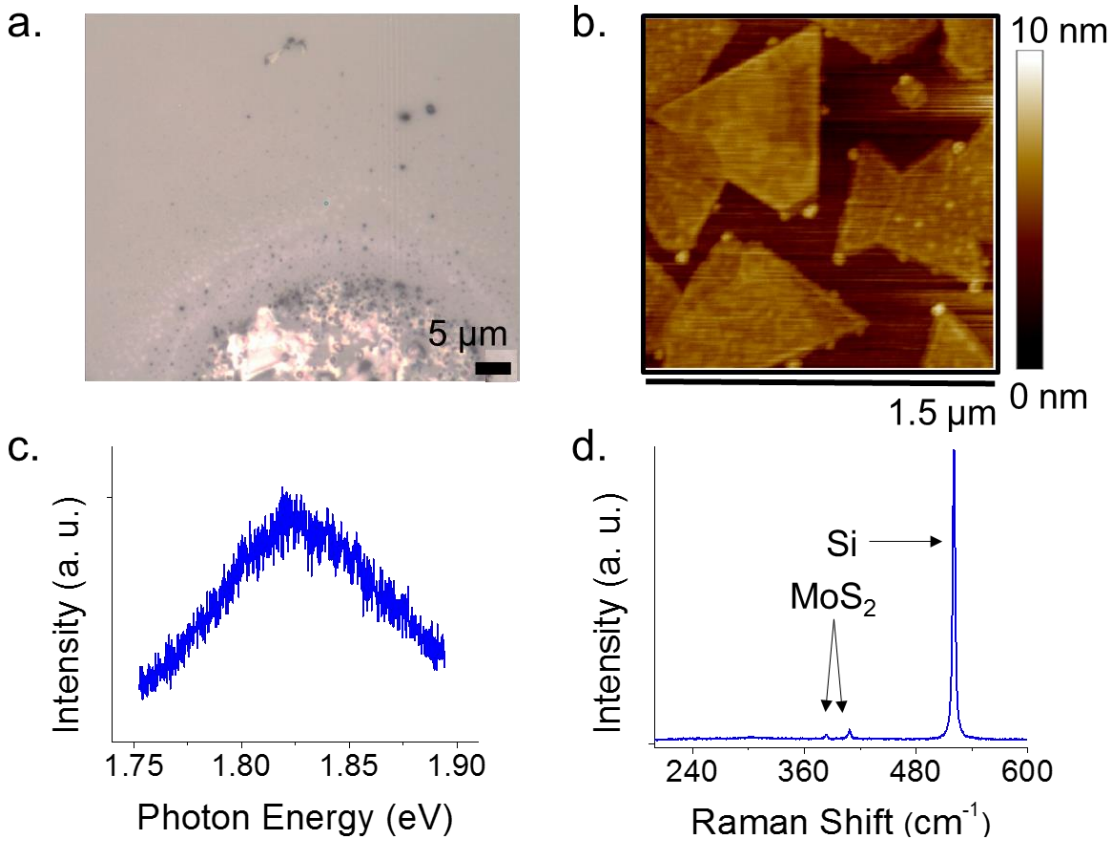

Figure 3.11: a. Optical image of clearly visible, bulk nucleation in bottom middle of image with micron scale coalescing islands radially surrounding the central bulk. b. AFM image of the surrounding area enables the morphology of the features characterized with Raman and photoluminescence microscopy to be resolved c. Photoluminscence of monolayer molybdenum disulfide dim on the ultra-thin SiO_2 substrate. d. Raman modes for monolayer MoS_2 appear weak relative to the silicon peak at 520 cm^{-1} oxide substrates.

Chapter 4. Surface Potential Assisted MoS_2 Catalysis for Hydrogen Evolution in an Economical Photocathode

4.1 Introduction

This chapter makes use of the work done to develop bottom-up, application-ready substrates to explore exciting photoelectrochemical applications of molybdenum disulfide towards an alternative, carbonless fuel source. The global energy demand forecast established in the International Energy Outlook 2016, published by the U. S. Energy Information Administration, predicts a 48% increase in world consumption over a 28-year span from 2012 to 2040. The environmental implications of fulfilling this demand using conventional petroleum based sources would exacerbate already dramatic effects of global climate change.[32] Additionally, market sensitivity to small fluctuations in the cost of energy position research on new avenues for sustainable fuels in the interest of national security.

Photoelectrochemical (PEC) experiments with MoS_2 seek to reduce water using the least amount of overpotential necessary, with photogenerated carriers from a light source driving the reaction forward to produce hydrogen gas. The PEC approach to hydrogen generation focuses on the photocathode of the photoelectrochemical cell shown in Figure 2.3 a. of Chapter 2, using a precious metal counter electrode and a p-type semiconducting material as a substrate for testing effectiveness of the catalyst.

4.2 Materials System as an Economic Photocatalyst

A key to photoelectrochemical water splitting yet to be resolved is development of an alternative to noble metal catalysts. MoS_2 has been considered as a catalyst for water reduction for several decades nearly forty years.[33] An understanding of the electronic properties of MoS_2 upon thinning to few, and monolayer has fueled a renewed interest in implementing this traditional material in PEC experiments.

The approach presented here is focused on an ultra-low cost heterogeneous S-I-M-S (SIMS) system using earth abundant and non-toxic materials. In the system presented, silicon, terminated with an ultra-thin rapid thermal annealed oxide absorbs light, with an absorption coefficient of $10^{-18} \cdot n_o \cdot \lambda^2$, and provides electrons to the catalytically active molybdenum disulfide nanoislands which exhibits photocurrent sensitivity even to ambient room light.

4.3 Photocatalysis with Molybdenum Disulfide

The role of our photocatalyst in water splitting is to absorb light and generate electrons for the reduction of hydronium. Catalysts appropriate for water splitting should have an electronic band gap suitable for water reduction and oxidation. For photocatalysis, the band gap should be suitable for absorption of many wavelengths in the range of AM 1.5 light source. This presents the paradox that an ideal material should have a wide enough band gap to bridge the overall water splitting redox potentials, but a narrow enough band gap to absorb the maximum

amount of light. Molybdenum disulfide strikes a good balance, as shown in the review by Akihiko Kudo in 2009, even before the knowledge of monolayer properties of the materials. In the review, cadmium selenide and silicon were the only other systems considered with a narrower band gap than MoS_2, but their valence band did not reach the oxidation potential of water.[34] Molybdenum disulfide has conduction band minimum of -0.12 eV and 0.25 eV for monolayer and bulk systems respectively, positioning the conduction band of monolayer material slightly higher than the reduction potential of water. However, we decide to look at the material only for the case of water reduction, because the Volmer - Tafel mechanisms have a high efficiency on sulfur surfaces. It is well established, from the use of MoS_2 in hydrodesulfurization (HDS) reactions, that hydrogen adsorbs at sulfur sites. However, in the case of the HDS catalysis, the sulfur is removed as H_2S gas. But, the selectivity that the system shows is specifically advantageous for the cathode reaction in water splitting, where, for the HER which we are investigating, electrons are collected by hydronium species adsorbed at the sulfur site and evolve from the electrode as elemental hydrogen gas. Previous work studying the activity of molybdenum disulfide in scanning tunneling microscopy has shown direct, experimental evidence of sulfur activity, enhanced at the edge sites of the crystallites.[30, 35]

4.4 Methods

Photocathodes of molybdenum disulfide are prepared by chemical vapor deposition growth using bubbler style and powder based methods described in Chapter 3. The samples are optically characterized by Raman and photoluminescence measurements. Due to the lack of optical contrast of the materials on the 1.82 nm oxide/ p-silicon substrate, scanning electron microscopy (SEM) and atomic force microscopy (AFM) are used to identify the microstructures present after growth. Atomic force microscopy shown in Figure 3.9 of the CVD grown sample shows nanometer and micron-scale clusters of triangular islands.

The samples, now deposited with MoS_2, are diced to fit inside the PEC cell. Contact is made to the back of the sample using a Kapton shielded copper wire, embedded in eutectic indium gallium, deposited on the etched silicon back of the photocathode. Kapton film is further used to protect the sample edges from oxidation, encapsulate the eutectic and mask inactive areas on the sample in order to obtain a more accurate photocurrent density value. The electrolyte, 0.5 M H_2SO_4, is used as described in Chapter 2. Molybdenum disulfide is impervious to degradation by the electrolyte solution under the experimental conditions.

The low built-in potential between the MoS_2 and p-silicon seen in the Kelvin Probe Force Microscopy measurements points to the fact that our TMD, as grown, is natively n-type as previously reported in the literature.[2] As a result of the low open circuit potential, significant drop-off in current will not occur until enough bias is applied to the cathode to create an inversion layer in the space charge region.

This was shown experimentally in standard broad area illumination measurements using a potentiostat.

In order to engineer a surface with built-in potential, we evaporated 50 nm titanium collectors onto the identical RTO SiO_2/ p-Si substrate. As a comparison, collectors of the same size were prepared as 20 nm of platinum on a 30 nm titanium adhesion layer.

4.5 Results and Discussion

First, we consider polarization curves of the molybdenum disulfide on RTO/ p-silicon to determine the onset and photocurrent density generated. For a bias of -1.25 V vs. RHE, the electrode demonstrates a photocurrent density of 16.4 mA/cm^3. Photovoltage obtained experimentally, by modulating light on and off during the linear voltage sweep, gives a value for the onset of the system at 60 mV vs. RHE. The Tafel slope for the MoS_2 sample was 29 mV/ decade. For the silicon electrode before growth, the Tafel slope was 32 mV/ decade seen in Figure 4.1 d. Of interest is the Tafel slope for the MoS_2, which I in the range where the Volmer-Tafel mechanism dominates.[36] The Mott Shottky plot is taken in cell under the previously stated conditions without illumination. The curve generated from the measurement is shown in Figure 4.1 c. The p-type behavior of the system is evident from the negative slope in the linear portion of the curve. The flat-band voltage is determined from the intersection of the linear regime of the curve with the potential axis. For this system, the flat band potential, based on the Mott

Shottky plot, is -400 mV. Finally, the charge carrier density, N_A, was calculated from the Mott-Shottky flat band potential and the potential at inverse capacitance, using Equation 2.8, and is 1.33 x 10^{26} cm^{-3}.

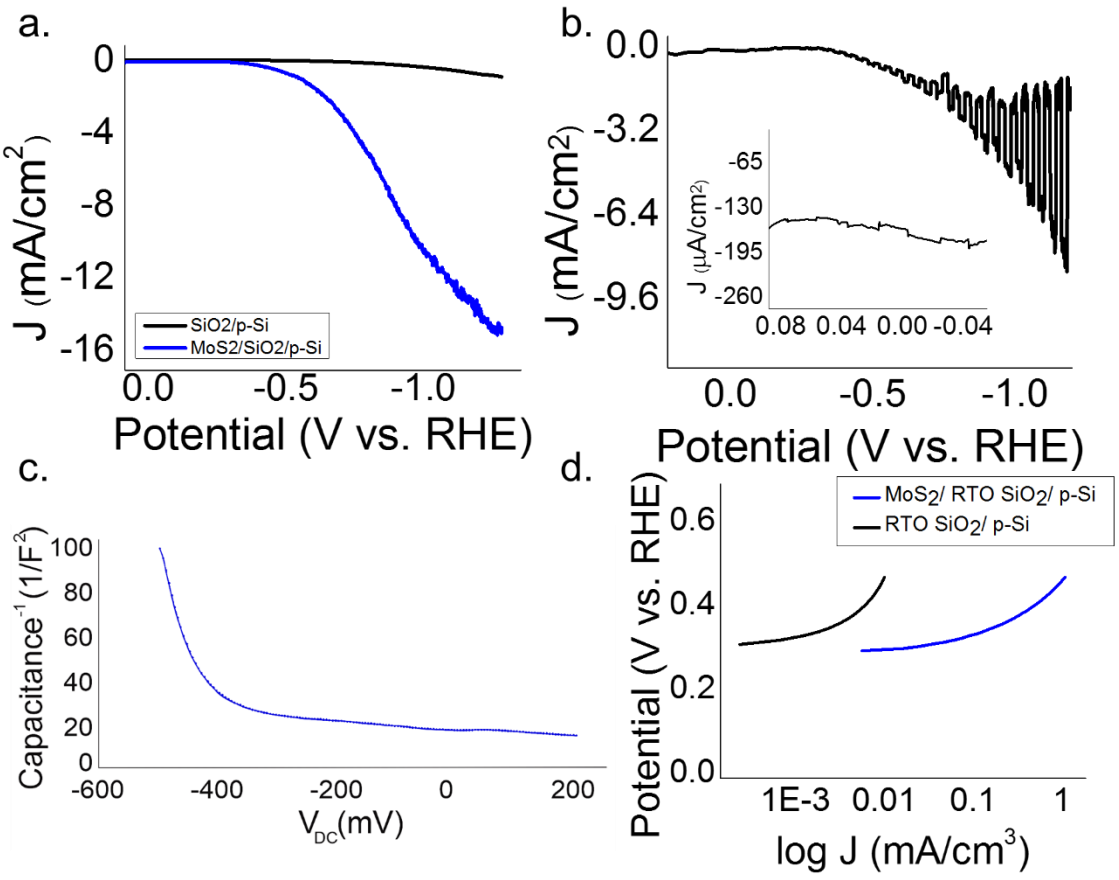

Figure 4.1: a. Mott Shottky plot shows the inverse capacitance as a function of DC bias for the MoS_2 on RTO SiO_2/ p-silicon system. b. The Tafel plot shows an exchange current density favoring cathodic conditions.

In the exploration of MoS_2 deposition, the first stage of our work explored CVD grown MoS_2 on the RTO SiO_2/ p-Si. The potential at which our photocurrent turned on, or rather the photovoltage results led us to consider the built-in potential of our

MoS_2 and p-silicon system. Because, with materials systems having lo difference in work function (Φ_{Δ}), it can be expected that the photovoltage will be poor. This explanation was given credence by Kelvin probe measurements which define the difference in potential between the two materials to be between 0.075 and 0.150 V. This potential small difference indicates the low Φ_{Δ} and allows us to define the MoS_2 grown in the CVD method to be n-type in character, as reported in the literature.[2] The difference in work function between MoS_2 and our p type silicon is 0.4 eV.

As a result of the low built-in potential, and the thin nature of the MoS_2 nanoislands the voltage drop is unable to occur in the MoS_2, and therefore a significant drop off in current cannot occur until so much bias is applied that the surface is inverted, at a large negative potential seen by the photovoltage and flat band potential in Figure 4.1 b., c.

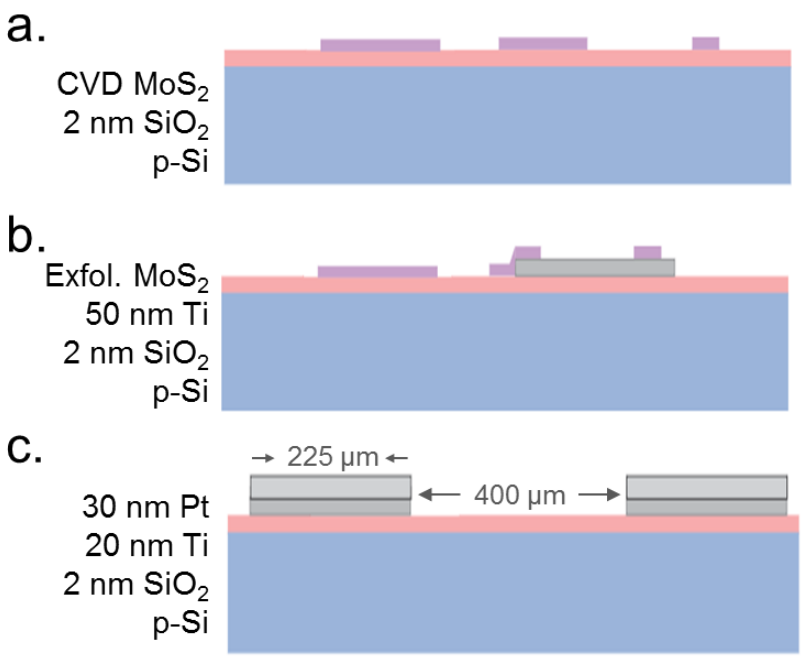

Figure 4.2: Semiconducting photocathodes investigated are; a. CVD MoS_2 as grown on 1.82 nm SiO_2 on p-silicon, b. exfoliated MoS_2 on 50 nm thick, 225 µm titanium metal collectors, and c. 30 nm of platinum with a 20 nm titanium adhesion layer deposited in the same collector pattern as was used in b.

In an effort to gain a better understanding of the effect of the built-in potential on catalytic MoS_2 applications, another system was engineered, shown in Figure 4.2 b., using titanium collectors with a well-defined work function, smaller than that of our TMD material. The smaller work function results in a greater built-in potential between the titanium metal and p-silicon, not seen between our CVD grown MoS2 and p-Si as described in Figure 4.3. The metal in the system has another important and established role, to reduce photo-generated carrier recombination. An analogous pattern was made, shown in Figure 4.2 c., using platinum, a non-photoactive, noble metal catalyst. The platinum sample allows us to evaluate, within this new system, the effect of the molybdenum disulfide.

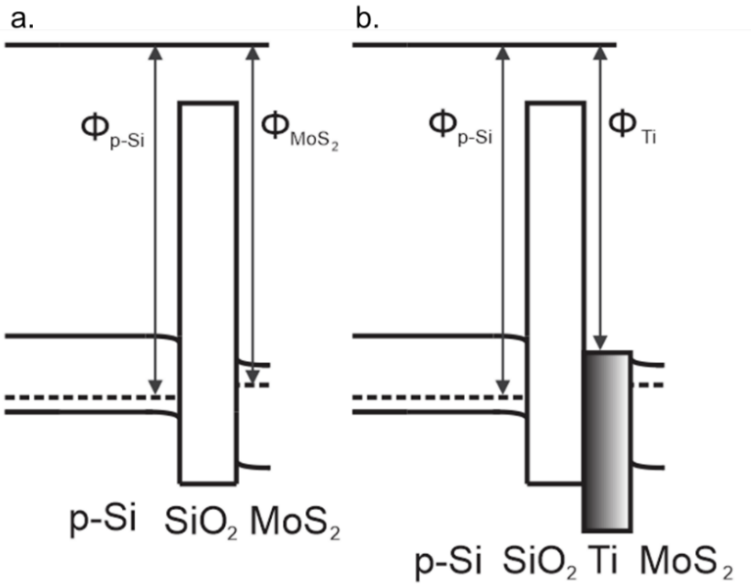

Figure 4.3: The schematic shows the difference in work function between a. the MoS_2 and b. titanium as compared to that of p-silicon at left in both diagrams.

The growth methods utilized in preparation of molybdenum disulfide samples presented limitations in dealing with the metalized substrates in the temperature stability of the thin films. Mechanical exfoliation onto the titanium decorated substrate was employed as a facile proof of concept for this system. The results of the polarization curves, shown in Figure 4.5, demonstrate that the presence of catalytically inert titanium improves the photovoltage by 323 mV, shifting the turn on potential to 0.43 V vs RHE

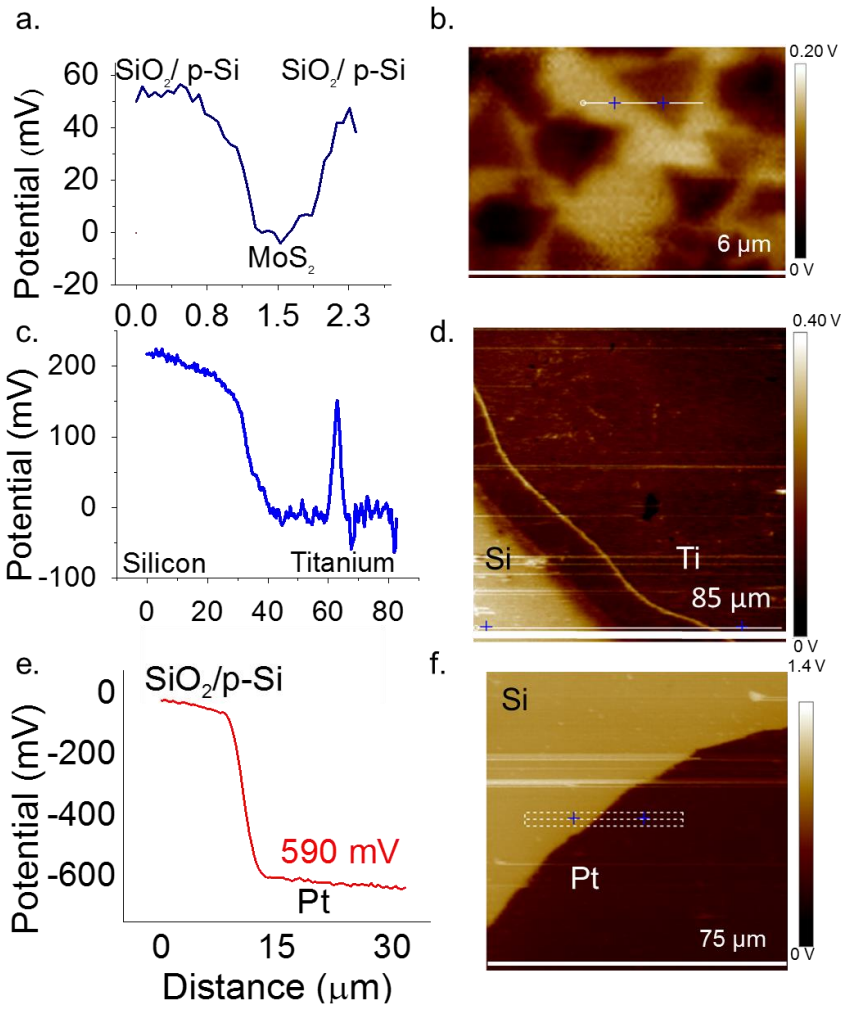

Figure 4.4: a. KFPM image and b. linescan of molybdenum disulfide islands grown on 1.82 nm SiO_2/ p-silicon. c., d. KPFM of molybdenum disulfide deposited on titanium collectors on the 1.82 nm SiO_2/ p-silicon substrate e., f. Surface potential difference image and linescan of platinum metal deposited as collectors on the RTO thin oxide/ p-silicon surface.

To verify the measurements of photovoltage arise from differences ins surface potential, we did Kelvin Probe Force Microscopy (KPFM) on the systems decorated with metal collectors. Considering the line scans in the measurements in Figure 4.4 c.-d., e.-f., the surface potential differences for both of the metal collector systems are greater by an order of magnitude compared to the MoS_2-p-

silicon case. Stability measurements of the system are shown in Figure 4.5 d. Chronoamperometry, measured over a span of 2 hours, under illumination at constant bias of -1 V vs. RHE, shows a stable photocurrent at -15 mA/cm^3.The metrics are summarized in Figure 4.6.

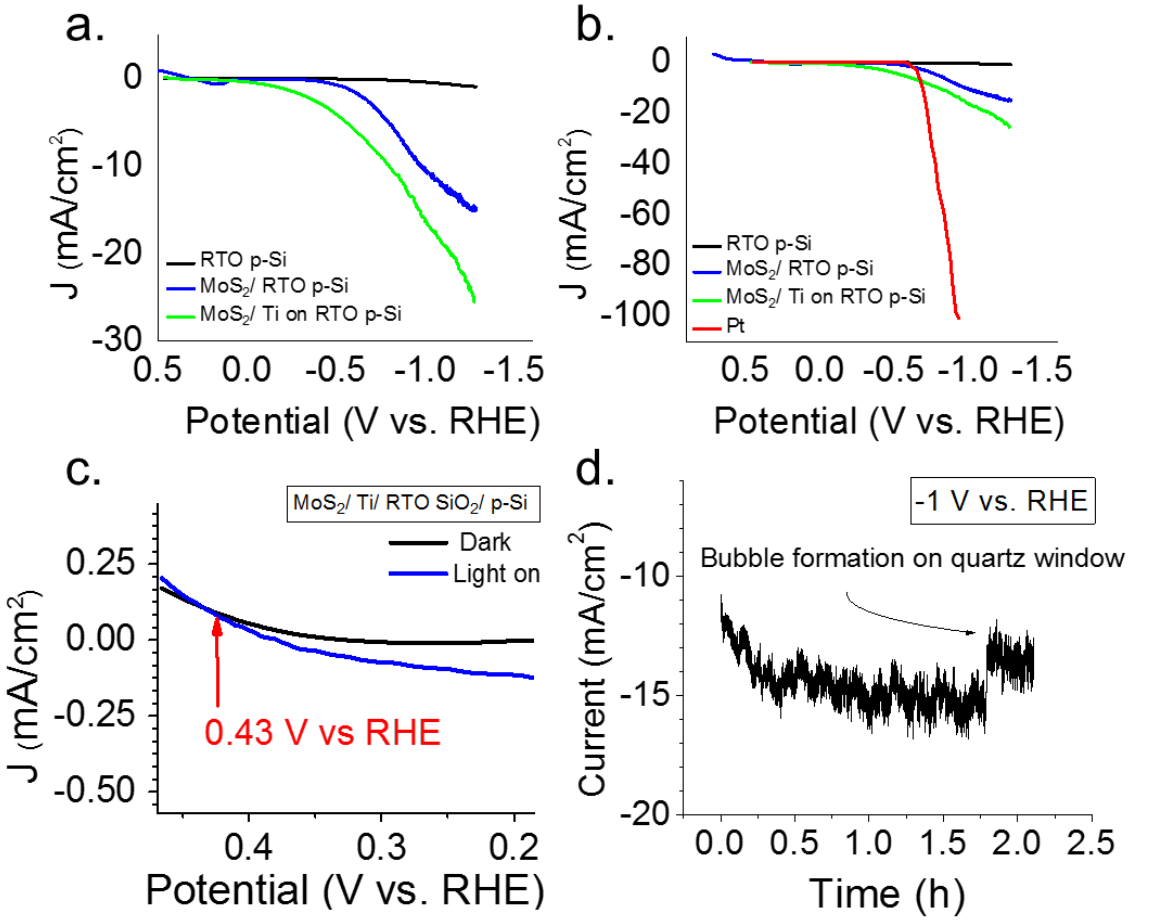

Figure 4.5: a. Polarization (LSV) measurements of the fabricated systems showing the surface patterned with titanium metal to have a more positive photovoltage and higher photocurrent density (green), than the case of molybdenum disulfide directly on the 1.82 nm SiO_2/ p-Si (blue) with the substrate itself (black) not active on the scale of the measured photocurrents. b. The case of platinum requires a greater overpotential, but is more efficient, yielding photocurrent larger than the best measurements taken of the MoS_2 based systems by a factor of four. c. Photovoltage shown as the light-on measurement exceeds the dark current at 0.43 V vs. RHE d. Chronoamperometry over 100 minutes shows a steady photocurrent of -15 mA/cm^3 at -1 V vs. RHE.

Materials System	J (mA/cm^2) - 1.0 V vs. RHE	Photovoltage (V vs. RHE)	Built In Potential MoS_2- Substrate (V)
SiO_2/ p-Si	-3.8	-.12	--
CVD MoS_2/ SiO_2/ p-Si	-10.6	0.06	0.075-0.150
MoS_2/ native TiO_2/ Ti/ SiO_2/ p-Si	-16.4	0.43	0.250
Pt/ native TiO_2/ Ti/ SiO_2/ p-Si	-100.8	-0.57	0.590

Figure 4.6: Summary of materials systems photocatalytic behavior.

Finally, in order to add enhanced understanding to the previous knowledge of collector-based systems, conducted on the same 1.82 nm RTO/ p-silicon surface, we modified the setup of the cell for scanning photocurrent microscopy.[31] With scanning photocurrent microscopy, we were able to collect two dimensionally resolved photocurrent data on the MoS_2/ Ti/ p-silicon surface shown in Figure 4.2b. The photocurrent decay between a collector and a metal strip at the edge of the pillbox, spaced 1.5 mm apart from one another, is shown in Figure 4.7 for a range of potentials. SPCM conducted for neighboring collectors, only 400 µm apart from one another, showed an incomplete decay. The behavior of the photocurrent at the pillbox edge (right in Figure 4.7) shows less responsivity than at the edge of the titanium collector (left in Figure 4.7). This difference indicated that the geometry employed in the collector design is superior to that of the titanium strip, the collector allowing a balance of light absorption in the silicon and the Φ_Δ created by the titanium. More interesting than geometry is the long-range drop off in the current. A long decay range has the implication of hydrogen adsorbing and degassing as H_2 far from the site of the collectors as discussed in the Nature Materials paper by

A. Alec Talin.[31] The most negative potential recorded was 215 mV vs RHE, as measurements beyond this were impeded by aberrations due to hydrogen gas bubble formation on the surface of the electrode, diffracting the laser. The line scans in Figure 4.7 show that the photocurrent is highest at the site where the built-in potential is engineered, in the region of the sample where the collectors are deposited. At the edge of the collector there is an even greater photocurrent due to the exposure of the RTO/ p-silicon surface, allowing it to act as an efficient absorber. The range of the enhanced photocurrent is 250 mV vs. RHE seen in Fi

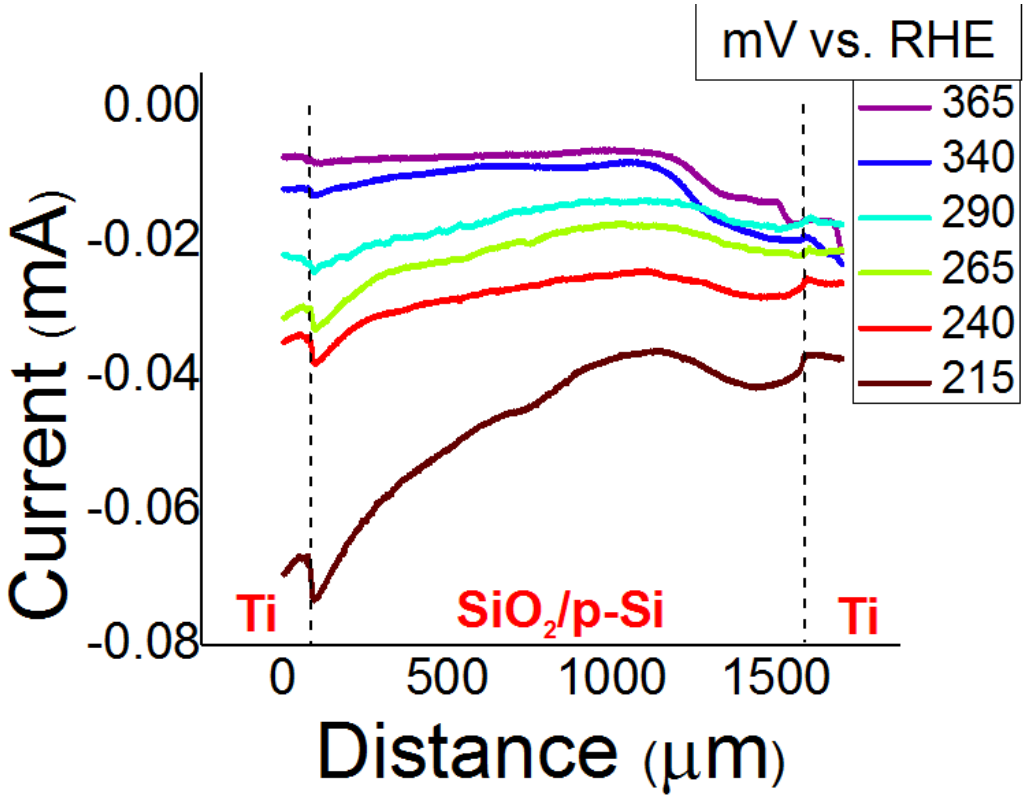

Figure 4.7: Scanning photocurrent microscopy done on the MoS_2 decorated surface shows the photocurrent decay distance from one collector, across the p-silicon surface to the to the nearest neighbor collector.

4.6 Conclusion

We show the optimization of a HER photocathode designed with naturally occurring and abundant materials through surface potential engineering of the heterogeneous semiconductor electrode. The photocatalytic activity of molybdenum disulfide is utilized here, as monolayer CVD grown materials showing the direct band gap transition, show sensitive photocurrent response to illumination. SPCM measurements indicate the electrode with deposited MoS_2 shows photocurrent enhancement at biases positive of 0 vs RHE beyond the length-scale of collector separation distances of 400 μm, indicating the entire active surface of the sample has a shifted photovoltage.

Chapter 5. Physical Transfer of Two Dimensional Materials onto a Variety of Substrates

5.1 Introduction

The photoelectrochemical work clearly showed engineering the substrate is a tool to drive highly photoactive catalysts to function in a more efficient way. It was demonstrated by the improved performance of exfoliated MoS_2 on a metal patterned surface that there is a need for CVD materials to be transferred to other substrates in order to realize TMD applications unfettered by the synthesis conditions. Additionally, transfer of two dimensional materials is especially beneficial for increasing the sustainability of the semiconductor processing and reducing operating costs for university laboratories which use high quality silicon and sapphire as substrate materials. While physical transfer has been carried out on two dimensional materials since the years leading up to the award of the Nobel Prize for graphene, physical transfer of CVD grown two dimensional materials from a range of substrates is still in its infancy.

Several different types of polymers have been employed in the literature to pick up flakes of CVD grown TMD materials.[37] We employ a polymer common in cleanrooms first, and secondly, an inexpensive silicone gel. The methods are evaluated on optical images of microstructures after deposition onto a target substrate and photoluminescence spectra.

5.2 Sonication Based Transfer Technique

Whole sample transfer, over an inch in scale, was achieved through a sonication-assisted process. The vehicle in the transfer were resist acrylates, specifically MMA (8.5) MAA EL 9 (Methyl methacrylate methacrylic acid ethyl lactate) or 950-PMMA A 4. The resists are procured commercially in the form of a copolymer solution. After samples are optically characterized, they are spun coat with the transfer media. The spin coating ensures a uniform and complete coverage. Then, the transfer media is drop-cast over the sample in its' container. The volume of drop cast resist changes the thickness of the cured films. For the purposes of strain measurements, the volume used is 7 mL, this yields films on the order of 180 μm in thickness. In order to harden the acrylic resists, the samples were cured in a kitchen style oven, in air, at a temperature of 65 °C. Curing of the methyl methacrylate occurs via free radical initiation. The elevated temperature assists in free radical initiation, yielding a polymerized, transparent thermoplastic.

For the purposes of transfer to a second substrate the degree of polymerization desired is minimal. In the context of using the resist as a substrate for opto-mechanical strain measurements, the ideal substrate will be flexible while maintaining its' structural integrity, which means that polymerization within the appropriate polymer should be optimized such that it does not become brittle.

Another component to selection of the materials to be used in the preparation of polymer substrates is the glass transition temperature (T_g). The T_g of PMMA and

MMA are well above room temperature, around 100 °C, which means they will behave viscoelastically but maintain their form.

These processes are executed, by design, at temperatures well below what is normally prescribed in other transfer techniques and in semiconductor processing.[38] Due to the volume of drop casted resist it is important to cure the transfer media uniformly. Even heating is accomplished at 65 °C in air in an insulated oven rather than a hotplate for a duration of five hours. Elevated temperatures, above 150 °C are reported to cause irreversible damage the thermoplastic polymer. Additionally, residues left behind by PMMA and MMA resists on graphene have been shown to increase with an increased bake temperature.[39] This high temperature degradation of the polymer will result in deposition of residue, which is insoluble in organic solvents compatible with our transition metal dichalcogenides. The oven setup allows even curing and supports the mechanism for acrylic polymer curing, which is assisted by water vapor present in air.

We observe etching in some of the TMD materials, aggressively at the grain boundaries. This problem is specific to tungsten disulfide and tungsten diselenide. For these tungsten dichalcogenide species, which are more sensitive to degradation under ambient conditions, the spin coating of resist is done with degassed resist solutions in a nitrogen-purged glove box.

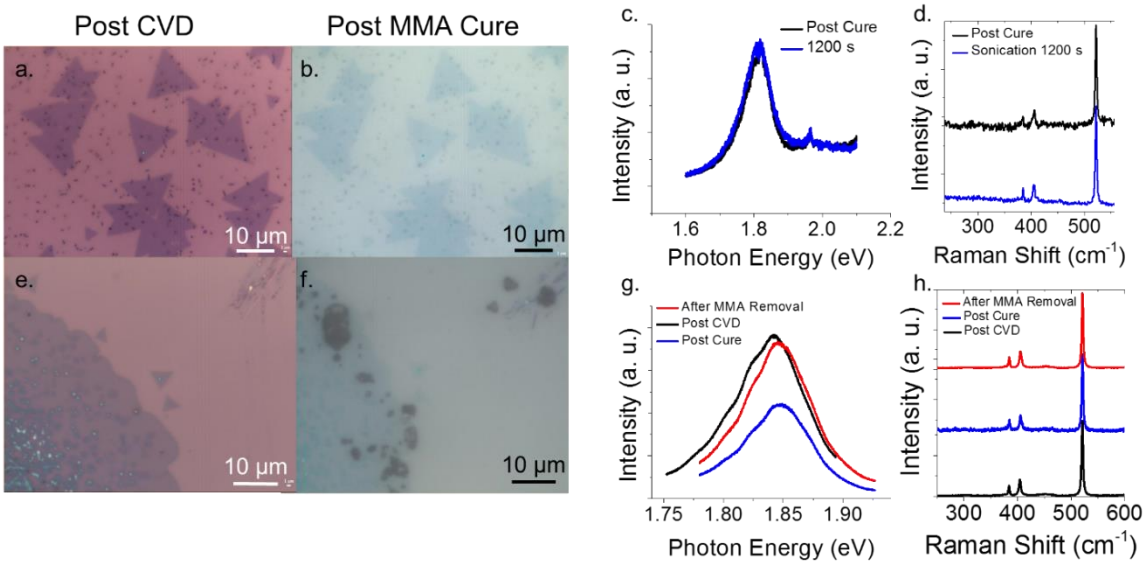

Figure 5.1: Monolayer molybdenum disulfide grown by CVD methods shown in a. is coated with methyl methacrylate b. Photoluminescence and Raman spectroscopy c., d. show that there is no decrease in photoluminescence with a sonication time of 20 minutes. After this length of time TMD material began to separate and was no longer able to be analyzed on the silicon substrate. Another molybdenum disulfide sample e. was coated in the previously written way with methyl methacrylate f. Photoluminescence spectroscopy revealed that the intensity of the PL was decreased by the interference of the methyl methacrylate layer (blue). But, upon removal the intensity increased back to its' previous level and was blue shifted indicating that a built-in tension was released in the process of adhesion and release of the resist.

The substrates, fully encapsulated by MMA and in contact with the glass petri curing dish, are sonicated in deionized water for 28 minutes, such that the chalcogenide surface is not exposed water. Photoluminescence measurements of the sample after growth compared to those done after curing, sonication and dissolution of the resist show no decrease in intensity. Instead, the photoluminescence intensity remains constant, and the peak is slightly blue-shifted due to relaxation of the built-in strain of the flakes, a result of their growth. Sonication is followed by drying of the sample with pure, nitrogen gas. Once all

water is removed from the surface of the resist coated petri dish, the sample is removed from its container and flash removed using a razor blade and tweezers.

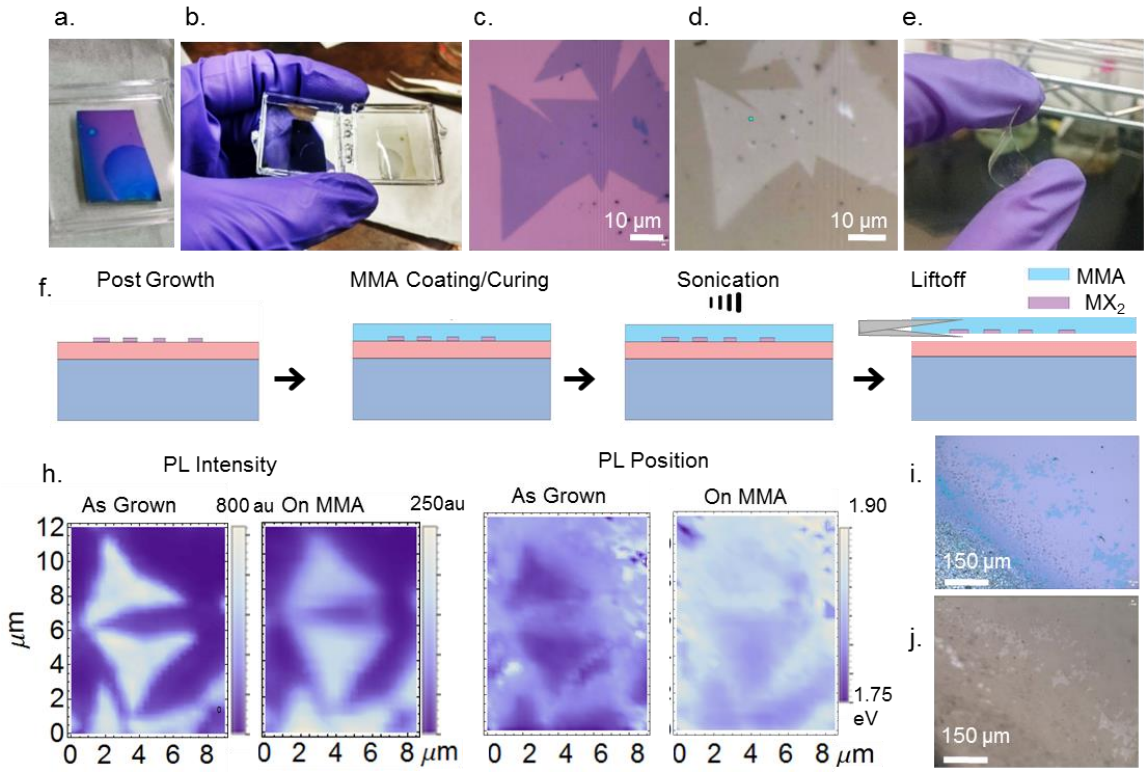

Figure 5.2: a. The sample is shown after CVD growth with visible landmarks of the thick molybdenum oxide "thumbprint". b. The growth is completely transferred onto a polymer film including landmarks via the sonication transfer method. c. Optical images of the MoS_2 island on SiO_2, then d. transferred to the MMA film. e. The transferred material on the MMA film is flexible with monolayer material only discernable under high magnification. f. The transfer method proceeds via spin coating, drop casting, sonication and lift-off from left to right. h. Photoluminescence intensity (leftmost) and position (rightmost) imaging of two islands first on SiO_2 then on MMA. i., j. Low magnification optical images show the scale of the transfer on SiO_2 and MMA respectively.

The process proceeds without contacting the chalcogenide terminated surfaces to any aqueous substance. Water adsorption is known to decrease the efficacy of single-layer transition metal dichalcogenide optical and electronic properties.[40] Using the technique shown in Figure 5.2, a whole sample area may

be transferred from its growth substrate, leaving the growth substrate available for subsequent use. The deposition of the two dimensional materials onto another substrate follows.

At this point the substrate which was used for the growth may be cleaned according to the standard procedures for cleaning substrates from the manufacturer. The process entails with sonication in IPA, IPA/ DI water rinse then in a 30-minute piranha soak. The original growth substrate is completely cleaned at this point and may be used in a new CVD growth as shown in Figure 5.3. Substrate recyclability seen in Figure 5.3 confirms the whole-sample scale of the transfer process.

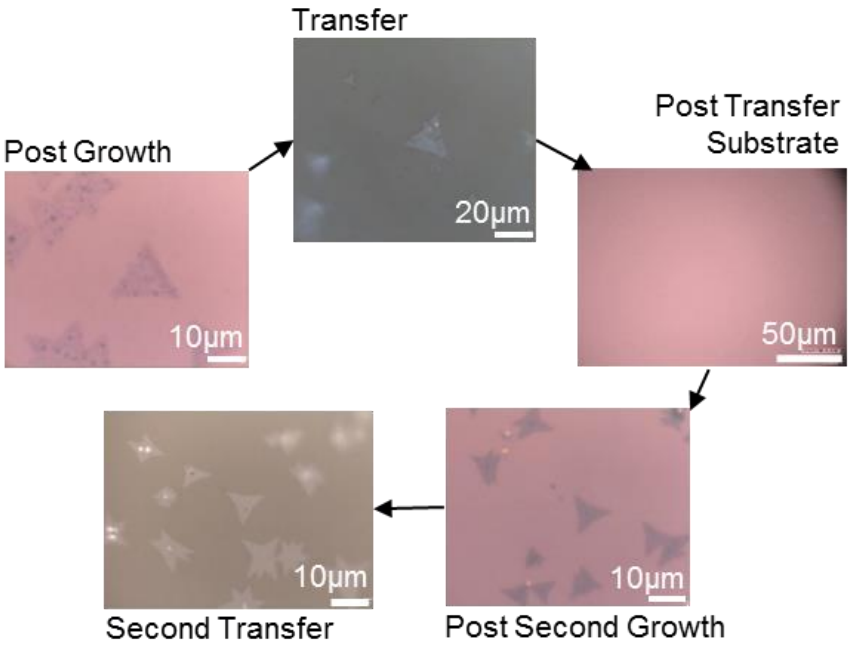

Figure 5.3: Optical images of subsequent chemical vapor deposition growths begin with the post growth case of a TMD on amorphous SiO_2, then show transfer to a MMA substrate. The substrate after and standard cleaning is pictured bare, then after growth. The newly grown islands are transferred onto MMA using the method described in Figure 5.2

The transfer onto a second substrate proceeds after the two dimensional materials have been characterized on their polymer substrates. Figure 5.5 shows two routes to the deposition from the MMA film onto a second substrate. In the first method, shown in Figure 5.5a.-c., acetone vapor refluxing is used to slowly dissolve away the resist. A critical component in achieving good transfer onto the target substrate is for there to be adhesion of the two dimensional materials to the target. Adhesion, in the refluxing approach, is assisted first by placing the inverted film on a clean target substrate and exposing the stack to warm acetone vapor on a level substrate heated to 50 °C shown in Figure 5.4 b. Once the methyl methacrylate appears to have made good contact, as pictured in Figure 5.4 b., the sample is refluxed in acetone at 80 °C for a period of 36 hours above 50 mL of acetone with the setup shown in greater detail in Figure 5.6. Finally, boiling in acetone for 15- 20 minutes after refluxing removes any remaining residue.

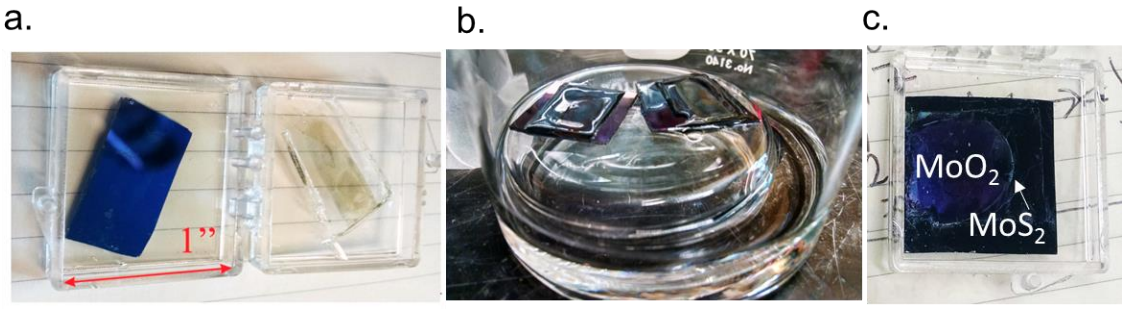

Figure 5.4: The transfer of materials by sonication to a. the methyl methacrylate (MMA) substrate, b. adhesion of the resist films to a new substrate in an acetone vapor bath, and c. deposition of the transferred material, including the characteristic molybdenum oxide strip (labeled at middle left) and the surrounding molybdenum disulfide film.

The second method to deposit onto a target substrate from the methyl methacrylate films is melting of the resist onto a target substrate by heating the film above its' glass transition temperature. The film, now having good contact to the target surface, is subsequently boiled in acetone at 80 °C for three hours to remove the resist. Changing the acetone solution assists in the removal of resist. The results of this method are shown in Figure 5.5 d.-f.

Photoluminescence loss, using the refluxing method (Figure 5.5 b.), from the original PL measured on the sample after CVD growth, is two orders of magnitude in intensity. Annealing the sample at 400 °C for 10 minutes exposed to vaporized elemental sulfur at a flow rate of 5 ft^3/ hr, the photoluminescence was dramatically increased (Figure 5.5 c.). The PL peak is dramatically red-shifted due only in part to relieved built-in strain, and mostly due to sulfur vacancies (Figure 5.5 d.-f.). When healed, the peak blue-shifts to the direct transition energy. The photoluminescence measured under the same power, filter and time conditions for the melted resist case does not show a loss of photoluminescence. However, the peak is broadened from spectra on the original sample. This broadening is statistical evidence of the residue that can be seen in the optical image (Figure 5.5 e., d. respectively.).

The retention of the photoluminescence intensity, discussed earlier for the sonication-based transfer method, seen in Figure 5.1, may seem contradictory to results presented here, for the deposition of the TMDs onto a target substrate shown in Figure 5.5 b. The process temperatures between these methods are

identical, precluding degradation of the resist as the source. The difference between the two dissolutions of acetone is that the method used in Figure 5.5 a.-c. is refluxing and has a duration of 36 hours, while the samples after sonication are boiled in acetone for only three hours. The longer dissolution step exposes sulfur vacancies present to the ketone group in acetone, which over time, perceptively acts as an oxidizing agent in the system.

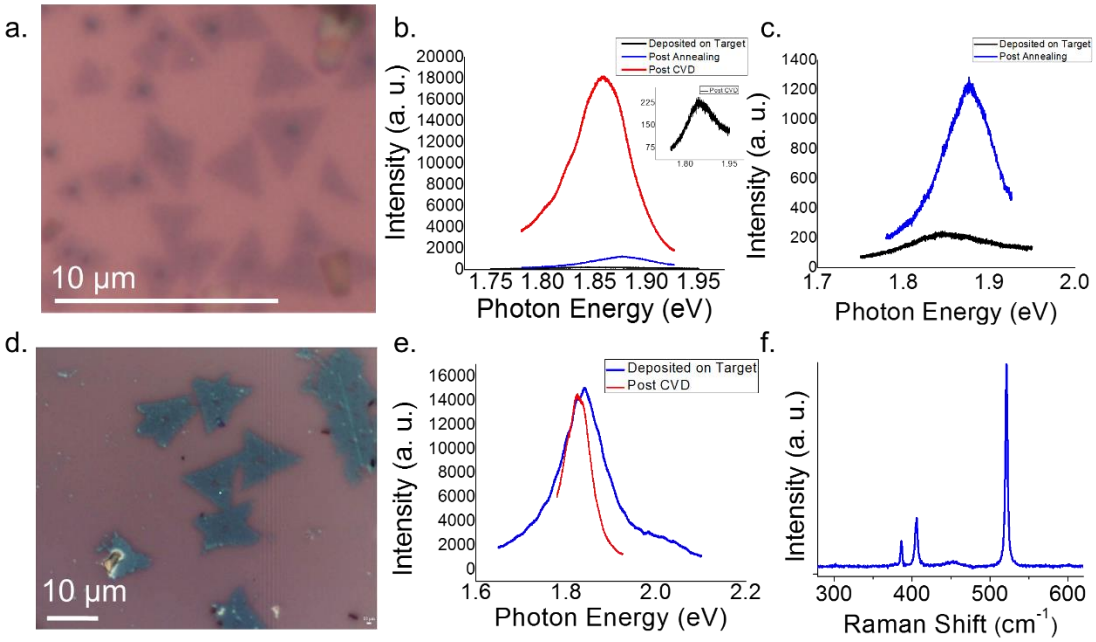

Figure 5.5: Deposition of MoS_2 onto target substrates from the MMA film in a. the refluxing deposition method showing optical microscopy of the islands on SiO_2/ Si substrate, and b. photoluminescence spectra of the sample before transfer (red), after transfer (black) and again after sulfur annealing at 400 °C (red). The panel c. shows nearly an order of magnitude intensity is recovered by sulfur annealing. d. Optical image of melt deposition followed by e. photoluminescence microscopy showing intensity of deposited MoS_2 (blue) within the same order of magnitude as seen originally on the sample (red) and f. Raman spectroscopy signature of monolayer material.

The drawback of this transfer method is in difficulty achieving complete removal of the residues left behind due to incomplete dissolution of MMA or PMMA upon deposition to a second substrate. The issue with their removal is not limited to this

work.[41] The persistence of the resist in small quantities, beyond what is optically discernable, can have a significant effect on contact resistance. For the purposes of transport measurements on two dimensional materials, the residue has even been shown to act as a dopant in graphene field effect transistors (GFETs) and effect characteristic behavior of MoS_2 FETs.[41-43]

However, where deposition onto a second substrate is not required, for example in the case of characterizing the optical properties of the materials during mechanical perturbation of strains, the MMA sonication based transfer method has the clear advantage of providing a flexible substrate and eliminating contact with water during the lift-off process.

5.3 Surface Energy Assisted PDMS Transfer

Polydimethylsiloxane (PDMS) is another vehicle for transfer of CVD grown TMD films which are fabricated on sapphire or silicon dioxide substrates. In this process, adapted from previously published work, the surface energy at the interfaces between PDMS and the growth substrate with water drives the transfer.[44] Surface energy driven transfer has been done before with polystyrene.[37] But, in the method which is presented here there is no curing of or a polymer, and thus no exposure of the subject materials to any solvents.

For the PDMS method the substrate surface is paramount. As the surface energy of the transfer solution, deionized water, remains constant with respect to the PDMS, the relative attraction of water to the subject substrate determines the

transfer. This will limit the application of the PDMS-based technique to any substrate. But, for materials commonly grown on thick amorphous oxides, this process is a good option. The substrates in this process are 300 nm silicon dioxide coated silicon or sapphire substrates with CVD transition metal dichalcogenide or transferred CVD graphene growth. The bare substrate surfaces are highly hydrophilic. Molybdenite (MoS_2) surfaces were reported, from the time of their debut as bulk materials, to by hydrophobic.[37, 40, 45] More recent studies have looked at how the hydrophobicity changes with layer thickness and synthesis temperature. The results demonstrate that monolayer molybdenum disulfide, grown in the temperature range used in this work is hydrophilic, with the contact angle increasing with increased process temperature and layer thickness.[40] Graphene was demonstrated to be wetting-transparent on some surfaces, copper for example, but not on the oxide substrates we are using where the contact angle is determined by the hydrogen bonding as opposed to surface wetting through van der Waals interactions on the metals.[46]

The PDMS gel film is 6.5 mil in thickness with a retention factor given by the manufacturer, GelPak, to be X4. While the weaker retention film, X0, is commonly used for mechanical exfoliation of hexagonal boron nitride and other two dimensional materials, the liftoff of films grown onto the substrate natively by CVD methods requires a stronger interaction. The gel film, placed evenly on the glass slide with a channel for water intercalation as shown in Figure 5.6, is brought into contact with the substrate having the TMD growth via a micropositioning stage.

Between the two unmoving components, a needle injects deionized water at the interface of the siloxane and substrate surface. The capillary action of the water, not limited by too firm a contact between the siloxane and substrate, intercalates between the transition metal dichalcogenide and the amorphous oxide substrate. The surface energy of the water on the siloxane is very high as can be seen in reported contact angle measurements, so the water forces its' way between the growth substrate and TMD material.[47]

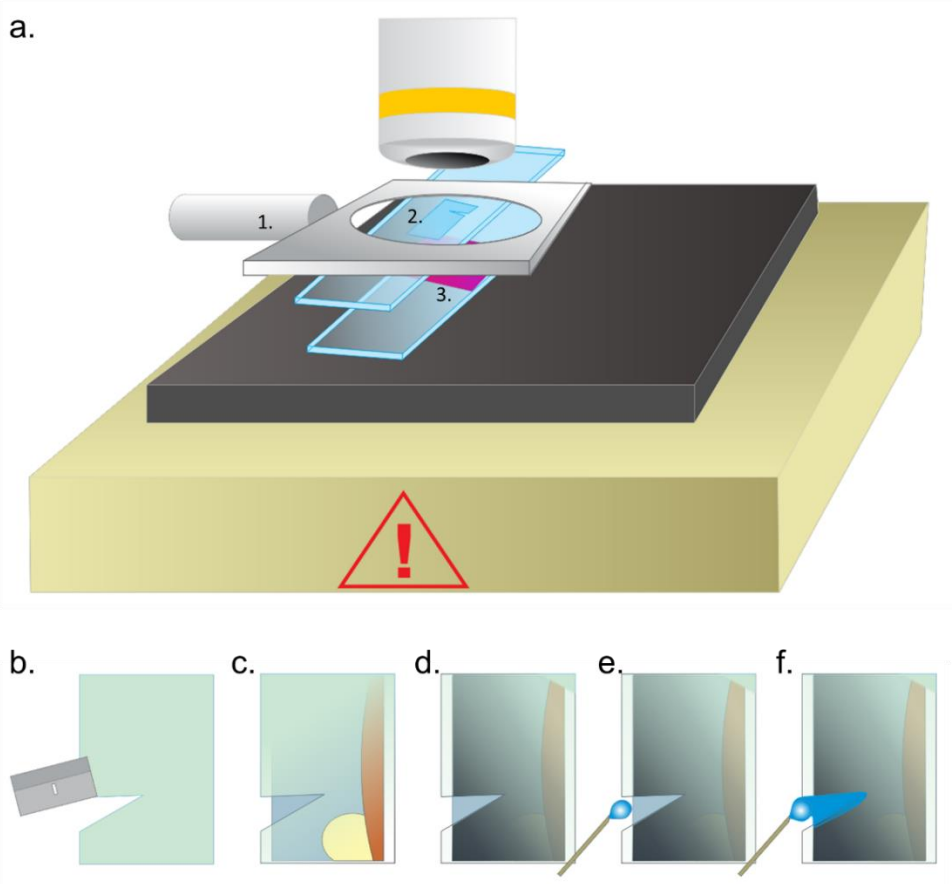

Figure 5.6: a. Setup for PDMS style transfer. 1. Upper stage holds a glass slide with 2. PDMS facing 3. the substrate to be transferred or deposited onto. The stage is heated for deposition onto target substrates. b. An incision in the PDMS allows a channel to assist in water intercalation. c. the stamp and CVD grown substrate are brought into alignment. d. The two surfaces make contact e., f. Water is injected at the channel site where the two materials meet and moves between across the interface.

The water can be seen, through the glass slide between the siloxane film and substrate, in the ToupTek UCMOS1400 camera, as it moves across the sample surface under the PDMS. This is the most crucial step of the transfer and must be allowed to proceed to completion in order to remove all of the TMD material. If the water does not pass a featured area, that area will not be transferred. When the upper stage is retracted, holding the glass slide-PDMS stack inverted over the sample, the TMD microstructures are removed from the original growth substrate and deposited onto the siloxane film. The islands can be seen on the PDMS film in Figure 5.7. The film is immediately dried, thoroughly with argon gas, to prevent adsorption of debris from the environment and to reduce subsequent residue in the second transfer step.

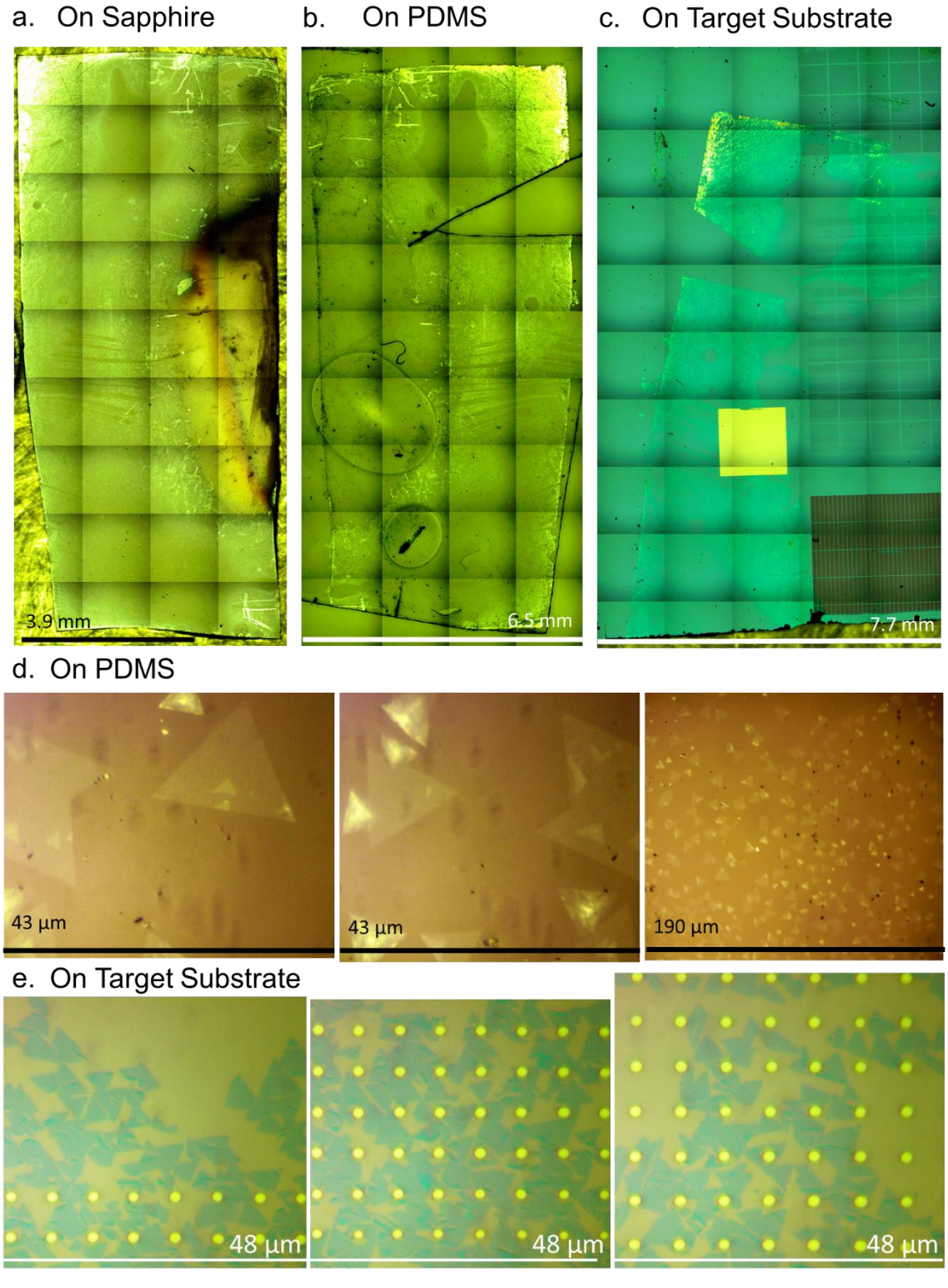
a. On Sapphire
b. On PDMS
c. On Target Substrate
3.9 mm
6.5 mm
7.7 mm
d. On PDMS
43 µm
43 µm
190 µm
e. On Target Substrate
48 µm
48 µm
48 µm

Figure 5.7: a. Stitched optical images of the whole substrate as grown on sapphire is shown followed by b. stitched images of the PDMS stamp after transfer with major areas picked up from the sapphire substrate. The cut seen at top right facilitates capillary action of the water across the sample surface. c. Composite image of the target substrate, SiO_2 patterned with pill boxes of 1 µm holes, shows the areas of CVD growth picked up on the PDMS dropped onto its' surface. d. Images of the MoS_2 on PDMS show that triangular islands were transferred intact to the siloxane film. e. Islands deposited onto a target substrate patterned with holes.

After the monolayer growth has been lifted off of its substrate and picked up by the PDMS, a piranha cleaned substrate is heated to 100 °C and the upper stage containing the inverted siloxane stamp holding the TMD materials is slowly and evenly lowered only to the point of contact, but without creating lateral displacement detrimental to the integrity of the films. The stack of materials, PDMS/ TMD/ target substrate, are kept in contact with the hot plate on for three minutes then separated. Heating during the deposition onto the target substrate reduces the tack of the siloxane film to assist in release of the islands onto the new substrate. The lessening of the tack of the transfer media takes place as entropy increases in an elastomer.[48] When increased above 80 °C, the substrate heating was shown, experimentally, to aid in eliminating deposition of residue, adsorbed on the PDMS film, onto the target substrate.

The hydrophilicity of the substrate surface and the of the transfer species, in our case the transition metal dichalcogenide or graphene, has been established as the crucial component to the mechanism driving this transfer. The molybdenum oxide formed during growth on the surface of the substrate is hydrophobic, it is more strongly bound to the surface of the substrate, not allowing intercalation of water.[45] The molybdenum oxide seen in the first panel in Figure 5.7 a. is left behind on the original growth substrate, not lifted up by the PDMS (Figure 5.7 b.). This is an advantage of the transfer technique, but can also cause partial transfer of TMD films which are grown in close proximity to molybdenum dioxide and oxisulfide crystals.

5.4 Heterostructures Through Transfer

The assembly of heterostructures is an area of increasing interest in fabrication of nanoscale transistors. The sonication based transfer process is used to remove the materials from their original substrate in order to vertically stack different species of CVD grown transition metal dichalcogenides as well as CVD grown graphene on top of one another. Though great advances have been made in directly synthesis of both lateral and vertical heterostructures, precursors and synthesis routes for many heterojunction materials are widely incompatible.

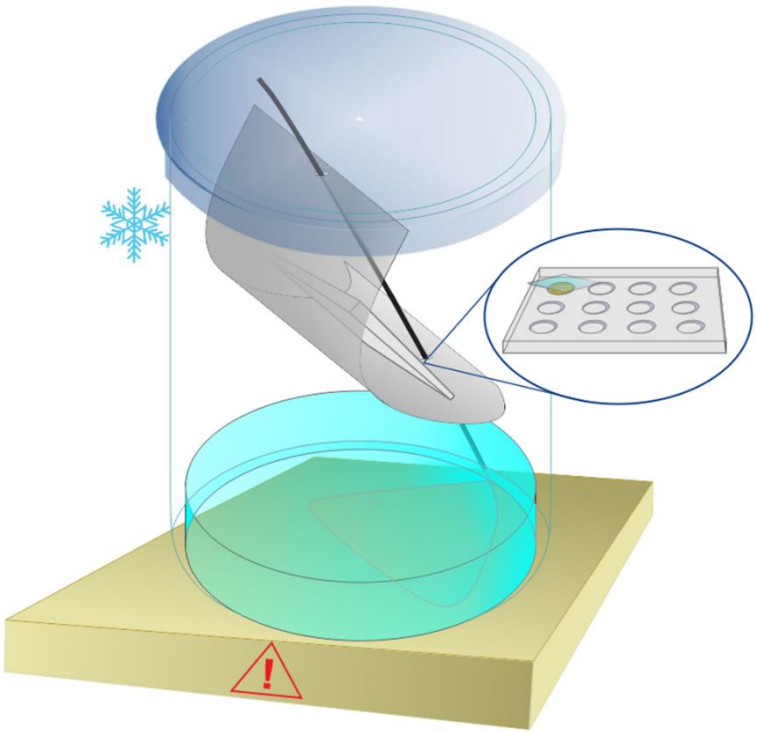

Figure 5.8: The acetone refluxing method of deposition of the graphene/TMD stack from the MMA film onto a TEM grid is shown. The TEM grid is held in place in a recessed groove, machined in an aluminum plate. The plate is tilted to allow the resist to run off.

A vertical heterostructure of MoS_2 on graphene is presented. After CVD growth of the MoS_2 on graphene, samples were transferred to a methyl methacrylate slab using the sonication based transfer technique outlined in Section 5.2. This creates a stack of material as shown in Figure 5.9 where the MoS_2 is in contact with the MMA and the graphene is the top-most layer. Additional Raman and photoluminescence measurements confirm the presence and quality of MoS_2 and graphene on the MMA.

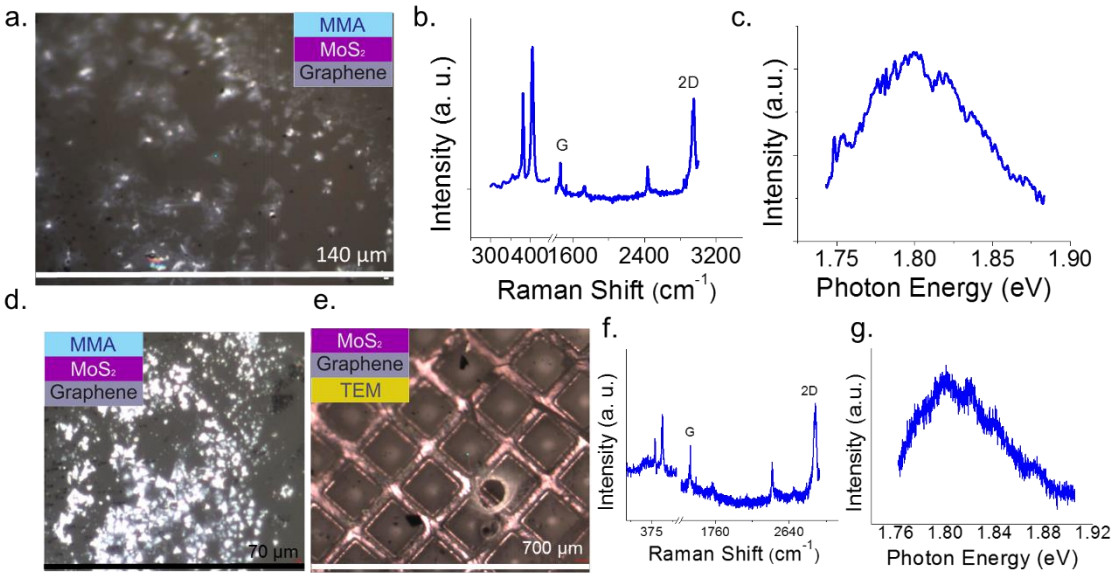

Figure 5.9: Shows graphene transferred to SiO_2/ Si substrate before CVD growth of MoS_2, Raman spectroscopy and PL spectra from the as grown materials system shown in c. and images of the heterostructure as transferred from the growth substrate, then deposited onto a TEM grid

The samples were then transferred to holey carbon mesh TEM grids seen in Figure 5.9. The second transfer step inverts the MMA slab such that the MoS_2 side is in contact with the holey carbon mesh as depicted in Figure 5.8. The resist is then dissolved by refluxing with hot acetone.

Chapter 6. Elastic Tuning of Optical Properties of Transition Metal Dichalcogenides Using Mechanical Strain

6.1 Introduction

Strain engineering of transition metal dichalcogenide (TMD) materials is an area of rapidly increasing interest because it allows substantial modification of the material properties without the need for compositional variations.[49] First principles calculations indicate a pronounced effect on the band gap and Raman modes for materials.[50-52] Prior experimental work has validated this impressively, focusing in particular on tensile strain in single-layer mechanically exfoliated MoS_2[11, 12, 53-57], multi-layer exfoliated MoS_2[22], chemically exfoliated 1T-phase WS_2[58], multilayer CVD grown MoS_2[59], monolayer uniaxial tension in CVD grown WS_2[60], and biaxial strain on monolayer CVD grown MoS_2 and WS_2.[61] Here we report on experiments involving continuous variation of the strain on monolayer, triangular crystallites of chemical vapor deposition (CVD) MoS_2, $MoSe_2$, WS_2, and WSe_2 in the range of ±3.0 %, i.e. including both compressive and tensile strain. The E^1_{2g} in-plane Raman mode softens under lattice expansion, while the A_{1g} out of plane mode remains unchanged. The photoluminescence peaks shift pronouncedly and reversibly during tension and release; the shift direction and magnitudes depend sensitively on the material composition.

The abundance of opto-electronic studies on two dimensional materials are motivated by exciting possibilities to observe, directly from experiments, physics in two dimensions. Transition metal dichalcogenide materials are a class of two-

dimensional materials in which recently observed single layer combinations of transition metals and chalcogenides show vastly different optical properties from their bulk counterparts.[14] With decreasing layers, the d orbitals of the intralayer metal atoms determine the HOMO and LUMO states and become aligned for direct transition, opposed to the indirect energy transition which is due to interlayer hybridization of metal with chalcogenide orbitals seen in bulk materials.[5, 14, 62] Scalability, beyond what is possible using mechanical exfoliation techniques, has been made possible by the materials' weak van der Waals' interactions with surfaces, resulting in non-directional growth on amorphous oxide substrates, as is shown here. For the materials we investigate, the natural occurrence and stability of the transition metal dichalcogenide materials in their layered, bulk morphology carries through to the 2-d morphologies, making it possible to study their properties generally at ambient conditions. Applications of the strain effects are only just emerging, and include, as of recently, electronic sin applicaitons.[63]

Strain effects have been seen in MoS_2 and its analogues in theory and experiment, and conversely, there are reports of determining strain through measurement of Raman modes.[11, 12] Expedited experimental findings have been importantly furthered by the fabrication of exfoliated samples. A number of prior reports of strain-based tuning of the optical response of TMDs utilize exfoliated flakes. However, such flakes often consist of sections of different thicknesses. This is highly advantageous for the study of bilayer and multilayer TMDs. But, it presents complications in the evaluation of the optical response of single layer

material, because the strain distribution in the exfoliated flakes is not necessarily uniform. Other studies have addressed CVD-grown single layer flakes; in this study we augment the available data by including both uniaxial *tension* and *compression*, which provides important validation of the phenomena observed. We probe the effect of tensile and compressive strain on the photoluminescence and Raman modes of the materials MX_2 (M= Mo, W, X= S, Se).

6.2 Methods

Our TMD films, MX_2 (M=Mo, W; X=S, Se), were grown through ambient pressure chemical vapor deposition in a single-zone, quartz, tube furnace at temperatures of 680 °C and 850 °C for molybdenum and tungsten based materials respectively. Our molybdenum-based growth process implements alumina crucibles containing molybdenum trioxide powder in central hot zone and sulfur or selenium powder approximately 10 inches up stream, in a 2 inch quartz tube as discussed in Chapter 3.[2] Tungsten based TMDs were prepared similarly, with S/Se crucibles upstream, but using two substrates facing each other in the center hot zone of the tube furnace. The bottom substrate acted as the tungsten source, when spin-coated with 3 mM of hydrated ammonium meta-tungstate.[64] For both growth processes, furnaces were purged with ultra-high purity N_2 gas, to create an inert environment and to act as a carrier, helping to initiate the TMD formation. The furnaces were ramped to the peak processing temperatures over a period of thirty minutes and held for ten minutes to allow the growth reaction yielding monolayer islands on the

order of 10 µm. Process tubes are cooled to room temperature with continuous nitrogen purging. Our TMD crystallites exhibit the expected photoluminescence and Raman characteristics as shown throughout this manuscript. The excitation wavelength for experiments shown in this chapter is the same as that used for Raman and photoluminescence (PL) spectroscopy throughout this dissertation, a Diode-Pumped Solid State 532 nm laser. The number of layers in the material can readily be deduced from the Raman spectra, the PL intensity and optical micrographs; in addition, we confirm thickness for select crystallites by means of atomic force microscopy (AFM) using an ASYLUM MFP 3D system in non-contact mode as detailed in Chapter 2.

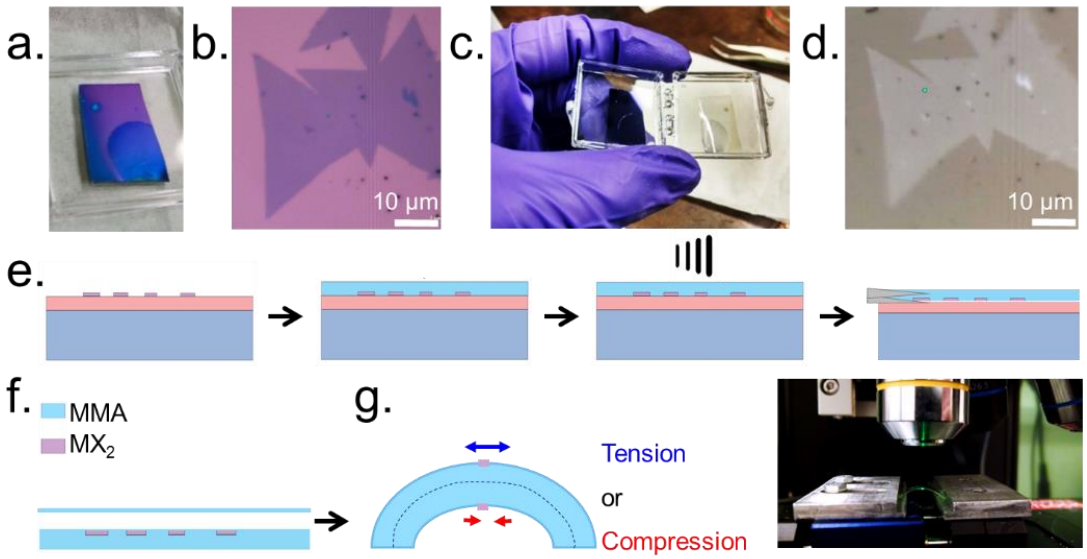

Figure 6.1: a. The whole substrate is shown macroscopically as-grown on a 300 nm SiO_2/Si and b. in optical images of 40 µm coalescing islands. c. The substrate is then shown after transfer with thick oxide as well as thin TMD film wholly transferred to a flexible membrane. An optical image d. shows the same monolayer growth of MoS_2 transferred to methyl methacrylate film. e. The as grown sample is spun with methyl methacrylate, drop cast then cured. The cured substrate is sonicated. The MMA film is lifted from its substrate with TMD materials attached. f. The TMD films on the MMA substrate are encapsulated by spin coating resist polymers. g. The films undergo uniaxial tension or compression at the apex of their curve as illustrated and shown in the photograph of the stage (right).

The TMD films are transferred from the growth substrate and measured directly on the transfer media. The physical transfer process is effective at complete transfer on substrates as large as 3 x 3 cm as shown in Figure 5.2 and again in Figure 6.1. Spin coating to achieve uniform coverage is followed by drop casting of methyl methacrylate (MMA). Drop casting allows the TMD materials to be supported on a thick slab, on the order of 170 μm. The thickness is important to achieve significant strain values during deflection. Curing does not exceed temperatures of 65 °C to retain the optical properties of the pristine material. The substrates, fully encapsulated by MMA, as detailed in Chapter 5, are sonicated in deionized water. The TMD's surface does not see water during any part of the transfer. The chalcogenide terminated TMD's absorb water on their surface very strongly due to hydrogen bonding. The oxidation of the molybdenum disulfide surface has been shown to increase drastically with humidity, a focus of study since the 1950s.[65] This is also an important consideration in transfer of a wider variety of TMD's, as many are unstable in air. The ultrasonic vibrations during sonication of the cured material in the curing vessel allows for subsequent liftoff, of the polymer and the two dimensional film, from the substrate. The effects of sonication, as well as low temperature exposure to MMA were examined and are shown in Section 5.2. Sonication for up to 20 minutes had no negative effect on the photoluminescence of the material, at which point the separation began. Once the films started to detach from the substrate, measurement of the target material on the silicon dioxide surface was no longer possible.

Density Functional Theory (DFT) is used to predict and interpret the effect of mechanical strain on the sample material. Calculations are performed using the spin-polarized version of Density Functional Theory (DFT), implemented in the Vienna ab initio simulation package (VASP 5.3.5) with the *Perdew-Burke-Ernzerhof Generalized Gradient Approximation e*xchange-correlation and the projector augmented wave potentials.[66]

Our computational super-cells include 20 Å of vacuum separating the TMD layers vertically, so as to avoid inter-layer interactions. We sample the Brillouin zone with a Monkhorst-Pack scheme and a (3 x 3 x 1) k-point mesh. For the plane-wave expansion of the electronic wave function, an energy cutoff of 450 eV is used. Geometry of the structures are relaxed until the force on each atom is less than 0.01 eV/Å and the energy convergence criteria of 1×10^{-5} eV are met. Spin-orbit coupling contributions to DFT are included, because of the unique property of transition metals, with empty d-orbitals that often split into two energy levels, as described by ligand field theory. These two levels give rise to a split valence band discussed in Chapter 1. Excitons make use of the valence band. The size of the split-valence band directly correlates to PL intensity.

For each monolayer system, the unit cell is optimized to obtain the lattice parameters corresponding to the lowest total energy. We obtain optimized lattice parameter of MoS_2 3.184 Å, $MoSe_2$ 3.312 Å, WS_2 3.182 Å, and WSe_2 3.317 Å in good agreement with experimental values.[67-70] As we ascertain experimentally that we induce uniaxial strain on the TMD islands, we disallow horizontal relaxation in

calculations on strained film, while allowing vertical a one. The latter relaxation corresponding to a change of the vertical separation between M and X layer. We note that uniaxial strain can be applied along any direction between [100] or [110], i.e., along the M-Γ-M' or K-Γ-K' direction, respectively, and we treat the two extreme cases separately. The orientation of the islands in real space is shown in the image in Figure 6.6a, and its' projection into reciprocal space with strain in Figure 6.6 e., f.

6.3 Results and Discussion

The Raman spectra of as grown MoS_2 show characteristic monolayer Raman active peaks at 382 cm^{-1} and 400 cm^{-1} shifted from the bulk materials' modes and indicative of well-established stiffening of the A_{1g} and softening of the E^1_{2g} phonon modes that occurs with decreased layers of material.[14] Photoluminescence for each material was centered at the known direct gap energy as seen in Figure 6.2.

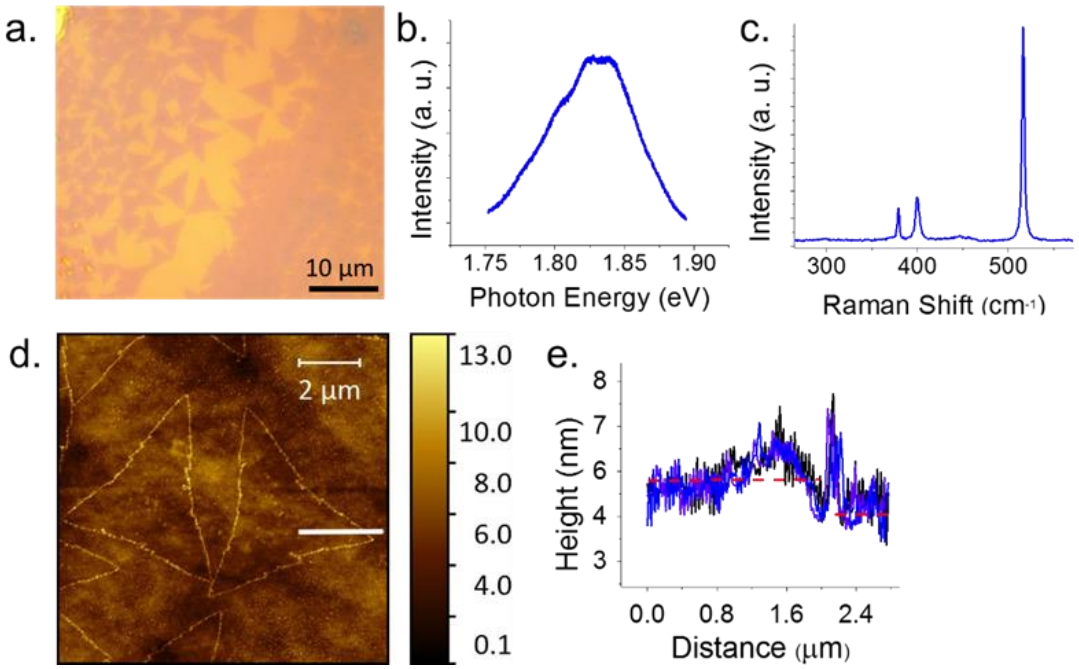

Figure 6.2 Characterization of the materials post growth indicated the requisite height, PL position and Raman shift for monolayer TMD materials. a. The optical image shows molybdenum disulfide islands grown on 300 nm SiO_2/Si substrate. These are the same islands characterized in the photoluminescence mapping shown in Figure 4 of the manuscript, b.-c. Photoluminescence and Raman spectra respectively are evidence of the monolayer nature of the material as grown with a E^1_{2g}- A_{1g} peak difference of 18 cm^{-1} d., e. An averaged line scan of the edge of the triangular crystallites in the AFM image. d. shows characteristic height of 0.85 nm on amorphous SiO_2.

Strain was applied in both tensile and compressive modes by bending of the membranes such that the microstructure of interest is centered at the apex of the bend, shown in Figure 6.1. At the apex, the strain is in uniaxial tension or compression. Precise control of the deflection was allowed through use of a piezoelectric stage. Radii of curvature were determined by the focal points on the surface for each bending iteration and fit to a quadratic curve. The radius of curvature combined with thickness measured by the focal point of the top and

bottom of the membrane is used to determine the applied strain, positive for tension, negative for compression discussed in more detail in Chapter 2.

The TMD materials were bound to the flexible polymeric substrate by a top encapsulation layer of MMA, to ensure conformal bending on the atomically thin microstructures and to prevent lift off. The top layer is of inconsequential thickness relative to the total thickness. Similar to other studies, the thickness of the film combined with the radius of curvature is used to calculate the strain, $\varepsilon=\tau/R_c$.[22] The maximum strain in tension which has been reported experimentally for these materials is 9%[53, 61], well above the maximum tensile elongation of 5% which can occur in viscoelastic acrylic polymers in accordance with methyl methacrylate materials adhering to ASTM D788-11.[71] The Poisson ratio has been measured by others to be 0.95 for monolayer MoS_2 and 0.25 for the bulk case.[53] But, by experimental design, the Poisson ratio of the viscoelastic MMA at the apex of the deflected film constrains deformation in the orthogonal loading direction and forces strictly uniaxial behavior.

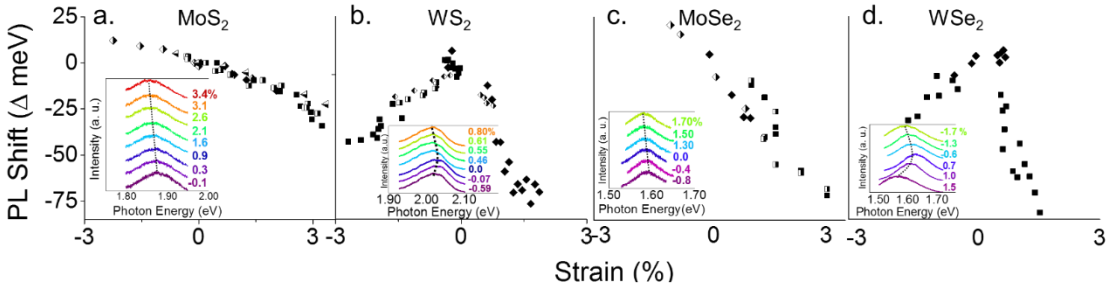

Figure 6.3: a.-d. Photoluminescence shift for MoS_2, WS_2, $MoSe_2$, and WSe_2 respectively with applied strain from -3 to 3 %. Spectra are inset for each material. Multiple datasets are shown with different symbols.

Photoluminescence measurements under strain show that the band gap of the molybdenum disulfide materials decrease in energy with the application of

strain by 10 meV for every percent of applied strain, significantly less than the 45 meV/% strain which has been shown experimentally for monolayer exfoliated MoS_2, reported in Figure 6.3a as a shift from the y intercept of the trend.[11, 50] Spectra are shown, inset in Figure 6.3, for individual samples of each material. The band gap then widens under compressions of up to -3%. The mechanism for the red-shift under tension and blue-shift with compression is a function of the bond angle of X-M-X (M= Mo, W, X=S, Se). This bond angle has been experimentally shown to play a key role in determination the materials' optoelectronic behavior under strain, due to the strong dependence of direct band gap photoluminescence on the interactions of the localized d orbitals of the metal atoms hybridizing with the p orbitals of the chalcogenide species.[51] When the chalcogenide atoms are crowded towards the transition metal atoms, the hybridization of the p and d orbitals is greater. This leads allows a lower energy transition at the Γ point of the Brillouin zone.

The direct optical band gap of tungsten disulfide, at the K point in the Brillouin zone, is shifted in the same direction as is seen in molybdenum disulfide as the material undergoes tensile strain. Under compression, the materials' optical bandgap narrows. The local maxima, or turn-around point, occurs where the material is in its unstrained conformation. A similar mirroring of the effects of tension versus compression is seen in tungsten diselenide. For tungsten diselenide, photoluminescence position narrows upon tension and compression with a high responsivity, differing from the case of tungsten disulfide by its' a

greater sensitivity. The greater responsivity seen in the case of tungsten diselenide is seen for molybdenum diselenide as well. But, the response in compression for the molybdenum diselenide is a blue-shift, the same as the compression response observed in molybdenum disulfide. The decrease in peak position for molybdenum diselenide was 27.5 meV/ % strain averaged between multiple samples shown in Figure 6.3 d., with different symbols representative of different data sets. The increased shift is due to the larger size of the less electronegative selenium atoms, which allows a greater hybridization of the p orbitals with smaller perturbation of the perfect lattice than is necessary in the sulfide TMDs.

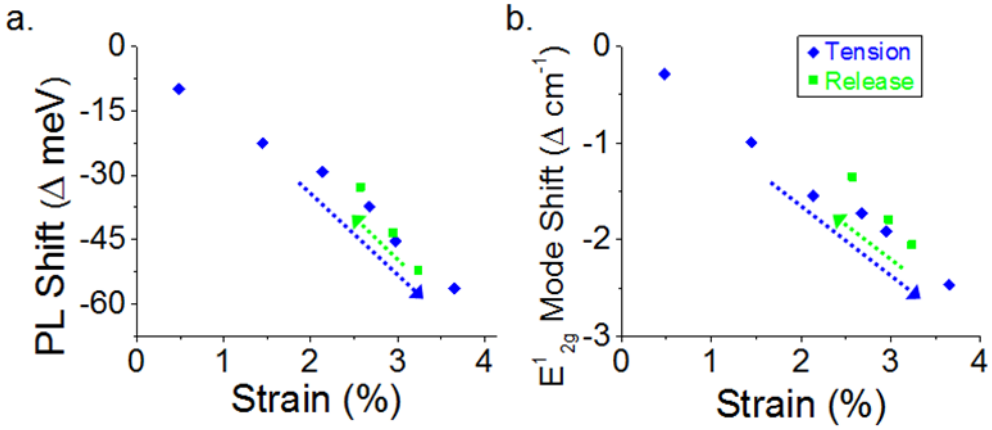

Figure 6.4: The reversibility of the trend for both a. PL and b. Raman spectra is shown here for MoS_2 with application of tension (blue) and release of tension (green).

The shift seen in the PL energy position and Raman response is reversible, allowing the original PL position to be recovered and the recovery is measured incrementally as shown in Figure 6.4 for MoS_2**.** This linear reversibility is evidence that the adhesion between the substrate and TMD material is strong, kept intact by the encapsulation layer. Previous literature supports the reversibility of the trend

upon release for strain of up to 2%.[54] For the data shown, the strain is released from a maximum tension of 3.6%.

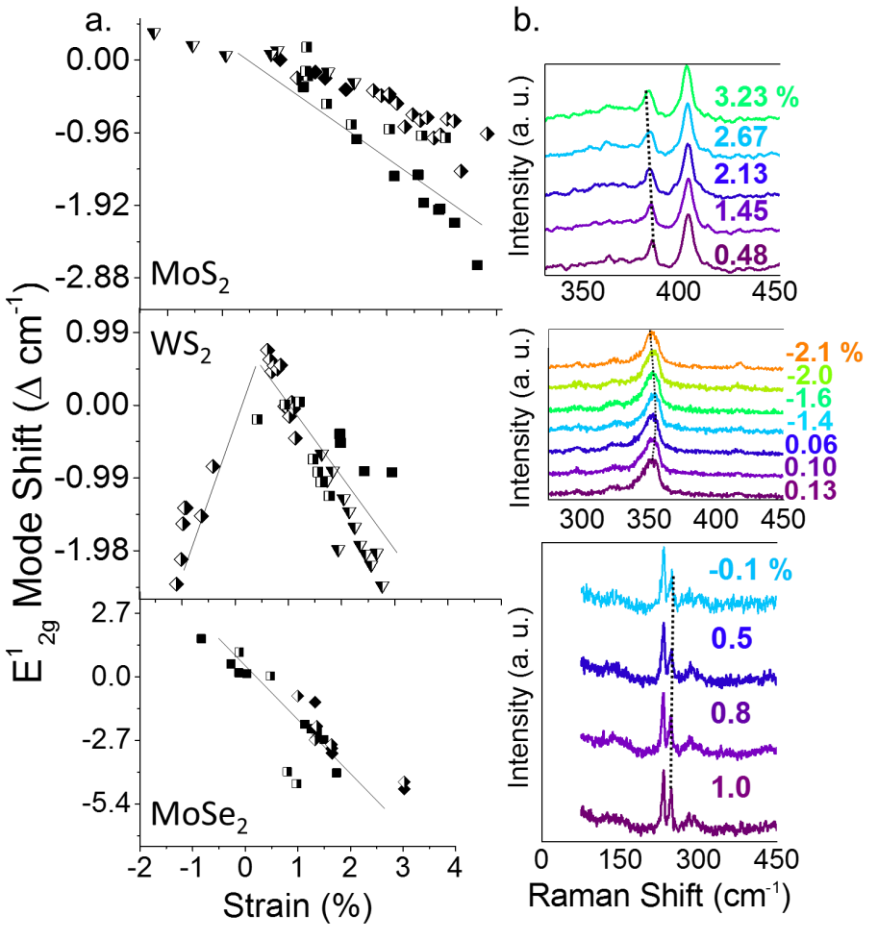

Figure 6.5: a, b. The in-plane Raman modes of MoS_2, WS_2, and $MoSe_2$ are dampened by tension. The tungsten disulfide displays the same response in tension as compresison with a decrease in frequency of 1.72 cm^{-1}/% strain when compressed and 1.50 cm^{-1}/% strain for tension. Samples are represented with different symbols. Spectra of each material as strain is applied are shown at left. Traces are linear fit of combined data sets.

For the Raman active modes of the MX_2 materials studied, we consider the in plane E^1_{2g} mode to be the primary indicator of strain, which we observe experimentally in agreement with previous reports, while the out of plane mode,

A_{1g}, remains at the same frequency, shown in Figure 6.5.[11] The relaxation in frequency occurs in the in-plane Raman modes of MoS_2 and $MoSe_2$ respectively at rates of -0.36, and -3.24 cm^{-1}/% strain respectively. The tungsten disulfide modes behave similarly in compression as in tension with a decrease in both directions of 1.72 and 1.50 cm^{-1}/ % strain respectively. Using the explanation that the X-M-X bond angle is a determining factor in strain-induced orbital interactions, we expect the phonon modes to be most sensitive within the plane, just as it is the localized d states' interaction with chalcogenide orbitals for the case of the photoluminescence.[51] The Raman active modes in tungsten diselenide are the E^1_{2g} and A_{1g} modes which are degenerate at 250 cm^{-1}.[13] Shifts observed in the overlapping peaks are not assigned to a particular mode.

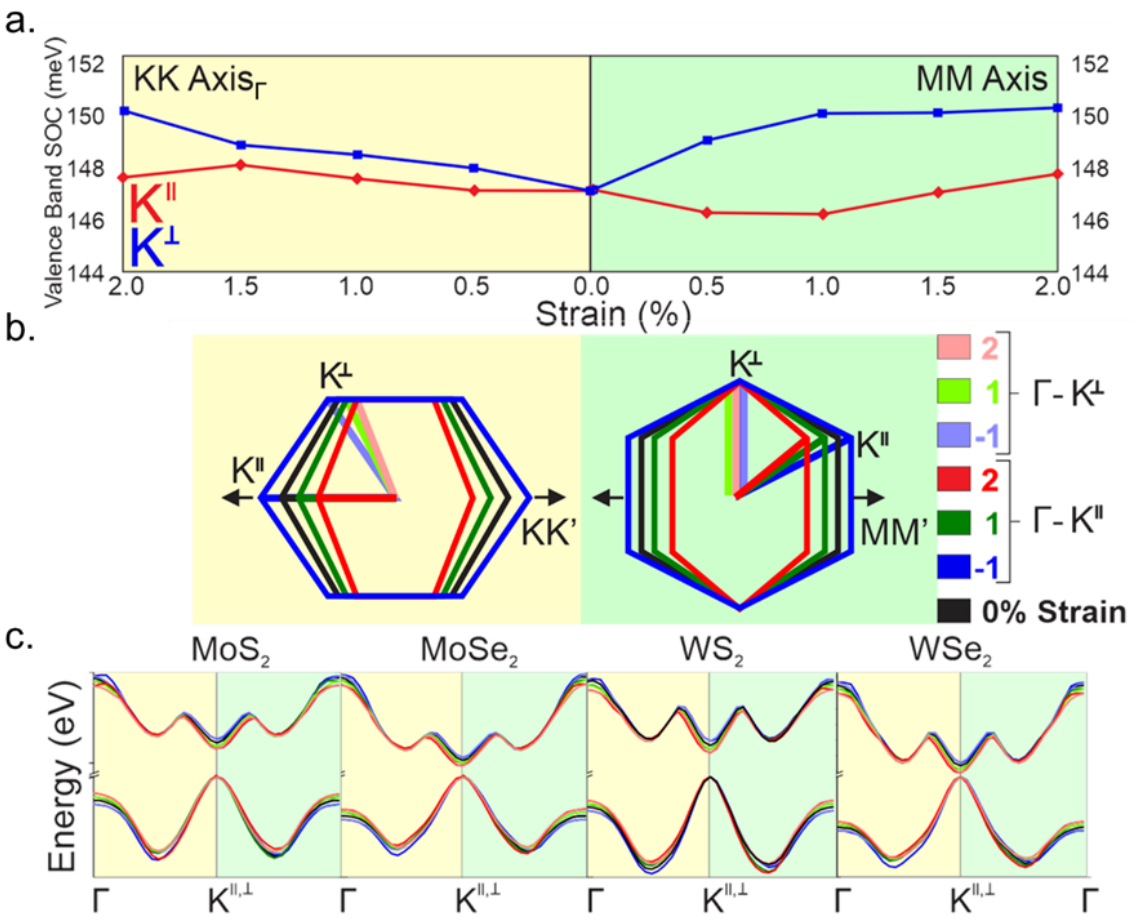

Figure 6.6: a. The difference of the spin splitting in the valence band of MoS_2 is shown for strain along KK'(yellow) and MM (green) from 0-2% c. The band structures along $K^{\perp}$-Γ-K^{II} for the KK' axis deformation in yellow and the MM axis deformation in green. Strain percent are shown according to the color bar in 5b. The $K^{\perp}$-Γ path is shown in pastel.

Density functional theory confirms the trends seen in our optical spectroscopy (Figure 6.6). The DFT images display the band structures of each material, for compression of 1%, and strain up to 2%. These show the narrowing in the bandgap, as strain is increased, and agrees with the already well known phenomena that strain reduces the bandgap such that the direct bandgap eventually becomes an indirect bandgap.[52] The added value in these

measurements, is that they illustrate the path, K-Γ-K, specific to uniaxial strain cases occurring along directions probed in our experimental photoluminescence imaging, with the K^{II} and $K^{\perp}$ of K^{II}-Γ-$K^{\perp}$ defined in Figure 6.6 b.

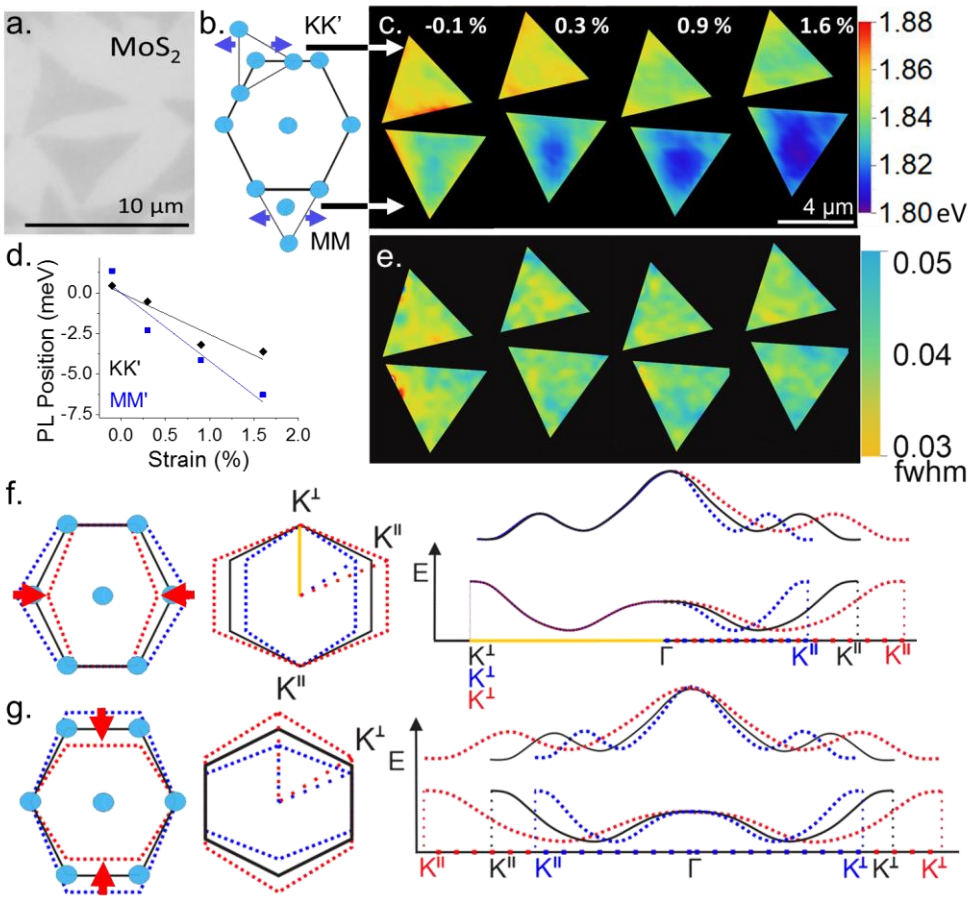

Figure 6.7: a. An optical image of two islands as grown, rotated 30° from one another on the MMA substrate. b. Superimposed primitive cell in reciprocal space over dotted hexagonal real space lattice with high symmetry points of the Brillouin zone labeled. Molybdenum atoms (blue) in the hexagonal lattice structure with superimposed islands oriented as the islands were oriented for the photoluminescence maps (c.) under strains from -0.1 to 1.6%. d. The rate of change in PL position for the top (black) vs. bottom (blue) islands c., e. FWHM of spectra f. Perturbing the lattice in real space along the MM' direction, two of the K points are stationary, the distance Γ-$K^{\perp}$ unchanged, and the Γ-K^{II} distance shortened or lengthened with tension or compression respectively. g. Alternatively, compressive strain (red) of the lattice in real space along K-K' causes expansion in reciprocal space and increases the the distance Γ- K^{II} as well as Γ-$K^{\perp}$ as is seen in the band structure diagram (far left).

In addition to aquiring single spectra of the films under tension and compression, photoluminecence imaging was done. The photoluminescnce images discussed are of two triangluar molybdenum disulfide crystallites grown in close proximity on the CVD substrate, seen in Figure 6.2. The PL maps, shown in Figure 6.7 c., of the islands taken in the same measurement, give an opportunity to investigate an orientation dependent shift in band gap position. The alignment of the islands, seen in the original and post transfer images, shows they are rotated 30° from one another. We can think of lattice vectors projected into recipocal space for triangular MoS_2 islands, with edges $(\bar{1}010)$ shown in previous scanning tunneling microscopy studies to be sulfur terminated.[72, 73] This known termination allows us to determine the orientation of the islands during strain measurements with respect to their reciprocal lattice. We can then investigate strain as it deforms the islands along axes of the high symmetry of the Brillouin zone as depicted in Figure 6.7 f.,g. By observing the orientation of the triangular islands and that strain is applied uniaxially on the sample, we can clearly define strain being applied either along the MM axis or the KK' axis. For the first case, that of MM strain, the K points in the lattice orthogonal to the direction of strain are unchanged in position. These points are labeled $K^{\perp}$, because they are orthogonal to the loading direction. The other four K points, for the MM' strain case, are displaced. These points are parrallel to the strain, shown in Figure 6.7 f., and identified as $K^{\parallel}$. For the second case of strain along the KK' axis, strain displaces all six of the K points. But, only two points which are parallel to the direction of the strain Figure 6.7 g., and

identified as K^{II}, are moved significantly. For the deformation seen in MM', the strain is causing only the Γ to K^{II} distance to change, an anisotropic outcome. On the KK' axis, deformation causes the distance between both K^{II}-Γ and Γ-$K^{\perp}$ to be stretched or shrunk commensurately. These displacements are shown schematically in Figure 6.7 e.,f. The distances are normalized for Figure 6.6 c., because it is the energy of the transition which is most interesting. However, the path can be distinguished by colors shown in Figure 6.6 b. Experimentally, we see a larger response in the photolumiscence spectra, a greater red-shift, for the anisotropic perturbation caused by strain applied along MM'. This is observed directly from the PL energy posiiton maps of the fitted spectra in Figure 6.7 c., and is also shown as a shift from the unstrained energy position in Figure 6.7 d.

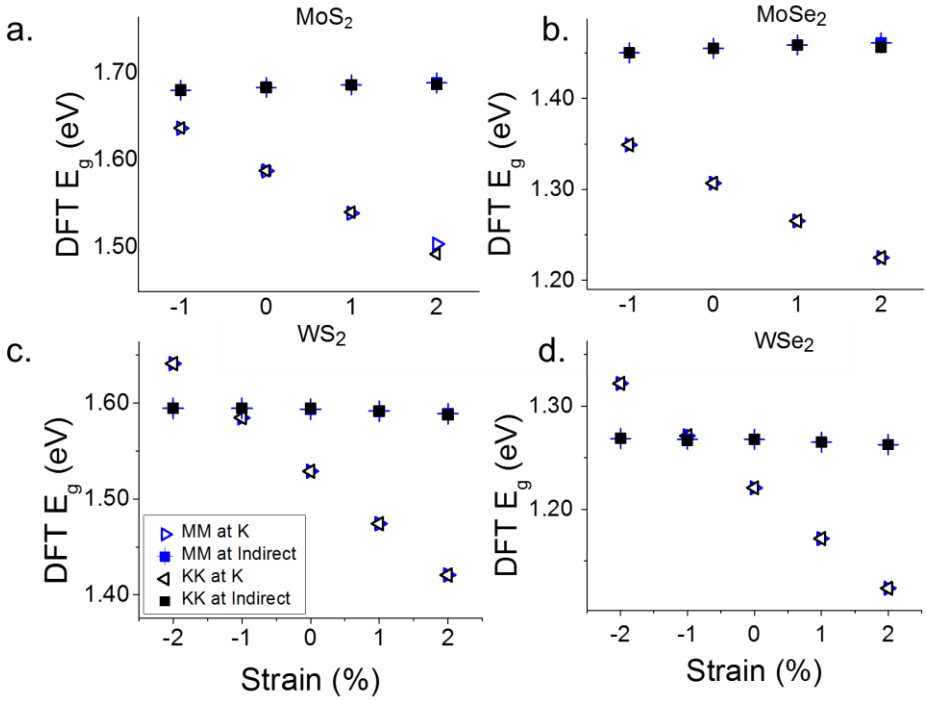

Figure 6.8: a.-d. The calculated band gap of the materials MoS_2, $MoSe_2$, WS_2, WSe_2 respectively, with strain applied along the KK' (black) or MM' (blue) directions. Symbols indicate the indirect (square) or direct (triangle) nature of the transition.

Considering the calculated band gap for the case of tungsten diselenide, the K point transition becomes higher in energy, at -1%, for either uniaxial strain direction, previously defined. In tungsten disulfide the crossover is less sensitive occurring only beyond -1% in compressive strain. This flip of minimum energy difference between the direct and indirect transitions is responsible for the mirrored effect of strain under compression seen in the tungsten dichalcogenide species and is due to enhanced d orbital character of the transition at K.

In our calculated band structures, along $K^{\perp}$-Γ-$K^{\parallel}$ from 0.1 to 1.6% tension as shown in Figure 6.6 c., the energy at the K point for either $K^{\parallel}$-Γ or $K^{\perp}$-Γ is degenerate in the MM' and KK' cases. For all the materials, the direct transition over the range of our calculations (-1 to 2%) remains the lowest energy transition. The indirect gap is also decreasing with increasing strain as seen in Figure 6.8. Our observations of the maps in Figure 6.7 c. demonstrate a larger narrowing for the MM case. Calculations show a small path dependent difference in the indirect band gap for the MoS_2 case of 2% strain seen in Figure 6.8 a. There is also an observed difference in responsivity seen in the spin orbit coupling data in Figure 6.6 a., with MM' at $K^{\perp}$ predicted to have larger amount of splitting. We see a subtle broadening of the peaks in the PL maps in Figure 6.7. This agrees well with the calculations for 0.5-1.5%, seen in the green panel of Figure 6.6 a., where there is a larger amount of spin splitting in the valence band at 1.5 % along MM as compared to KK' axis deformation.

As a periodic structure the lattice points $K^{\perp}$ and $K^{\parallel}$ of neighboring cells will coincide in reciprocal space, and therefore must have a singular energy. This pins the energy of $K^{\perp}$ and $K^{\parallel}$ in the conduction band to the same value at K for either path. Since the direct transition is the lower energy transition for the range of strain the islands are subjected to, the K point transition must play a role in the difference in shift between the crystallites. Since we consider only the high spin valence band energy in calculating the band gap at K, an energy change could be arising from the amount of spin splitting. Calculations show that, for the range of strains we consider, the MM direction has a larger amount of spin splitting. Analyzing the fwhm of the PL spectra of the islands shows a small, but potentially meaningful widening in the MM case.

6.4 Conclusion

In conclusion, in this single study, we have demonstrated the effects of uniaxial tensile and compressive strain on optical properties of four compositions of two dimensional, TMD materials grown by chemical vapor deposition (MoS_2, $MoSe_2$, WS_2, and WSe_2). The study examines homogeneous monolayer crystallites, without conflation of thickness differences problematic in mechanically exfoliated analogous materials. The direction of the strain effect for tension compared to compression was observed experimentally to be composition sensitive. Selenide materials showed a greater response. The sensitivity of the response differs with crystallographic orientation with respect to the strain axis for molybdenum

disulfide. Raman modes, known to be sensitive to in plane perturbation corroborate the measurements of the optical band gap shifts. And, to facilitate bending of our substrate, we show a low temperature physical transfer process amenable to the generic study transition metal dichalcogenide materials of arbitrary composition on flexible, transparent surfaces.

References

1. Yang, D.; Sandoval, S. J.; Divigalpitiya, W. M. R.; Irwin, J. C.; Frindt, R. F., Structure of single-molecular-layer MoS_2. *Physical Review B* **1991,** *43* (14), 12053-12056.

2. Mann, J.; Sun, D.; Ma, Q.; Chen, J.-R.; Preciado, E.; Ohta, T.; Diaconescu, B.; Yamaguchi, K.; Tran, T.; Wurch, M.; Magnone, K.; Heinz, T. F.; Kellogg, G. L.; Kawakami, R.; Bartels, L., Facile growth of monolayer MoS_2 film areas on SiO_2. *The European Physical Journal B* **2013,** *86* (5), 1-4.

3. Anthony, J. W.; Bideaux, R. A.; Bladh, K.; Nichols, M. C., Handbook of Mineralogy: Elements, Sulfides and Sulfosalts vol 1 (Tucson, AZ. Mineral Data Publishing: 1990.

4. Lee, C.; Yan, H.; Brus, L. E.; Heinz, T. F.; Hone, J.; Ryu, S., Anomalous Lattice Vibrations of Single- and Few-Layer MoS_2. *ACS Nano* **2010,** *4* (5), 2695-2700.

5. Splendiani, A.; Sun, L.; Zhang, Y.; Li, T.; Kim, J.; Chim, C.-Y.; Galli, G.; Wang, F., Emerging Photoluminescence in Monolayer MoS_2. *Nano Letters* **2010,** *10* (4), 1271-1275.

6. Komesu, T.; Le, D.; Zhang, X.; Ma, Q.; Schwier, E. F.; Kojima, Y.; Zheng, M.; Iwasawa, H.; Shimada, K.; Taniguchi, M.; Bartels, L.; Rahman, T. S.; Dowben, P. A., Occupied and unoccupied electronic structure of Na doped MoS2(0001). *Applied Physics Letters* **2014,** *105* (24), 241602.

7. Zhang, Y.; Chang, T.-R.; Zhou, B.; Cui, Y.-T.; Yan, H.; Liu, Z.; Schmitt, F.; Lee, J.; Moore, R.; Chen, Y., Direct observation of the transition from indirect to direct bandgap in atomically thin epitaxial $MoSe_2$. *Nature nanotechnology* **2014,** *9* (2), 111-115.

8. Tanabe, I.; Komesu, T.; Le, D.; Rawal, T. B.; Schwier, E. F.; Zheng, M.; Kojima, Y.; Iwasawa, H.; Shimada, K.; Rahman, T. S., The symmetry-resolved electronic structure of 2H-WSe_2 (0001). *Journal of Physics: Condensed Matter* **2016,** *28* (34), 345503.

9. Lebègue, S.; Eriksson, O., Electronic structure of two-dimensional crystals from -ab initio theory. *Physical Review B* **2009,** *79* (11), 115409.

10. Schmidt, H.; Giustiniano, F.; Eda, G., Electronic transport properties of transition metal dichalcogenide field-effect devices: surface and interface effects. *Chemical Society Reviews* **2015,** *44* (21), 7715-7736.

11. Conley, H. J.; Wang, B.; Ziegler, J. I.; Haglund, R. F.; Pantelides, S. T.; Bolotin, K. I., Bandgap Engineering of Strained Monolayer and Bilayer MoS_2. *Nano Letters* **2013,** *13* (8), 3626-3630.

12. Wang, Y.; Cong, C.; Qiu, C.; Yu, T., Raman Spectroscopy Study of Lattice Vibration and Crystallographic Orientation of Monolayer MoS_2 under Uniaxial Strain. *Small* **2013,** *9* (17), 2857-2861.

13. Sahin, H.; Tongay, S.; Horzum, S.; Fan, W.; Zhou, J.; Li, J.; Wu, J.; Peeters, F. M., Anomalous Raman spectra and thickness-dependent electronic properties of WSe_2. *Physical Review B* **2013,** *87* (16), 165409.

14. Mak, K. F.; Lee, C.; Hone, J.; Shan, J.; Heinz, T. F., Atomically thin MoS_2: a new direct-gap semiconductor. *Physical Review Letters* **2010,** *105* (13), 136805.
15. Butun, S.; Tongay, S.; Aydin, K., Enhanced Light Emission from Large-Area Monolayer MoS_2 Using Plasmonic Nanodisc Arrays. *Nano Letters* **2015,** *15* (4), 2700-2704.

16. Weber, W. H.; Merlin, R., *Raman scattering in materials science*. Springer Science & Business Media: 2013; Vol. 42.

17. Gołasa, K.; Grzeszczyk, M.; Korona, K. P.; Bożek, R.; Binder, J.; Szczytko, J.; Wysmołek, A.; Babiński, A., Optical Properties of Molybdenum Disulfide (MoS_2). *Acta Physica Polonica, A.* **2013,** *124* (5).

18. Martin, Y.; Williams, C. C.; Wickramasinghe, H. K., Atomic force microscope–force mapping and profiling on a sub 100-Å scale. *Journal of Applied Physics* **1987,** *61* (10), 4723-4729.

19. Jankov, I. R.; Goldman, I. D.; Szente, R. N., Principles of the Kelvin Probe Force Microscopy. *Revista Brasileira de Ensino de F ísica* **2000,** *22* (4), 503.

20. Zisman, W. A., A new method of measuring contact potential differences in metals. *Review of Scientific Instruments* **1932,** *3* (7), 367-370.

21. Glatzel, T.; Sadewasser, S.; Lux-Steiner, M. C., Amplitude or frequency modulation-detection in Kelvin probe force microscopy. *Applied Surface Science* **2003,** *210* (1–2), 84-89.

22. Yang, L.; Cui, X.; Zhang, J.; Wang, K.; Shen, M.; Zeng, S.; Dayeh, S. A.; Feng, L.; Xiang, B., Lattice strain effects on the optical properties of MoS_2 nanosheets. *Scientific Reports* **2014,** *4*, 5649.

23. Najmaei, S.; Liu, Z.; Zhou, W.; Zou, X.; Shi, G.; Lei, S.; Yakobson, B. I.; Idrobo, J.-C.; Ajayan, P. M.; Lou, J., Vapour phase growth and grain boundary structure of molybdenum disulphide atomic layers. *Nat Mater* **2013,** *12* (8), 754-759.

24. Lehtonen, A.; Sillanpéé, R., Dioxomolybdenum (VI) Complexes of Chelating. *Acta Chemica Scandinavica* **1999,** *53*, 1078-1082.

25. Hu, B.; Ago, H.; Ito, Y.; Kawahara, K.; Tsuji, M.; Magome, E.; Sumitani, K.; Mizuta, N.; Ikeda, K.-i.; Mizuno, S., Epitaxial growth of large-area single-layer graphene over Cu(111)/sapphire by atmospheric pressure CVD. *Carbon* **2012,** *50* (1), 57-65.

26. Liu, Y.; Wu, H.; Cheng, H.-C.; Yang, S.; Zhu, E.; He, Q.; Ding, M.; Li, D.; Guo, J.; Weiss, N. O.; Huang, Y.; Duan, X., Toward Barrier Free Contact to Molybdenum Disulfide Using Graphene Electrodes. *Nano Letters* **2015,** *15* (5), 3030-3034.

27. Azizi, A.; Eichfeld, S.; Geschwind, G.; Zhang, K.; Jiang, B.; Mukherjee, D.; Hossain, L.; Piasecki, A. F.; Kabius, B.; Robinson, J. A.; Alem, N., Freestanding van der Waals Heterostructures of Graphene and Transition Metal Dichalcogenides. *ACS Nano* **2015**.

28. Janisch, C.; Song, H.; Zhou, C.; Lin, Z.; Elías, A. L.; Ji, D.; Terrones, M.; Gan, Q.; Liu, Z., MoS_2 monolayers on nanocavities: enhancement in light–matter interaction. *2D Materials* **2016,** *3* (2), 025017.

29. Jackman, M. J.; Thomas, A. G.; Muryn, C., Photoelectron spectroscopy study of stoichiometric and reduced anatase TiO_2 (101) surfaces: the effect of subsurface defects on water adsorption at near-ambient pressures. *The Journal of Physical Chemistry C* **2015,** *119* (24), 13682-13690.

30. Jaramillo, T. F.; Jørgensen, K. P.; Bonde, J.; Nielsen, J. H.; Horch, S.; Chorkendorff, I., Identification of Active Edge Sites for Electrochemical H_2 Evolution from MoS_2 Nanocatalysts. *Science* **2007,** *317* (5834), 100-102.

31. Esposito, D. V.; Levin, I.; Moffat, T. P.; Talin, A. A., H_2 evolution at Si-based metal–insulator–semiconductor photoelectrodes enhanced by inversion channel charge collection and H spillover. *Nat Mater* **2013,** *12* (6), 562-568.

32. Seinfeld, J. H.; Pandis, S. N., *Atmospheric chemistry and physics: from air pollution to climate change*. John Wiley & Sons: 2016.

33. Tributsch, H., Solar energy-assisted electrochemical splitting of water. Some energetical, kinetical and catalytical considerations verified on MoS_2 layer crystal surfaces. *Zeitschrift für Naturforschung A* **1977,** *32* (9), 972-985.

34. Kudo, A.; Miseki, Y., Heterogeneous photocatalyst materials for water splitting. *Chemical Society Reviews* **2009,** *38* (1), 253-278.

35. Yu, Y.; Huang, S.-Y.; Li, Y.; Steinmann, S. N.; Yang, W.; Cao, L., Layer-Dependent Electrocatalysis of MoS_2 for Hydrogen Evolution. *Nano Letters* **2014,** *14* (2), 553-558.

36. Liao, L.; Zhu, J.; Bian, X.; Zhu, L.; Scanlon, M. D.; Girault, H. H.; Liu, B., MoS_2 formed on mesoporous graphene as a highly active catalyst for hydrogen evolution. *Advanced Functional Materials* **2013,** *23* (42), 5326-5333.

37. Gurarslan, A.; Yu, Y.; Su, L.; Yu, Y.; Suarez, F.; Yao, S.; Zhu, Y.; Ozturk, M.; Zhang, Y.; Cao, L., Surface-Energy-Assisted Perfect Transfer of Centimeter-Scale Monolayer and Few-Layer MoS_2 Films onto Arbitrary Substrates. *ACS Nano* **2014,** *8* (11), 11522-11528.

38. Donglin Ma, J. S., Qingqing Ji, Yu Zhang1, Mengxi Liu, Qingliang Feng, Xiuju Song, Jin Zhang, Yanfeng Zhang, Zhongfan Liu, Etching-free transfer of wafer-scale MoS_2 films. *arxiv* **2015**.

39. Jia, K.; Luo, J.; Hu, R.; Zhan, J.; Cao, H.; Su, Y.; Zhu, H.; Xie, L.; Zhao, C.; Chen, D., Evaluation of PMMA Residues as a Function of Baking Temperature and a Graphene Heat-Free-Transfer Process to Reduce Them. *ECS Journal of Solid State Science and Technology* **2016,** *5* (3), P138-P141.

40. Gaur, A. P. S.; Sahoo, S.; Ahmadi, M.; Dash, S. P.; Guinel, M. J. F.; Katiyar, R. S., Surface Energy Engineering for Tunable Wettability through Controlled Synthesis of MoS2. *Nano Letters* **2014,** *14* (8), 4314-4321.

41. Pirkle, A.; Chan, J.; Venugopal, A.; Hinojos, D.; Magnuson, C. W.; McDonnell, S.; Colombo, L.; Vogel, E. M.; Ruoff, R. S.; Wallace, R. M., The effect of chemical residues on the physical and electrical properties of chemical vapor deposited graphene transferred to SiO_2. *Applied Physics Letters* **2011,** *99* (12), 122108.

42. Suk, J. W.; Lee, W. H.; Lee, J.; Chou, H.; Piner, R. D.; Hao, Y.; Akinwande, D.; Ruoff, R. S., Enhancement of the Electrical Properties of Graphene Grown by Chemical Vapor Deposition via Controlling the Effects of Polymer Residue. *Nano Letters* **2013,** *13* (4), 1462-1467.

43. Namgung, S. D.; Yang, S.; Park, K.; Cho, A.-J.; Kim, H.; Kwon, J.-Y., Influence of post-annealing on the off current of MoS_2 field-effect transistors. *Nanoscale Research Letters* **2015,** *10*, 62.

44. Jia, H.; Yang, R.; Nguyen, A. E.; Alvillar, S. N.; Empante, T.; Bartels, L.; Feng, P. X. L., Large-scale arrays of single- and few-layer MoS_2 nanomechanical resonators. *Nanoscale* **2016,** *8* (20), 10677-10685.

45. Winer, W. O., Molybdenum disulfide as a lubricant: a review of the fundamental knowledge. *Wear* **1967,** *10* (6), 422-452.

46. Rafiee, J.; Mi, X.; Gullapalli, H.; Thomas, A. V.; Yavari, F.; Shi, Y.; Ajayan, P. M.; Koratkar, N. A., Wetting transparency of graphene. *Nature Materials* **2012,** *11* (3), 217-222.

47. Bodas, D.; Khan-Malek, C., Formation of more stable hydrophilic surfaces of PDMS by plasma and chemical treatments. *Microelectronic engineering* **2006,** *83* (4), 1277-1279.

48. Feynman, R. P., Mr. Feynman goes to Washington. *Engineering and Science* **1987,** *51* (1), 6-22.

49. Mann, J.; Ma, Q.; Odenthal, P. M.; Isarraraz, M.; Le, D.; Preciado, E.; Barroso, D.; Yamaguchi, K.; von Son Palacio, G.; Nguyen, A., 2-Dimensional Transition Metal Dichalcogenides with Tunable Direct Band Gaps: $MoS_{2\,(1-x)}$ Se_{2x} Monolayers. *Advanced Materials* **2014,** *26* (9), 1399-1404.

50. Johari, P.; Shenoy, V. B., Tuning the Electronic Properties of Semiconducting Transition Metal Dichalcogenides by Applying Mechanical Strains. *ACS Nano* **2012,** *6* (6), 5449-5456.

51. Chang, C.-H.; Fan, X.; Lin, S.-H.; Kuo, J.-L., Orbital analysis of electronic structure and phonon dispersion in MoS 2, $MoSe_2$, WS_2, and WSe_2 monolayers under strain. *Physical Review B* **2013,** *88* (19), 195420.

52. Amin, B.; Kaloni, T. P.; Schwingenschlogl, U., Strain engineering of WS_2, WSe_2, and WTe_2. *RSC Advances* **2014,** *4* (65), 34561-34565.

53. Bertolazzi, S.; Brivio, J.; Kis, A., Stretching and Breaking of Ultrathin MoS_2. *ACS Nano* **2011,** *5* (12), 9703-9709.

54. Bissett, M. A.; Tsuji, M.; Ago, H., Strain engineering the properties of graphene and other two-dimensional crystals. *Physical Chemistry Chemical Physics* **2014,** *16* (23), 11124-11138.

55. Castellanos-Gomez, A.; Roldán, R.; Cappelluti, E.; Buscema, M.; Guinea, F.; van der Zant, H. S. J.; Steele, G. A., Local Strain Engineering in Atomically Thin MoS_2. *Nano Letters* **2013,** *13* (11), 5361-5366.

56. He, K.; Poole, C.; Mak, K. F.; Shan, J., Experimental Demonstration of Continuous Electronic Structure Tuning via Strain in Atomically Thin MoS_2. *Nano Letters* **2013,** *13* (6), 2931-2936.

57. Rice, C.; Young, R. J.; Zan, R.; Bangert, U.; Wolverson, D.; Georgiou, T.; Jalil, R.; Novoselov, K. S., Raman-scattering measurements and first-principles calculations of strain-induced phonon shifts in monolayer MoS_2. *Physical Review B* **2013,** *87* (8), 081307.

58. Voiry, D.; Yamaguchi, H.; Li, J.; Silva, R.; Alves, D. C. B.; Fujita, T.; Chen, M.; Asefa, T.; Shenoy, V. B.; Eda, G.; Chhowalla, M., Enhanced catalytic activity in strained chemically exfoliated WS_2 nanosheets for hydrogen evolution. *Nat Mater* **2013,** *12* (9), 850-855.

59. Hui, Y. Y.; Liu, X.; Jie, W.; Chan, N. Y.; Hao, J.; Hsu, Y.-T.; Li, L.-J.; Guo, W.; Lau, S. P., Exceptional Tunability of Band Energy in a Compressively Strained Trilayer MoS_2 Sheet. *ACS Nano* **2013,** *7* (8), 7126-7131.

60. Wang, Y.; Cong, C.; Yang, W.; Shang, J.; Peimyoo, N.; Chen, Y.; Kang, J.; Wang, J.; Huang, W.; Yu, T., Strain-induced direct–indirect bandgap transition and phonon modulation in monolayer WS_2. *Nano Research* **2015,** *8* (8), 2562-2572.

61. Liu, K.; Yan, Q.; Chen, M.; Fan, W.; Sun, Y.; Suh, J.; Fu, D.; Lee, S.; Zhou, J.; Tongay, S.; Ji, J.; Neaton, J. B.; Wu, J., Elastic Properties of Chemical-Vapor-Deposited Monolayer MoS_2, WS_2, and Their Bilayer Heterostructures. *Nano Letters* **2014,** *14* (9), 5097-5103.

62. Mak, K. F.; Sfeir, M. Y.; Wu, Y.; Lui, C. H.; Misewich, J. A.; Heinz, T. F., *Phys. Rev. Lett.* **2008,** *101*, 196405.

63. Park, M.; Park, Y. J.; Chen, X.; Park, Y. K.; Kim, M. S.; Ahn, J. H., MoS_2-Based Tactile Sensor for Electronic Skin Applications. *Advanced Materials* **2016**.

64. Yun, S. J.; Chae, S. H.; Kim, H.; Park, J. C.; Park, J.-H.; Han, G. H.; Lee, J. S.; Kim, S. M.; Oh, H. M.; Seok, J.; Jeong, M. S.; Kim, K. K.; Lee, Y. H., Synthesis of Centimeter-Scale Monolayer Tungsten Disulfide Film on Gold Foils. *ACS Nano* **2015,** *9* (5), 5510-5519.

65. Ross, S.; Sussman, A., Surface oxidation of molybdenum disulfide. *The Journal of Physical Chemistry* **1955,** *59* (9), 889-892.

66. Perdew, J. P.; Burke, K.; Ernzerhof, M., Generalized gradient approximation made simple. *Physical review letters* **1996,** *77* (18), 3865.

67. Yu, Y.; Li, C.; Liu, Y.; Su, L.; Zhang, Y.; Cao, L., Controlled Scalable Synthesis of Uniform, High-Quality Monolayer and Few-layer MoS_2 Films. *Scientific Reports* **2013,** *3*, 1866.

68. Huang, J.-K.; Pu, J.; Hsu, C.-L.; Chiu, M.-H.; Juang, Z.-Y.; Chang, Y.-H.; Chang, W.-H.; Iwasa, Y.; Takenobu, T.; Li, L.-J., Large-Area Synthesis of Highly Crystalline WSe_2 Monolayers and Device Applications. *ACS Nano* **2014,** *8* (1), 923-930.

69. Gutiérrez, H. R.; Perea-López, N.; Elías, A. L.; Berkdemir, A.; Wang, B.; Lv, R.; López-Urías, F.; Crespi, V. H.; Terrones, H.; Terrones, M., Extraordinary room-temperature photoluminescence in triangular WS_2 monolayers. *Nano letters* **2012,** *13* (8), 3447-3454.

70. Xia, J.; Huang, X.; Liu, L.-Z.; Wang, M.; Wang, L.; Huang, B.; Zhu, D.-D.; Li, J.-J.; Gu, C.-Z.; Meng, X.-M., CVD synthesis of large-area, highly crystalline $MoSe_2$ atomic layers on diverse substrates and application to photodetectors. *Nanoscale* **2014,** *6* (15), 8949-8955.

71. Ellis, B.; Smith, R., *Polymers: A Property Database, Second Edition*. CRC Press: 2008.

72. Bollinger, M. V.; Lauritsen, J. V.; Jacobsen, K. W.; Nørskov, J. K.; Helveg, S.; Besenbacher, F., One-dimensional metallic edge states in MoS 2. *Physical review letters* **2001,** *87* (19), 196803.

73. Helveg, S.; Lauritsen, J. V.; Lægsgaard, E.; Stensgaard, I.; Nørskov, J. K.; Clausen, B. S.; Topsøe, H.; Besenbacher, F., Atomic-scale structure of single-layer MoS 2 nanoclusters. *Physical review letters* **2000,** *84* (5), 951.